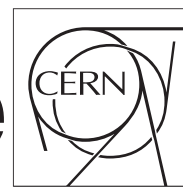


The Compact Muon Solenoid Experiment

CMS Draft Note

Mailing address: CMS CERN, CH-1211 GENEVA 23, Switzerland



2021/03/01

Archive Hash: 5dc9748-D

Archive Date: 2021/02/26

Measurements of Higgs differential cross section and interpretations in $H \rightarrow ZZ \rightarrow 4\ell$ ($\ell = e, \mu$) channel

M. Ahmad⁷, M. Bonanomi², M.S. Chen¹, Q.Y. Guo^{1,4}, T. Javaid^{1,4}, P. Milenovic⁵, V. Milosevic¹, C. Ochando², G. Ortona², R. Salerno², T. Sculac³, R. Sharma¹, and D. Sperka⁶

¹ IHEP, Beijing

² Laboratoire Leprince-Ringuet

³ University of Split

⁴ Beihang University

⁵ University of Belgrade

⁶ Boston University

⁷ Tsinghua University

Abstract

Properties of the Higgs boson are measured in the $H \rightarrow ZZ \rightarrow 4\ell$ ($\ell = e, \mu$) decay channel. A data sample of proton-proton collisions at a center-of-mass energy of 13 TeV is used, corresponding to an integrated luminosity of 137 fb^{-1} recorded by the CMS detector at the LHC. The fiducial cross section is measured with respect to several observables sensitive to production and decay of Higgs where the observed results are compared with POWHEG, MADGRAPH5 and NNLOPS theory predictions. The possible interpretations of the results are reported.

This box is only visible in draft mode. Please make sure the values below make sense.

PDFAuthor:	Qianying Guo, Vukasin Milosevic, Tahir Javaid, Ram Krishna Sharma
PDFTitle:	Measurements of Higgs differential cross section and interpretations in channel
PDFSubject:	CMS
PDFKeywords:	CMS, Higgs, ggH, SMEFT, Higgs Characterization, HEL, HEFT

Please also verify that the abstract does not use any user defined symbols

Acknowledgments

Contents

1	Introduction	2
2	1.1 EFT interepreations	2
3	1.2 Additionnal Prediction	3
4	2 Datasets, simulation samples and theoretical predictions	5
5	2.1 Triggers and Datasets	5
6	2.2 Simulation samples	8
7	2.3 Simulation samples for interpretations	9
8	3 Objects	10
9	3.1 Electrons	10
10	3.2 Muons	10
11	3.3 Photons for FSR recovery	11
12	3.4 Jets	11
13	4 Signal Modelling	16
14	5 Background Estimation	17
15	5.1 Estimation of ZZ normalization from Data	17
16	6 Analysis Strategy	18
17	6.1 Event Selection	18
18	6.2 Fiducial Volume Significance and Definition	19
19	6.3 Binning strategy for differential observables	20
20	6.4 Unfolding	21
21	6.5 Acceptance and other correction factors	21
22	6.6 Statistical Procedure	22
23	6.7 Extraction of differential $H \rightarrow 4\ell$ cross section	25
24	6.8 Interpretations	29
25	7 Systematic uncertainties	31
26	7.1 Systematic uncertainties treatment when combining the data sets	32
27	8 Results	37
28	8.1 Yields and distributions	37
29	8.2 Differential Cross Sections measurement results	41
30	8.3 Double differential cross section measurements	45
31	8.4 Interpretations	45
32	9 Interpretation	46
33	A Signal Shapes and Efficiencies	47
34	A.1 Differential bins - Higgs boson transverse momentum	47
35	A.2 Differential bins - rapidity of the Higgs boson	65
36	A.3 Signal fits in differential bins - number of jets	68

39 1 Introduction

40 The ATLAS and CMS collaborations first reported the discovery of a new boson in 2012 [1,
 41 2] consistent with the standard model (SM) Higgs boson [3–8] based on proton-proton (pp)
 42 collisions delivered by the CERN LHC at a center-of-mass energy of $\sqrt{s} = 7\text{ TeV}$ in years 2011
 43 and 8 TeV in 2012. Subsequent studies by CMS using the full LHC Run 1 data set in various
 44 decay channels and production modes and combined measurements from ATLAS and CMS
 45 [9–12] showed that the properties of the new boson are so far consistent with expectations for
 46 the SM Higgs boson.

47 The $H \rightarrow ZZ \rightarrow 4\ell$ decay channel ($\ell = e, \mu$) has a large signal-to-background ratio due to the
 48 complete reconstruction of the final state decay products and excellent lepton momentum res-
 49 olution and is one of the most important channels for studies of the Higgs boson’s properties.
 50 Measurements performed using this decay channel and the Run 1 data set include the deter-
 51 mination of the mass and spin-parity of the new boson [13–15], its width [16, 17] and fiducial
 52 cross sections [18], as well as tests for anomalous HVV couplings [15, 17].

53 In this document we present measurements of the differential fiducial cross sections for the
 54 Higgs boson production in the $H \rightarrow ZZ \rightarrow 4\ell$ decay channel at $\sqrt{s} = 13\text{ TeV}$ using 137 fb^{-1} of
 55 pp collision data collected with the CMS experiment at the LHC in 2016, 2017 and 2018. Differ-
 56 ential measurements for Higgs production variables have already been studied and published
 57 under [19]. In this analysis, in addition, the full available dataset has been fully re-analyzed,
 58 with several improvements:

- 59 • Analysis Ultra Legacy data.
- 60 • Revised measurement of lepton scale factors (Section 3.2.3)
- 61 • several additional (production and as well as decay) observables studied with opti-
 62 mized binning.
- 63 • in addition to POWHEG and NNLOPS, MADGRAPH5_AMC@NLO-FxFx is used as ad-
 64 ditional theory prediction to for comparision of the observed results.
- 65 • Effective Field Theory (EFT) interpretations of differential measurements are also
 66 presented.

67 1.1 EFT intereprations

68 Effective Field Theory (EFT) is an model independent way to parametrize the high enregy scale
 69 effects in the enregy scale available to us. The general form of the lagrangian is:

$$\mathcal{L} = \mathcal{L}_{SM} + \mathcal{L}^5 + \mathcal{L}^6 + \mathcal{L}^7 + \dots, \quad \mathcal{L}^{(d)} = \sum_{i=1}^{n_d} \frac{C_i^{(d)}}{\Lambda^{d-4}} Q_i^{(d)} \quad \text{for } d > 4, \quad (1)$$

70 Where Λ is the New Physics (NP) enregy scale, the parameter $C_i(d)$ are the Wilson Coefficients.
 71 One of most promissing EFT model is the SMEFT [20, 21]. Since the operators $Q_i^{(d)}$ are sur-
 72 presssed by the power of cutoff scale Λ , so we will work with dimension-6 operators only.
 73 Currently, we are trying to produce the Leading Order (LO) ggH process with additional jets
 74 upto 2 jets. Like:

```
75 import model SMEFTsim_A_general_MwScheme_UFO_v2
76 #import model SMEFTsim_A_general_alphaScheme_UFO_v2
```

```

77 generate p p > h QED=1 NP<=1 @0
78 add process p p > h j QED=1 NP<=1 @1
79 add process p p > h j j QED=1 NP<=1 @2

```

80 Our plan with this is following:

- 81 • Generate SM from the SMEFT model and compare it with the NNNLOPS official
samples (from HIG-19-001).
- 83 • Decide the set of parameter for which our analysis is sensitive.
- 84 • Validate the reweight method for our model.
- 85 • After finalizing previous step we will try to submit for official full CMSSW simula-
86 tion.

87 1.2 Additional Prediction

In order to do the additional cross check, we also exploite the ggH sample predicted by MadGraph5_aMCatNLO
 $HC_{NLO}X0_UFO-heft[????????????????]$ is a model file for the characterisation of the boson recently discovered at the
88 The effective field theory consists of the SM (except for the Higgs itself), expressed through the
89 physical degrees of freedom present below the EWSB scale, plus a new bosonic state X(JP) with
90 spin/parity assignments JP = 0+, 0, 1+, 1, and 2+.

$$\mathcal{L}_{HC,J} = \mathcal{L}_{SM-H} + \mathcal{L} \quad (2)$$

91 Currently, we produce the Next Leading Order (NLO) ggH process with additional jets up to 2
92 jets. Like:

```

93 set low_mem_multicore_nlo_generation True
94 #special model for gluon fusion higgs at NLO (effective theory in infinite top m
95 #note that this model is NOT needed for other SM higgs production modes
96 import model HC_NLO_X0_UFO-heft
97 define p = g u c b d s u~ c~ d~ s~ b~
98 define j = g u c b d s u~ c~ d~ s~ b~
99 generate p p > x0 / t a [QCD] @0
100 add process p p > x0 j / t a [QCD] @1
101 add process p p > x0 j j / t a [QCD] @2

```

102 Here is our djr plots to check the FxFx merging quality.

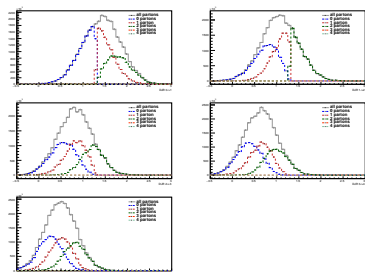


Figure 1: Differential Jet Ratio plots for the ggH with additional 0,1,2 jets using $\text{HC}_N\text{LO}_X 0_u \text{FO} - \text{heftmodelwithFx} \text{Fxmerging}$. The setting of $q\text{Cut}$ is 20.

103 2 Datasets, simulation samples and theoretical predictions

104 2.1 Triggers and Datasets

105 This analysis uses a ultra legacy data sample recorded by the CMS experiment during 2016,
 106 2017 and 2018, corresponding to 137 fb^{-1} of data.

107 The datasets used for 2016, 2017 and 2018 data taking are listed in Tables 1, 3, and 5, respec-
 108 tively, along with the integrated luminosity. The analysis relies on four different primary
 109 datasets (PDs), *DoubleMuon*, *MuEG*, *EGamma* (or *DoubleEG* and *SingleElectron* for 2016 and
 110 2017), and *SingleMuon*, each of which combines a certain collections of HLT paths. To avoid
 111 duplicate events from different primary datasets, events are taken:

- 112 • from EGamma if they pass the diEle or triEle or singleElectron triggers,
- 113 • from DoubleMuon if they pass the diMuon or triMuon triggers and fail the diEle
 114 and triEle triggers,
- 115 • from MuEG if they pass the MuEle or MuDiEle or DiMuEle triggers and fail the
 116 diEle, triEle, singleElectron, diMuon and triMuon triggers,
- 117 • from SingleMuon if they pass the singleMuon trigger and fail all the above triggers.

118 The HLT paths used for 2016, 2017 and 2018 collision data are listed in Tables 2, 4 and 6, respec-
 119 tively.

Run-range	Dataset	Integrated luminosity
272007-275376	/DoubleMuon/Run2016C-21Feb2020_UL2016.HIPM-v1/MINIAOD /DoubleMuon/Run2016B-21Feb2020_ver1_UL2016.HIPM-v1/MINIAOD /MuonEG/Run2016B-21Feb2020_ver1_UL2016.HIPM-v1/MINIAOD /SingleElectron/Run2016B-21Feb2020_ver1_UL2016.HIPM-v1/MINIAOD /SingleMuon/Run2016B-21Feb2020_ver1_UL2016.HIPM-v1/MINIAOD	5.892 fb^{-1}
275657-276283	/DoubleMuon/Run2016C-17Jul2018-v1/MINIAOD /DoubleEG/Run2016C-21Feb2020_UL2016.HIPM-v1/MINIAOD /MuonEG/Run2016C-21Feb2020_UL2016.HIPM-v1/MINIAOD /SingleElectron/Run2016C-21Feb2020_UL2016.HIPM-v1/MINIAOD /SingleMuon/Run2016C-21Feb2020_UL2016.HIPM-v1/MINIAOD	2.646 fb^{-1}
276315-276811	/DoubleEG/Run2016D-21Feb2020_UL2016.HIPM-v1/MINIAOD /DoubleMuon/Run2016D-21Feb2020_UL2016.HIPM-v1/MINIAOD /MuonEG/Run2016D-21Feb2020_UL2016.HIPM-v1/MINIAOD /SingleElectron/Run2016D-21Feb2020_UL2016.HIPM-v1/MINIAOD /SingleMuon/Run2016D-21Feb2020_UL2016.HIPM-v1/MINIAOD	4.353 fb^{-1}
276831-277420	/DoubleEG/Run2016E-21Feb2020_UL2016.HIPM-v1/MINIAOD /DoubleMuon/Run2016E-21Feb2020_UL2016.HIPM-v1/MINIAOD /MuonEG/Run2016E-21Feb2020_UL2016.HIPM-v1/MINIAOD /SingleElectron/Run2016E-21Feb2020_UL2016.HIPM-v1/MINIAOD /SingleMuon/Run2016E-21Feb2020_UL2016.HIPM-v1/MINIAOD	4.117 fb^{-1}
277772-278808	/DoubleEG/Run2016F-21Feb2020_UL2016-v1/MINIAOD /DoubleMuon/Run2016F-21Feb2020_UL2016.HIPM-v1/MINIAOD /MuonEG/Run2016F-21Feb2020_UL2016-v1/MINIAOD /SingleElectron/Run2016F-21Feb2020_UL2016-v1/MINIAOD /SingleMuon/Run2016F-21Feb2020_UL2016-v1/MINIAOD	3.186 fb^{-1}
278820-280385	/DoubleEG/Run2016G-21Feb2020_UL2016-v1/MINIAOD /DoubleMuon/Run2016G-21Feb2020_UL2016-v1/MINIAOD /MuonEG/Run2016G-21Feb2020_UL2016-v1/MINIAOD /SingleElectron/Run2016G-21Feb2020_UL2016-v1/MINIAOD /SingleMuon/Run2016G-21Feb2020_UL2016-v1/MINIAOD	7.721 fb^{-1}
280919-284044	/DoubleEG/Run2016H-21Feb2020_UL2016-v1/MINIAOD /DoubleMuon/Run2016H-21Feb2020_UL2016-v1/MINIAOD /MuonEG/Run2016H-21Feb2020_UL2016-v1/MINIAOD /SingleElectron/Run2016H-21Feb2020_UL2016-v2/MINIAOD /SingleMuon/Run2016H-21Feb2020_UL2016-v1/MINIAOD	8.857 fb^{-1}

Table 1: Datasets used in the 2016 analysis.

HLT path	prescale	primary dataset
HLT_Ele17_Ele12_CaloIdL_TrackIdL_IsoVL_DZ	1	DoubleEG
HLT_Ele23_Ele12_CaloIdL_TrackIdL_IsoVL_DZ	1	DoubleEG
HLT_DoubleEle33_CaloIdL_GsfTrkIdVL	1	DoubleEG
HLT_Ele16_Ele12_Ele8_CaloIdL_TrackIdL	1	DoubleEG
HLT_Mu17_TrkIsoVVL_Mu8_TrkIsoVVL	1	DoubleMuon
HLT_Mu17_TrkIsoVVL_TkMu8_TrkIsoVVL	1	DoubleMuon
HLT_TripleMu_12_10_5	1	DoubleMuon
HLT_Mu8_TrkIsoVVL_Ele17_CaloIdL_TrackIdL_IsoVL	1	MuonEG
HLT_Mu8_TrkIsoVVL_Ele23_CaloIdL_TrackIdL_IsoVL	1	MuonEG
HLT_Mu17_TrkIsoVVL_Ele12_CaloIdL_TrackIdL_IsoVL	1	MuonEG
HLT_Mu23_TrkIsoVVL_Ele12_CaloIdL_TrackIdL_IsoVL	1	MuonEG
HLT_Mu23_TrkIsoVVL_Ele8_CaloIdL_TrackIdL_IsoVL	1	MuonEG
HLT_Mu8_DiEle12_CaloIdL_TrackIdL	1	MuonEG
HLT_DiMu9_Ele9_CaloIdL_TrackIdL	1	MuonEG
HLT_Ele25_eta2p1_WPTight	1	SingleElectron
HLT_Ele27_WPtight	1	SingleElectron
HLT_Ele27_eta2p1_WPLoose_Gsf	1	SingleElectron
HLT_IsoMu20 OR HLT_IsoTkMu20	1	SingleMuon
HLT_IsoMu22 OR HLT_IsoTkMu22	1	SingleMuon

Table 2: Trigger paths used in 2016 collision data.

Run-range	Dataset	Integrated luminosity
297046-299329	/DoubleMuon/Run2017B-UL2017_MiniAODv2-v1/MINIAOD /DoubleEG/Run2017B-09Aug2019_UL2017-v1/MINIAOD /MuonEG/Run2017B-UL2017_MiniAODv2-v1/MINIAOD /SingleElectron/Run2017B-UL2017_MiniAODv2-v1/MINIAOD /SingleMuon/Run2017B-09Aug2019_UL2017-v1/MINIAOD	4.792 fb ⁻¹
299368-300676	/DoubleMuon/Run2017C-UL2017_MiniAODv2-v1/MINIAOD /DoubleEG/Run2017C-UL2017_MiniAODv2-v2/MINIAOD /MuonEG/Run2017C-UL2017_MiniAODv2-v1/MINIAOD /SingleElectron/Run2017C-UL2017_MiniAODv2-v1/MINIAOD /SingleMuon/Run2017C-09Aug2019_UL2017-v1/MINIAOD	9.755 fb ⁻¹
302030-303434	/DoubleMuon/Run2017D-UL2017_MiniAODv2-v1/MINIAOD /DoubleEG/Run2017D-UL2017_MiniAODv2-v1/MINIAOD /MuonEG/Run2017D-UL2017_MiniAODv2-v1/MINIAOD /SingleElectron/Run2017D-09Aug2019_UL2017-v1/MINIAOD /SingleMuon/Run2017D-09Aug2019_UL2017-v1/MINIAOD	4.319 fb ⁻¹
303824-304797	/DoubleMuon/Run2017E-09Aug2019_UL2017-v1/MINIAOD /DoubleEG/Run2017E-UL2017_MiniAODv2-v1/MINIAOD /MuonEG/Run2017E-UL2017_MiniAODv2-v1/MINIAOD /SingleElectron/Run2017E-UL2017_MiniAODv2-v1/MINIAOD /SingleMuon/Run2017E-09Aug2019_UL2017-v1/MINIAOD	9.424 fb ⁻¹
305040-306462	/DoubleMuon/Run2017F-UL2017_MiniAODv2-v1/MINIAOD /DoubleEG/Run2017F-09Aug2019_UL2017-v1/MINIAOD /MuonEG/Run2017F-UL2017_MiniAODv2-v1/MINIAOD /SingleElectron/Run2017F-UL2017_MiniAODv2-v1/MINIAOD /SingleMuon/Run2017F-09Aug2019_UL2017-v1/MINIAOD	13.50 fb ⁻¹
278820-280385	/DoubleMuon/Run2017G-09Aug2019_UL2017-v1/MINIAOD /DoubleEG/Run2017G??_MINIAOD /MuonEG/Run2017G??_MINIAOD /SingleElectron/Run2017G??_MINIAOD /SingleMuon/Run2017G?_MINIAOD	7.721 fb ⁻¹
281207-284068	/DoubleMuon/Run2017H-UL2017_MiniAODv2-v1/MINIAOD /DoubleEG/Run2017??_MINIAOD /MuonEG/Run2017H??_MINIAOD /SingleElectron/Run2017H??_MINIAOD /SingleMuon/Run2017H??_MINIAOD	8.857 fb ⁻¹

Table 3: Datasets used in the 2017 analysis.

HLT path	prescale	primary dataset
HLT_Ele23_Ele12_CaloIdL_TrackIdL_IsoVL_*	1	DoubleEG
HLT_DoubleEle33_CaloIdL_GsfTrkIdVL	1	DoubleEG
HLT_Ele16_Ele12_Ele8_CaloIdL_TrackIdL	1	DoubleEG
HLT_Mu17_TrkIsoVVL_Mu8_TrkIsoVVL_DZ_Mass3p8	1	DoubleMuon
HLT_Mu17_TrkIsoVVL_Mu8_TrkIsoVVL_DZ_Mass8	1	DoubleMuon
HLT_TripleMu_12_10_5	1	DoubleMuon
HLT_TripleMu_10_5_5_D2	1	DoubleMuon
HLT_Mu23_TrkIsoVVL_Ele12_CaloIdL_TrackIdL_IsoVL	1	MuonEG
HLT_Mu8_TrkIsoVVL_Ele23_CaloIdL_TrackIdL_IsoVL_DZ	1	MuonEG
HLT_Mu12_TrkIsoVVL_Ele23_CaloIdL_TrackIdL_IsoVL_DZ	1	MuonEG
HLT_Mu23_TrkIsoVVL_Ele12_CaloIdL_TrackIdL_IsoVL_DZ	1	MuonEG
HLT_DiMu9_Ele9_CaloIdL_TrackIdL_DZ	1	MuonEG
HLT_Mu8_DiEle12_CaloIdL_TrackIdL	1	MuonEG
HLT_Mu8_DiEle12_CaloIdL_TrackIdL_DZ	1	MuonEG
HLT_Ele35_WPTight_Gsf_v*	1	SingleElectron
HLT_Ele38_WPTight_Gsf_v*	1	SingleElectron
HLT_Ele40_WPTight_Gsf_v*	1	SingleElectron
HLT_IsoMu27	1	SingleMuon

Table 4: Trigger paths used in 2017 collision data.

Run-range	Dataset	Integrated luminosity
315252-316995	/DoubleMuon/Run2018A-UL2018_MiniAODv2-v1/MINIAOD /MuonEG/Run2018A-12Nov2019_UL2018_rsb-v1/MINIAOD /EGamma/Run2018A-12Nov2019_UL2018-v2/MINIAOD /SingleMuon/Run2018A-UL2018_MiniAODv2-v1/MINIAOD	X.XXX fb ⁻¹
317080-319310	/DoubleMuon/Run2018B-UL2018_MiniAODv2-v2/MINIAOD /MuonEG/Run2018B-12Nov2019_UL2018-v1/MINIAOD /EGamma/Run2018B-UL2018_MiniAODv2-v1/MINIAOD /SingleMuon/Run2018B-12Nov2019_UL2018-v2/MINIAOD	X.XXX fb ⁻¹
319337-320065	/DoubleMuon/Run2018C-12Nov2019_UL2018-v2/MINIAOD /MuonEG/Run2018C-12Nov2019_UL2018-v1/MINIAOD /EGamma/Run2018C-UL2018_MiniAODv2-v1/MINIAOD /SingleMuon/Run2018C-12Nov2019_UL2018-v2/MINIAOD	X.XXX fb ⁻¹
320673-325175	/DoubleMuon/Run2018D-UL2018_MiniAODv2-v1/MINIAOD /MuonEG/Run2018D-12Nov2019_UL2018_rsb-v1/MINIAOD /EGamma/Run2018D-UL2018_MiniAODv2-v1/MINIAOD /SingleMuon/Run2018D-12Nov2019_UL2018-v4/MINIAOD	X.XXX fb ⁻¹

Table 5: Datasets used in the 2018 analysis.

HLT path	prescale	primary dataset
HLT_Ele23_Ele12_CaloIdL_TrackIdL_IsoVL_v*	1	DoubleEG
HLT_DoubleEle25_CaloIdL_MW_v*	1	DoubleEG
HLT_Mu17_TrkIsoVVL_Mu8_TrkIsoVVL_DZ_Mass3p8_v*	1	DoubleMuon
HLT_Mu23_TrkIsoVVL_Ele12_CaloIdL_TrackIdL_IsoVL_v*	1	MuonEG
HLT_Mu8_TrkIsoVVL_Ele23_CaloIdL_TrackIdL_IsoVL_DZ_v*	1	MuonEG
HLT_Mu12_TrkIsoVVL_Ele23_CaloIdL_TrackIdL_IsoVL_DZ_v*	1	MuonEG
HLT_DiMu9_Ele9_CaloIdL_TrackIdL_DZ_v*	1	MuonEG
HLT_Ele32_WPTight_Gsf_v*	1	SingleElectron
HLT_IsoMu24_v*	1	SingleMuon

Table 6: Trigger paths used in 2018 collision data.

120 2.1.1 Trigger Efficiency

121 The efficiency in data of the combination of triggers used in the analysis with respect to the
 122 offline reconstruction and selection is measured by considering 4ℓ events triggered by single
 123 lepton triggers. Details on the procedures are described in $H \rightarrow ZZ \rightarrow 4\ell$ ($\ell = e, \mu$) analyses
 124 common note [19].

125 A summary of the trigger efficiencies in MC truth, and in MC and data using the tag and probe
 126 method are summarized in table 7. The trigger efficiency in simulation is found to be $> 99\%$ in
 127 each final state.

Final State	$gg \rightarrow H$ MC	$gg \rightarrow H$ MC (matching)	Data (matching)
$4e$	$0.991^{+.002}_{-.002}$	$0.948^{+.004}_{-.004}$	$0.982^{+.005}_{-.007}$
4μ	$0.997^{+.001}_{-.001}$	$0.997^{+.001}_{-.001}$	$1.000^{+.000}_{-.001}$
$2e2\mu$	$0.995^{+.001}_{-.001}$	$0.964^{+.002}_{-.002}$	$0.983^{+.003}_{-.004}$

Table 7: Trigger efficiencies measured using 4ℓ events in 2018 data (TBU).

128 2.2 Simulation samples

129 2.2.1 Signal Samples

130 Descriptions of the SM Higgs boson production are obtained using the POWHEG V2 [22–24]
 131 generator for the five main production modes: gluon fusion ($gg \rightarrow H$) including quark mass
 132 effects [25], vector boson fusion (VBF) [26], and associated production (WH, ZH and $t\bar{t} H$ [27]).
 133 The simulation of Higgs production through gluon fusion i.e. $gg \rightarrow H$ production at next-
 134 to-next-to-leading order (NNLO) is obtained by NNLOPS [28] and is used in the analysis as
 135 reference theory predictions for observed differential cross section results. A dedicated studies
 136 using MADGRAPH5_AMC@NLO-FxFx generators with next-to-leading order (NLO) accuracy
 137 is done for $gg \rightarrow H$ production as additional theoretical predication for fiducial cross section
 138 measurement. Details are described in Section 2.2.1. In the case of WH and ZH the MINLO
 139 HVJ extension of POWHEG is used [29]. The description of the decay of the Higgs boson to
 140 four leptons is obtained using the JHUGEN generator [30]. In the case of WH, ZH and $t\bar{t} H$,
 141 the Higgs boson is allowed to decay to $H \rightarrow ZZ \rightarrow 2\ell^2 X$ such that 4-lepton events where two
 142 leptons originate from the decay of associated Z, W bosons or top quarks are also taken into
 143 account in the simulation. Showering of parton-level events is done using PYTHIA8.209, and in
 144 all cases matching is performed by allowing QCD emissions at all energies in the shower and
 145 vetoing them afterwards according to the POWHEG internal scale. All samples are generated
 146 with the NNPDF 3.1 NLO parton distribution functions (PDFs) [31]. The list of signal samples
 147 and their cross sections are shown in Table 8. For each year, corresponding simulation samples
 148 are reweighted to match the pileup distribution in data for which details are described in [19].

149 Simulation of Higgs production using MADGRAPH5

150 To be updated.

151 2.2.2 Background Samples

152 Production of ZZ via quark-antiquark annihilation is generated at next-to-leading order (NLO)
 153 using POWHEG V2 [32] and PYTHIA8, with the same settings as for the Higgs signal. As this
 154 simulation covers a large range of ZZ invariant masses, dynamical QCD factorization and
 155 renormalization scales have been chosen, equal to m_{ZZ} .

156 The $gg \rightarrow ZZ$ process is simulated at leading order (LO) with MCFM [33, 34]. In order to match
 157 the $gg \rightarrow H \rightarrow ZZ$ transverse momentum spectra predicted by POWHEG at NLO, the showering

Process	Dataset Name	$\sigma \times BR(\times \epsilon_{\text{filter}})$
$gg \rightarrow H(124) \rightarrow ZZ \rightarrow 4\ell$	/GluGluHToZZTo4L_M124_13TeV_powheg2_JHUGenV7011_pythia8/[1]	12.18 fb
$gg \rightarrow H(125) \rightarrow ZZ \rightarrow 4\ell$	/GluGluHToZZTo4L_M125_13TeV_powheg2_JHUGenV7011_pythia8/[1]	12.18 fb
$gg \rightarrow H(126) \rightarrow ZZ \rightarrow 4\ell$	/GluGluHToZZTo4L_M126_13TeV_powheg2_JHUGenV7011_pythia8/[1]	12.18 fb
$qq \rightarrow Hqq \rightarrow ZZqq \rightarrow 4\ell qq$	/VBF_HToZZTo4L_M125_13TeV_powheg2_JHUGenV709_pythia8/[1]	1.044 fb
$qq \rightarrow W^+H \rightarrow W^+ZZ \rightarrow 4\ell + X$	/WplusH_HToZZTo4L_M125_13TeV_powheg2-minlo-HWJ_JHUGenV7011_pythia8/[1]	0.232 fb
$qq \rightarrow W^-H \rightarrow W^-ZZ \rightarrow 4\ell + X$	/WminusH_HToZZTo4L_M125_13TeV_powheg2-minlo-HWJ_JHUGenV7011_pythia8/[1]	0.147 fb
$qq \rightarrow ZH \rightarrow ZZZ \rightarrow 4\ell + X$	/ZH_HToZZ_4LFitter_M125_13TeV_powheg2-minlo-HZJ_JHUGenV7011_pythia8/[1]	0.668 fb
$gg \rightarrow ttH \rightarrow ttZZ \rightarrow 4\ell + X$	/ttH_HToZZ_4LFitter_M125_13TeV_powheg_JHUGenV7011_pythia8/[1]	0.393 fb
$gg \rightarrow bbH \rightarrow bbZZ \rightarrow 4\ell + X$	/bbH_HToZZTo4L_M125_13TeV_JHUGenV7011_pythia8/[1]	0.135 fb
$q\bar{q}/qg \rightarrow tHq \rightarrow tqZZ \rightarrow 4\ell + X$	/tqH_HToZZTo4L_M125_13TeV_JHUGenV7011_pythia8/[1]	0.0213 fb

[1] HIG-RunIISummer20UL18wmLHEGEN-000*

Table 8: Signal Monte Carlo samples and cross sections.

Process	Dataset Name	$\sigma \cdot BR$
$qq \rightarrow ZZ \rightarrow 4\ell$	/ZZTo4L_TuneCP5_13TeV_powheg_pythia8/	1.256 pb
$qq \rightarrow ZZ \rightarrow 4\ell$	/ZZTo4L_TuneCP5_13TeV_amcatnloFXFX_pythia8/	1.212 pb
$gg \rightarrow ZZ \rightarrow 4e$	/GluGluToContinToZZTo4e_13TeV_MCFM701/	0.00159 pb
$gg \rightarrow ZZ \rightarrow 4\tau$	/GluGluToContinToZZTo4mu_13TeV_MCFM701/	0.00159 pb
$gg \rightarrow ZZ \rightarrow 2e2\tau$	/GluGluToContinToZZTo2e2mu_13TeV_MCFM701/	0.00319 pb
$Z \rightarrow \ell\ell + \text{jets}$	/DYJetsToLL_M-50_TuneCUETP8M1_13TeV-amcatnloFXFX_pythia8/	6104 pb
$Z \rightarrow \ell\ell + \text{jets}$	/DYJetsToLL_M-10to50_TuneCUETP8M1_13TeV-amcatnloFXFX_pythia8/	18610 pb
$WZ \rightarrow 3\ell\nu$	/WZTo3LNu_TuneCUETP8M1_13TeV-powheg_pythia8/	4.430 pb
$t\bar{t}$	/TTJets_TuneCUETP8M1_13TeV-amcatnloFXFX_pythia8/	815.96 pb
$t\bar{t} \rightarrow 2\ell 2\nu 2b$	/TTTo2L2Nu_13TeV-powheg/	87.31 pb
ZZZ	/ZZZ_TuneCUETP8M1_13TeV-amcatnlo_pythia8/	0.01398 pb
WZZ	/WZZ_TuneCUETP8M1_13TeV-amcatnlo_pythia8/	0.05565 pb
WWZ	/WWZ_TuneCUETP8M1_13TeV-amcatnlo_pythia8/	0.1651 pb
$t\bar{t}+ZZ$	/TTZZ_TuneCUETP8M2T4_13TeV-madgraph_pythia8/	0.001572 pb
$t\bar{t}+WW$	/TTWW_TuneCUETP8M2T4_3TeV - madgraph - pythia8/	0.007883 pb
$t\bar{t}+Z$	/ttZJets_13TeV_madgraphMLM/	0.259 pb

Table 9: Background Monte Carlo samples and cross sections.

- for MCFM samples is performed with different PYTHIA8 settings, allowing only emissions up to the parton-level scale (“wimpy” shower).
- Although not directly used to model data observations, additional MC samples of WZ, Drell-Yan+jets, $t\bar{t}$, and tribosons are generated using MADGRAPH5_AMCANTNLO [35] either inclusively or merging several jet multiplicities, as detailed in the table. Table 9 summarizes the MC simulation datasets used for this analysis.

2.3 Simulation samples for interpretations

165 3 Objects

166 This analysis follows the same object defintion as in [36] for each year. Detailed descriptcion
 167 on objection definitions and scale factors can be found in the corresponding analysis note [19].
 168 Since this analysis is based on Ultra Legacy (UL) full Run 2 data, most of the objects related
 169 ingredients will be reevaluated with respect to [19].

170 The reconstruction of the SM Higgs boson in the decay chain $H \rightarrow ZZ \rightarrow 4\ell$ requires very
 171 efficient lepton reconstruction and identification in order to be sensitive to a low mass Higgs,
 172 for which at least one of the leptons has a p_T within the range 5 - 15 GeV. In this kinematic
 173 region the need is for an optimal efficiency, while retaining the rate of misidentified leptons
 174 low enough. On the same time, to allow a precise measurement of the Higgs boson mass and
 175 together properties, which depend on the lepton kinematics, the analysis needs a precise mo-
 176 mentum measurement. For both reasons, the analysis will make use of high statistics sources
 177 of prompt leptons to measure efficiency, mis-identification rate, and energy scale/resolution.
 178 Muon Efficiency measuremens using UL dataset are discribed as follows:

179 3.1 Electrons

180 3.1.1 Electron Reconstruction and Identification

181 Referred to [19].

182 3.1.2 Electron Energy Calibrations

183 Referred to [19].

184 3.1.3 Electron Efficiency Measurements

185 Referred to [19].

186 3.2 Muons

187 3.2.1 Muon Reconstruction and Identification

188 Referred to [19].

189 3.2.2 Muon Energy Calibrations

190 Referred to [19].

191 3.2.3 Muon Efficiency Measurements

192 Muon efficiencies are measured with the Tag and Probe (T&P) method performed on $Z \rightarrow \mu\mu$
 193 and $J/\psi \rightarrow \mu\mu$ events in bins of p_T and η . More details on the methodology can be found
 194 in Ref. [37]. Measurements are extracted using 2016, 2017 and 2018 UL data. The Z sample
 195 is used to measure the muon reconstruction and identification efficiency at high p_T , and the
 196 efficiency of the isolation and impact parameter requirements at all p_T . The J/ψ sample is used
 197 to measure the reconstruction efficiency at low p_T , as it benefits from a better purity in that
 198 kinematic regime.

199 **Reconstruction and identification** Results for the muon reconstruction and identification
 200 efficiency for $p_T > 20$ GeV have been derived by the Muon POG. However, results for low p_T
 201 muons were derived using J/ψ events, with the same definitions of probe and passing probes.
 202 Events are selected using `HLT_Mu8_v*` or `HLT_Mu17_v*` or `HLT_Mu20_v*` triggers. The probe

203 in this measurement are tracks reconstructed in the inner tracker, and the passing probes are
 204 those that are also reconstructed as a global or tracker muon and passing the Muon POG Loose
 205 muon identification.

206 Details on the procedure can be found in Ref. [37]. The efficiency and scale factors used for low
 207 p_T muons are the ones derived using single muon ultra-legacy dataset.

208 The efficiency in data and simulation is shown in Fig. 2.

209 **Impact parameter requirements** The measurement is performed using Z events. Events
 210 are selected with `HLT_IsoMu20_v*` or `HLT_IsoMu22_v*` or `HLT_IsoMu22_eta2p1_v*` for
 211 2016, `HLT_IsoMu27_v*` for 2017 and `HLT_IsoMu24_v*` for 2018 measurements. For this mea-
 212 surement, the probe is a muon passing the POG Loose identification criteria, and it is consid-
 213 ered a passing probe if it satisfies the SIP3D, dxy , dz cuts of this analysis. The results are shown
 214 in Fig. 3.

215 **Isolation requirements** The isolation efficiency is measured using events from the Z decay
 216 for any p_T . The events are selected with the triggers as required for impact parameter require-
 217 ments measurements as explained in previous paragraph. To fit the FSR contribution in the
 218 low mass region, MC template convoluted with the Gaussian is used to better fit the dimuon
 219 invariant mass.

220 The results are shown in Fig. 4.

221 **Tracking** The efficiency to reconstruct a muon track in the inner detector can be measured
 222 using as probes tracks reconstructed in the muon system alone. However, since it comes out to
 223 be 100%, it is no more recommended by muon POG.

224 **Overall results** The product of all the data to simulation scale factors for muon tracking,
 225 reconstruction, identification, impact parameter and isolation requirements is shown in Fig. 5.
 226 The systematic effects on measurements are estimated by ¹:

- 227 1. Varying the analytical signal and background shape models used to fit the dimuon in-
 228 variant mass
- 229 2. Increasing and decreasing the number of bins in dimuon mass distribution
- 230 3. Increasing and decreasing the dimuon mass range
- 231 4. Relaxing and tightening a selection cut on tag muons

232 3.3 Photons for FSR recovery

233 Referred to [19].

234 3.4 Jets

235 Referred to [19].

¹For low p_T measurements of reconstruction and identification only first three systematic sources are used as recommended by muon POG

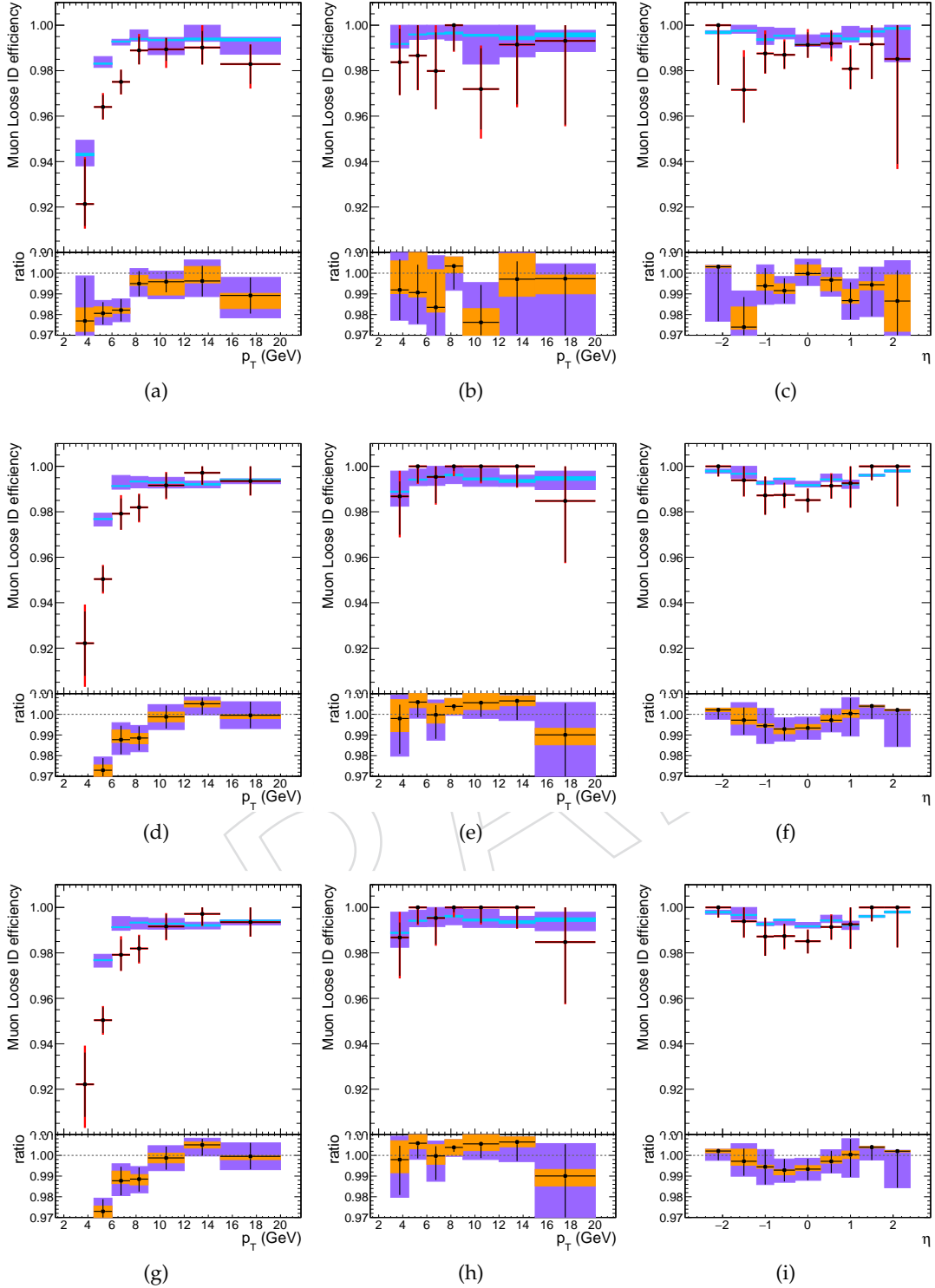


Figure 2: Muon reconstruction and identification efficiency at low p_T , measured with the tag&probe method on J/ψ events, as function of p_T in the barrel (left) and endcaps (center), and as function of η for $p_T > 7\text{ GeV}$ (right), for 2016 (top), 2017 (middle) and 2018 (bottom). In the upper panel, the larger error bars include also the systematical uncertainties, while the smaller ones are purely statistical. In the lower panel showing the ratio of the two efficiencies, the black error bars are for the statistical uncertainty, the orange rectangles for the systematical uncertainty and the violet rectangles include both uncertainties.

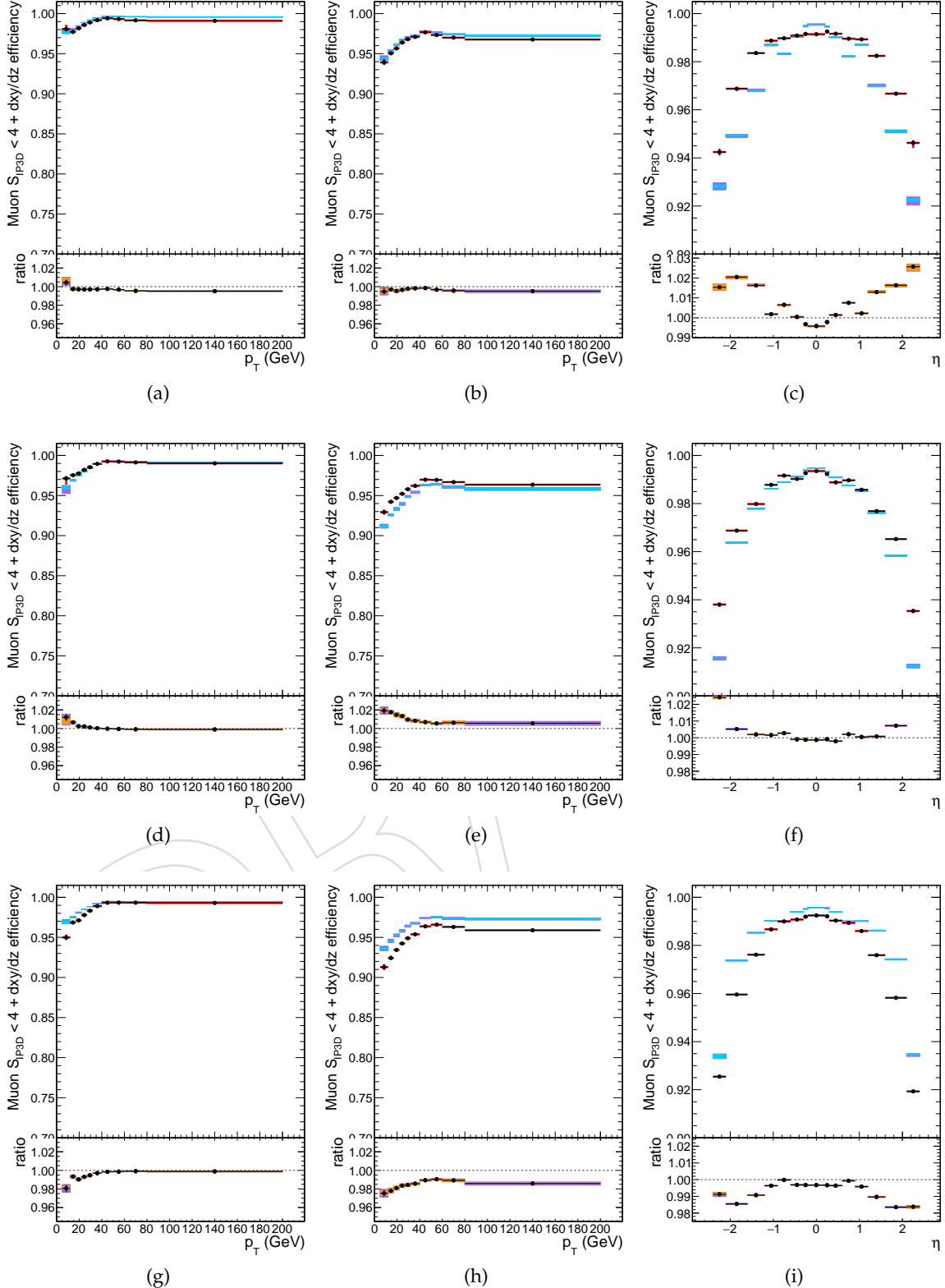


Figure 3: Efficiency of the muon impact parameter requirements, measured with the tag&probe method on Z events, as function of p_T in the barrel (left) and endcaps (center), and as function of η for $p_T > 20$ GeV (right), for 2016 (top), 2017 (middle) and 2018 (bottom). In the upper panel, the larger error bars include also the systematical uncertainties, while the smaller ones are purely statistical. In the lower panel showing the ratio of the two efficiencies, the black error bars are for the statistical uncertainty, the orange rectangles for the systematical uncertainty and the violet rectangles include both uncertainties.

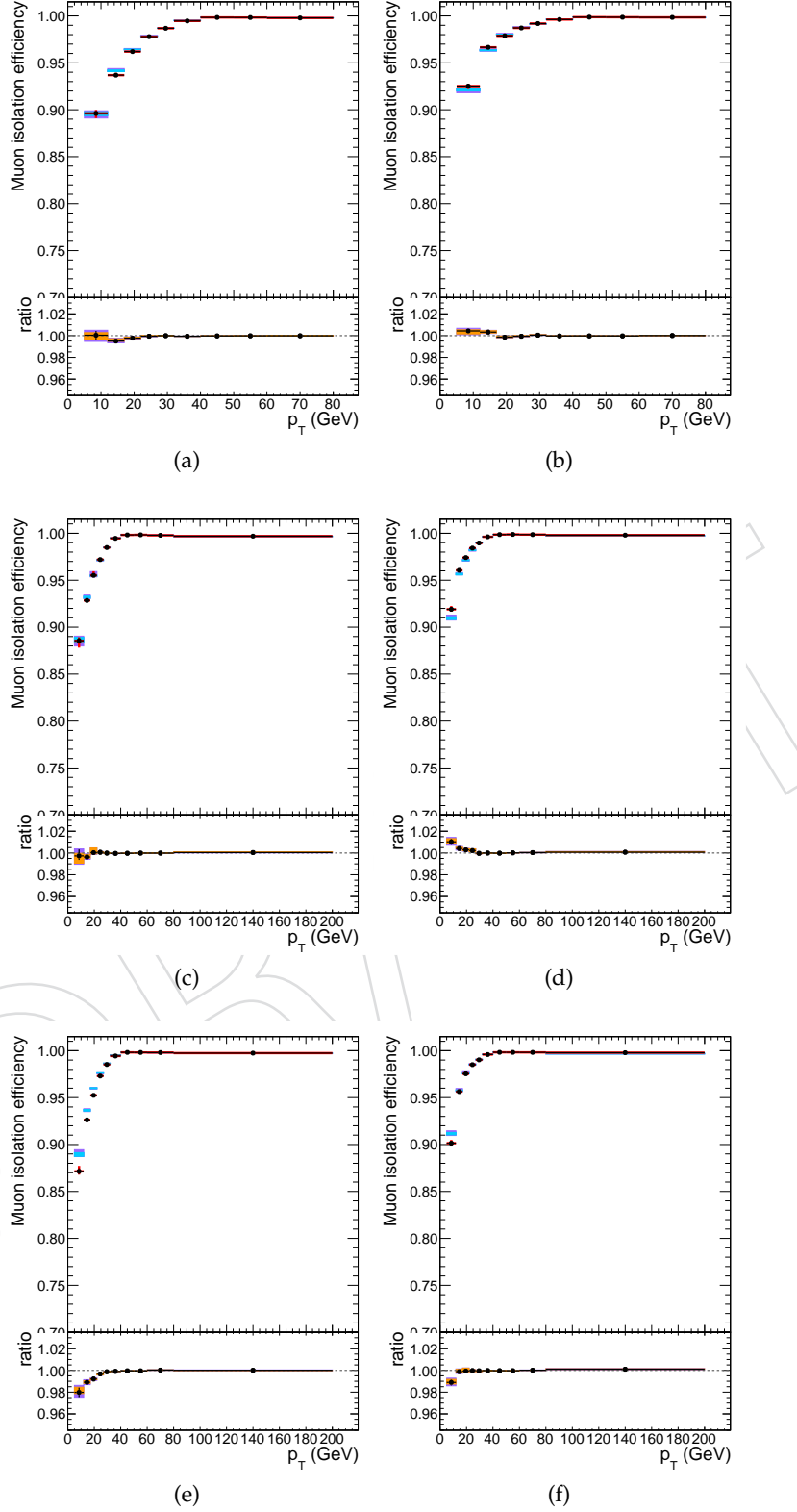


Figure 4: Efficiency of the muon isolation requirement, measured with the tag&probe method on Z events, as function of p_T in the barrel (left) and endcaps (right), for 2016 (top), 2017 (middle) and 2018 (bottom). In the upper panel, the larger error bars include also the systematical uncertainties, while the smaller ones are purely statistical. In the lower panel showing the ratio of the two efficiencies, the black error bars are for the statistical uncertainty, the orange rectangles for the systematical uncertainty and the violet rectangles include both uncertainties.

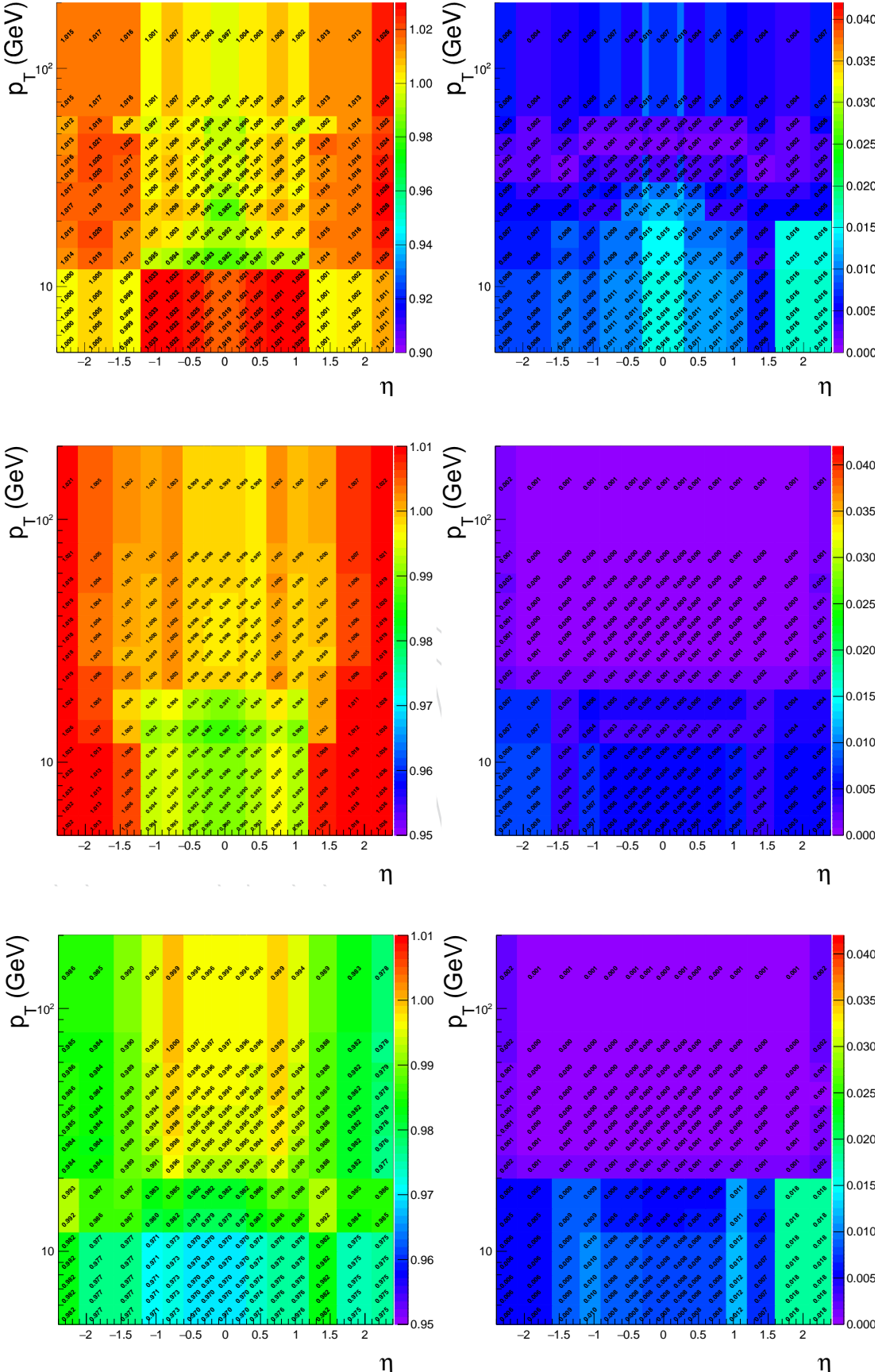


Figure 5: Left: Overall data to simulation scale factors for muons, as function of p_T and η . Right: Uncertainties on data to simulation scale factors for muons, as function of p_T and η . Results are shown for 2016 (top), 2017 (middle) and 2018 (bottom).

²³⁶ **4 Signal Modelling**

²³⁷ Referred to AN [19]

DRAFT

238 5 Background Estimation

239 Details on the background processes and their modeling is discussed in detail in AN [19]. In
 240 order to perform the differential measurements, the background four-lepton mass spectrum
 241 need to be extracted at the reconstruction level for each bin of the considered observable. In
 242 general, the background mass spectrum shape is not the same in every bin of the considered
 243 observable because the background does not have a resonance structure. The mass spectrum
 244 also can have non-negligible correlation with the observables.

245 In case of the irreducible backgrounds, the four-lepton mass spectra are extracted as the m_{4l}
 246 template shapes using Monte Carlo simulated events for each bin of the observable considered
 247 for the measurement. Similarly, in case of the reducible backgrounds the templates are built
 248 from the control regions in data.

In each differential bin of $p_T(4\ell)$ fractions of background events are presented in the Table 10.

Table 10: Estimated fraction of background events in each bin of $p_T(4\ell)$, for each final state using 2018 samples.

Background	final state	0 – 15	15 – 30	30 – 45	45 – 80	80 – 120	120 – 200	200 – 13000
qqZZ	2e2μ	0.483668	0.239196	0.130151	0.105276	0.0266332	0.011809	0.00326633
qqZZ	4e	0.459665	0.234399	0.136986	0.114916	0.0388128	0.00989346	0.00532725
qqZZ	4μ	0.492632	0.241203	0.110977	0.109173	0.0297744	0.0129323	0.00330827
ggZZ	2e2μ	0.310446	0.309859	0.191901	0.168134	0.0187793	0.000880282	0.0
ggZZ	4e	0.3085	0.306332	0.19247	0.17433	0.0169994	0.00136908	0.0
ggZZ	4μ	0.321332	0.319311	0.194863	0.150987	0.0128703	0.000638196	0.0
Z+X (CR)	4l	0.0992521	0.211153	0.209307	0.305327	0.120303	0.0483797	0.00627828

249

250 5.1 Estimation of ZZ normalization from Data

251 In earlier analyses, both the shape and the normalization for $q\bar{q} \rightarrow ZZ$ background were
 252 measured from simulation. However, with full Run 2 statistics, we can benefit from enough
 253 statistics to extend $m_{4\ell}$ range to fit ZZ normalization from data, still taking shapes from sim-
 254 ulation. This would help to improve the estimation and as well as reduction in uncertainties
 255 because luminosity and other theoretical uncertainties no longer contribute to the normaliza-
 256 tion. (studies in under validation)

257 6 Analysis Strategy

258 6.1 Event Selection

259 6.1.1 Trigger Selection

260 The events are required to have fired the High-Level Trigger paths described in subsection 2.1.
 261 Unlike in the Run I analysis, the trigger requirement does not depend on the selected final state:
 262 it is always the OR of all HLT paths. The reason is in Run II we will be targeting associated
 263 production modes that can come with additional leptons, thus improving trigger efficiency
 264 further.

265 6.1.2 Vertex Selection

266 The events are required to have at least one good primary vertex (PV) fulfilling the following
 267 criteria: high number of degree of freedom ($N_{PV} > 4$), collisions restricted along the z -axis
 268 ($z_{PV} < 24$ cm) and small radius of the PV ($r_{PV} < 2$ cm).

269 6.1.3 Z, ZZ and best ZZ Candidate Selection

270 The four-lepton candidates are built from what we call **selected leptons**, which are the tight
 271 leptons that pass the $SIP_{3D} < 4$ vertex constraint and the isolation cuts, where FSR photons
 272 are subtracted as described in [19]. A lepton cross cleaning is applied by discarding electrons
 273 which are within $\Delta R < 0.05$ of selected muons.

274 The construction and selection of four-lepton candidates proceeds according to the following
 275 sequence:

276 1. **Z candidates** are defined as pairs of selected leptons of opposite charge and matching
 277 flavour (e^+e^- , $\mu^+\mu^-$) that satisfy $12 < m_{\ell\ell(\gamma)} < 120$ GeV/ c^2 , where the Z candidate mass
 278 includes the selected FSR photons if any.

279 2. **ZZ candidates** are defined as pairs of non-overlapping Z candidates. The Z candidate
 280 with reconstructed mass $m_{\ell\ell}$ closest to the nominal Z boson mass is denoted as Z_1 , and
 281 the second one is denoted as Z_2 . ZZ candidates are required to satisfy the following list
 282 of requirements:

- 283 • **Ghost removal** : $\Delta R(\eta, \phi) > 0.02$ between each of the four leptons.
- 284 • **lepton p_T** : Two of the four selected leptons should pass $p_{T,i} > 20$ GeV/ c and
 $p_{T,j} > 10$ GeV/ c . FSR photons are used.
- 286 • **QCD suppression**: all four opposite-sign pairs that can be built with the four
 287 leptons (regardless of lepton flavor) must satisfy $m_{\ell\ell} > 4$ GeV/ c^2 . Here, se-
 288 lected FSR photons are not used in computing $m_{\ell\ell}$, since a QCD-induced low
 289 mass dilepton (eg. J/Ψ) may have photons nearby (e.g. from π_0).
- 290 • **Z_1 mass**: $m_{Z_1} > 40$ GeV/ c^2
- 291 • **'smart cut'**: defining Z_a and Z_b as the mass-sorted alternative pairing Z candi-
 292 dates (Z_a being the one closest to the nominal Z boson mass), require $NOT(|m_{Z_a} -$
 $m_Z| < |m_{Z_1} - m_Z| \text{ AND } m_{Z_b} < 12)$. Selected FSR photons are included in m_Z 's
 293 computations. This cut discards 4μ and $4e$ candidates where the alternative
 294 pairing looks like an on-shell Z + low-mass $\ell^+\ell^-$. (NB. In Run I, such a situa-
 295 tion was avoided by choosing the best ZZ candidate before applying kinematic
 296 cuts to it, most precisely before the $m_{Z_2} > 12$ GeV/ c^2 cut. The present smart
 297 cut allows to choose the best ZZ candidate after all kinematic cuts.)

- 299 • **four-lepton invariant mass:** $m_{4\ell} > 70 \text{ GeV}/c^2$ (selected FSR photons are in-
300 cluded).
- 301 3. Events containing at least one selected ZZ candidate form the **signal region**.
- 302 4. **Best ZZ candidate selection:** If more than one ZZ candidates survive the above selection,
303 we choose the one with Z_1 closest in mass to nominal Z boson mass and Z_2 from the
304 candidates whose lepton give higher p_T sum.

305 **6.2 Fiducial Volume Significance and Definition**

- 306 To minimize the model dependence, results are extracted in the fiducial volume that closely
matches with the detector geometry as shown in Figure 6.



Figure 6: Fiducial phase definition among different models.

- 307
- 308 The differential cross subsections are measured in a fiducial region in order to reduce the ef-
309 fects of model dependent acceptances. The fiducial selection mimics the reconstruction level
310 selection, which is optimised to detect a low mass ($m_H 125\text{GeV}$) Higgs boson decaying to 4 lep-
311 tons through two Z bosons. Since in the standard model there are multiple production modes,
312 the fiducial selection and measurement strategy are designed to be independent of how the

313 Higgs boson is produced. For this reason, the inclusion of isolation in the fiducial selection
 314 is necessary in order to make the reconstruction efficiency with respect to the fiducial volume
 315 independent of the number of jets.

316 The fiducial volume is defined to match closely the reconstruction level selection and is very
 317 similar to the definition used in Refs. [18]. With respect to the Run 1 analysis, the leptons are
 318 defined as “dressed” leptons rather than Born level leptons. Leptons are dressed by adding the
 319 four-momenta of leptons within $\Delta R < 0.3$ to the bare leptons. The fiducial lepton isolation cri-
 320 teria is also updated to match the Run 2 reconstruction level isolation. Leptons are considered
 321 isolated at generator level if the sum p_T of particles within a cone $\Delta R < 0.3$ is less than 0.35. The
 322 fiducial volume definition can be seen in Table 11. The fiducial volume acceptance for various
 323 SM production modes can be seen in Table 16.

Table 11: Summary of requirements and selections used in the definition of the fiducial phase space for the $H \rightarrow 4\ell$ cross subsection measurements.

Requirements for the $H \rightarrow 4\ell$ fiducial phase space	
Lepton kinematics and isolation	
leading lepton p_T	$p_T > 20 \text{ GeV}$
next-to-leading lepton p_T	$p_T > 10 \text{ GeV}$
additional electrons (muons) p_T	$p_T > 7(5) \text{ GeV}$
pseudorapidity of electrons (muons)	$ \eta < 2.5(2.4)$
p_T sum of all stable particles within $\Delta R < 0.3$ from lepton	less than $0.35 \cdot p_T$
Event topology	
existence of at least two SFOS lepton pairs, where leptons satisfy criteria above	
inv. mass of the Z_1 candidate	$40 \text{ GeV} < m(Z_1) < 120 \text{ GeV}$
inv. mass of the Z_2 candidate	$12 \text{ GeV} < m(Z_2) < 120 \text{ GeV}$
distance between selected four leptons	$\Delta R(\ell_i \ell_j) > 0.02$ for any $i \neq j$
inv. mass of any opposite sign lepton pair	$m(\ell^+ \ell^-) > 4 \text{ GeV}$
inv. mass of the selected four leptons	$105 \text{ GeV} < m_{4\ell} < 140 \text{ GeV}$
the selected four leptons must originate from the $H \rightarrow 4\ell$ decay	

324 6.3 Binning strategy for differential observables

Choice of bin boundaries and number of bins are two important aspects of differential measurements. With respect to the Run 1 analyses, we are benefitted from more statistic during Run 2 where data is recorded at 137 fb^{-1} with CMS detector. Sufficient statistics has helped to choose more fine binning for the observables than before. Bin boundaries are chosen in such a way that there is similar relative uncertainties on the expected cross section in the respective bins. Relative uncertainty (Δ_{rel}) is defined as:

$$\Delta_{rel}^i = \frac{d\sigma_{fid}^i}{\Delta_{tot}^i} \quad (3)$$

325 where $d\sigma_{fid}^i$ and Δ_{tot}^i are expected cross section and total uncertainty in bin i for a differential
 326 observable.

327 Table 12 shows the current choice of bin boundaries of $p_T(H)$ observables with details of ex-
 328 pected cross section and relative uncertainties in the bins.

Table 12: Differential cross section results for the pT4l observable.

Bin range (GeV)	$d\sigma_{fid}$ (fb)	Δ_{tot} (% fb)	Δ_{rel} (%)	δ_{stat} (% fb)	δ_{syst} (% fb)
0 - 10	0.34	+0.11 -0.096	+33 -28	+0.1 -0.091	+0.048 -0.031
10 - 20	0.53	+0.13 -0.11	+25 -21	+0.12 -0.11	+0.056 -0.037
20 - 30	0.42	+0.11 -0.097	+27 -23	+0.1 -0.093	+0.044 -0.027
30 - 45	0.43	+0.11 -0.094	+25 -22	+0.1 -0.089	+0.044 -0.029
45 - 80	0.52	+0.11 -0.1	+22 -19	+0.1 -0.092	+0.05 -0.038
80 - 120	0.25	+0.073 -0.062	+29 -25	+0.069 -0.06	+0.024 -0.018
120 - 200	0.18	+0.057 -0.048	+31 -26	+0.055 -0.046	+0.016 -0.011
200 - 13000	0.082	+0.036 -0.028	+44 -34	+0.035 -0.028	+0.008 -0.004

329 6.4 Unfolding

330 The effects of imperfect detector resolution can in general have an non-negligible impact on
 331 the shape of the distribution of the measured observables. For this reason, in case of the dif-
 332 ferential cross sections measurements, a procedure to correct for the detection efficiencies and
 333 resolution effects is applied. Throughout this document, this procedure will be referred to as
 334 the unfolding procedure, and the unfolded differential distributions will be referred to as dis-
 335 tributions at the fiducial level. Currently adopted procedure is “bin-by-bin unfolding”. This
 336 procedure for the unfolding of the detector effects from the observed distributions is the same
 337 as in Refs. [18] and [38]. The finite efficiencies and resolution effects are encoded in a detec-
 338 tor response matrix which describes how events migrate from a given observable bin at the
 339 fiducial level to a given bin at the reconstruction level. This matrix is diagonally dominant,
 340 with sizeable off-diagonal elements for observables involving jets. It is aimed we would also
 341 perform matrix inversion method as a validation tool for preceding method.

342 Examples of the efficiency matrices for gluon fusion and VBF production can be seen in Fig. 7.
 343 The matrices for the p_{TH} and N(jets) observables are shown.

344 6.5 Acceptance and other correction factors

345 In this section the acceptance and other correction factors while measuring the cross sections
 346 are discussed in details.

347 6.5.1 Acceptance

348 Ratio of the total number of events passing the fiducial level selectons $N_{fid.}$ to the total number
 349 of the generated events $N_{gen.}$ are is called acceptance as given in Equation 4.

$$A = \frac{N_{fid.}}{N_{gen.}} \quad (4)$$

350 6.5.2 Other correction factors

351 Measurement strategy and definition of the fiducial volume is optimized to:

- 352 • detect a low mass Higgs ($m_H=125.38$ GeV) boson decaying to 4 leptons through a
 353 pair of Z bosons
- 354 • keep the measurements independent of how the Higgs boson is produced.

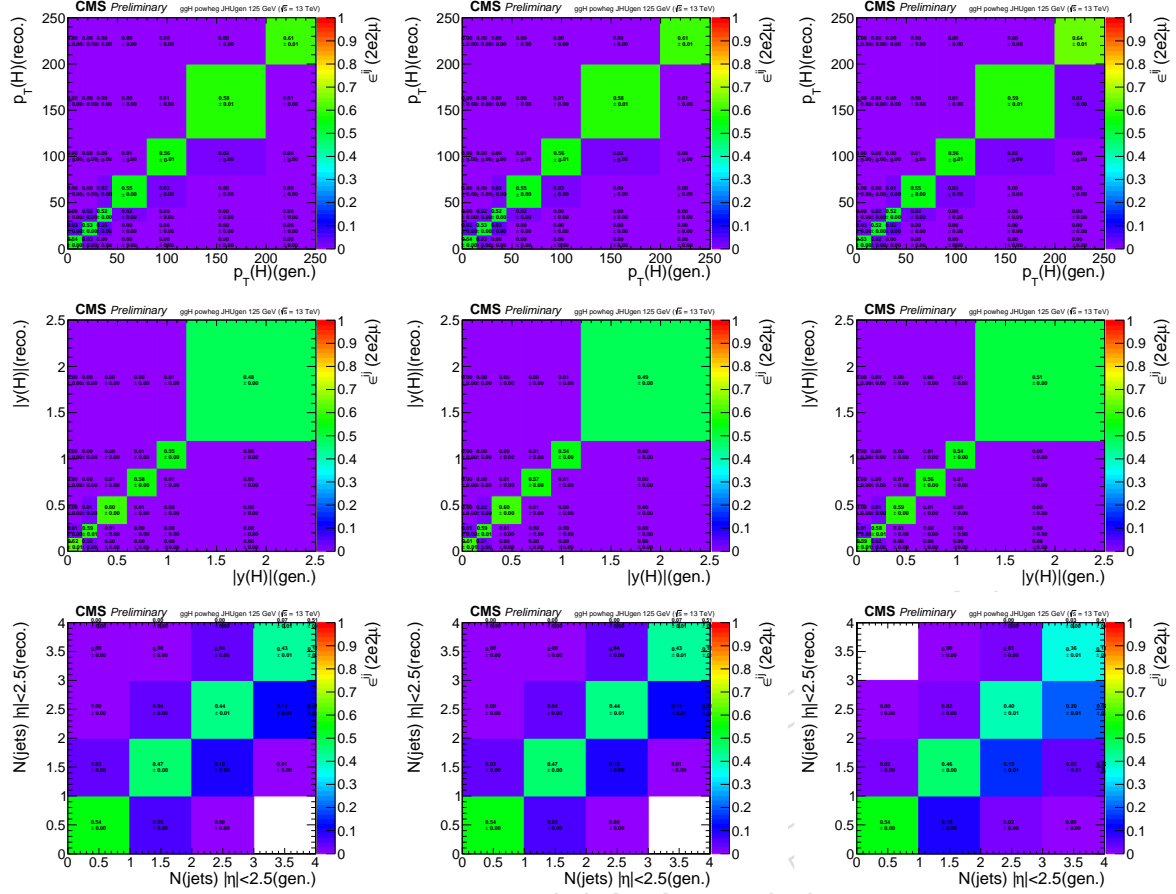


Figure 7: Efficiency matrices for the $p_{T\text{H}}$ (top) and y_{H} (middle) and N_{jets} (bottom) observables for gluon fusion production modes in the $2e2\mu$ final state in 2016 (left) 2017 (middle) and 2018 (right) (TBU).

For reconstruction efficiency to be independent of fiducial phase space, it is necessary to include isolation in the definition of fiducial phase space.

In case of associated production of Higgs with vector bosons where the bosons can decay leptonically, there is possibility that Higgs is reconstructed from wrong combination of leptons. This makes it necessary to consider such “wrong combination” events as a background in order to keep complete information from unbinned simultaneous fit of signal and background parameterizations to four-lepton invariant mass.

Also, signal events which pass the fiducial level selections but fail the reconstruction are accounted in the fiducial efficiency (ϵ) and the events which pass the reconstruction but fail the fiducial selections are referred to as “nonfiducial signal” events (f_{nonfid}) and are treated as a background as illustrated in Figure 8.

The summary of acceptance and other factors for full Run 2 periods are given Table. 16.

6.6 Statistical Procedure

We measure differential fiducial cross subsection for $pp \rightarrow H \rightarrow 4\ell$ by performing a maximum likelihood fit of the signal and background parameterisations to the observed 4ℓ mass distribution, $N_{\text{obs}}(m_{4\ell})$, and the fiducial cross subsection (σ_{fid}) is directly extracted from the fit. The systematic uncertainties are included in the form of nuisance parameters and are effectively

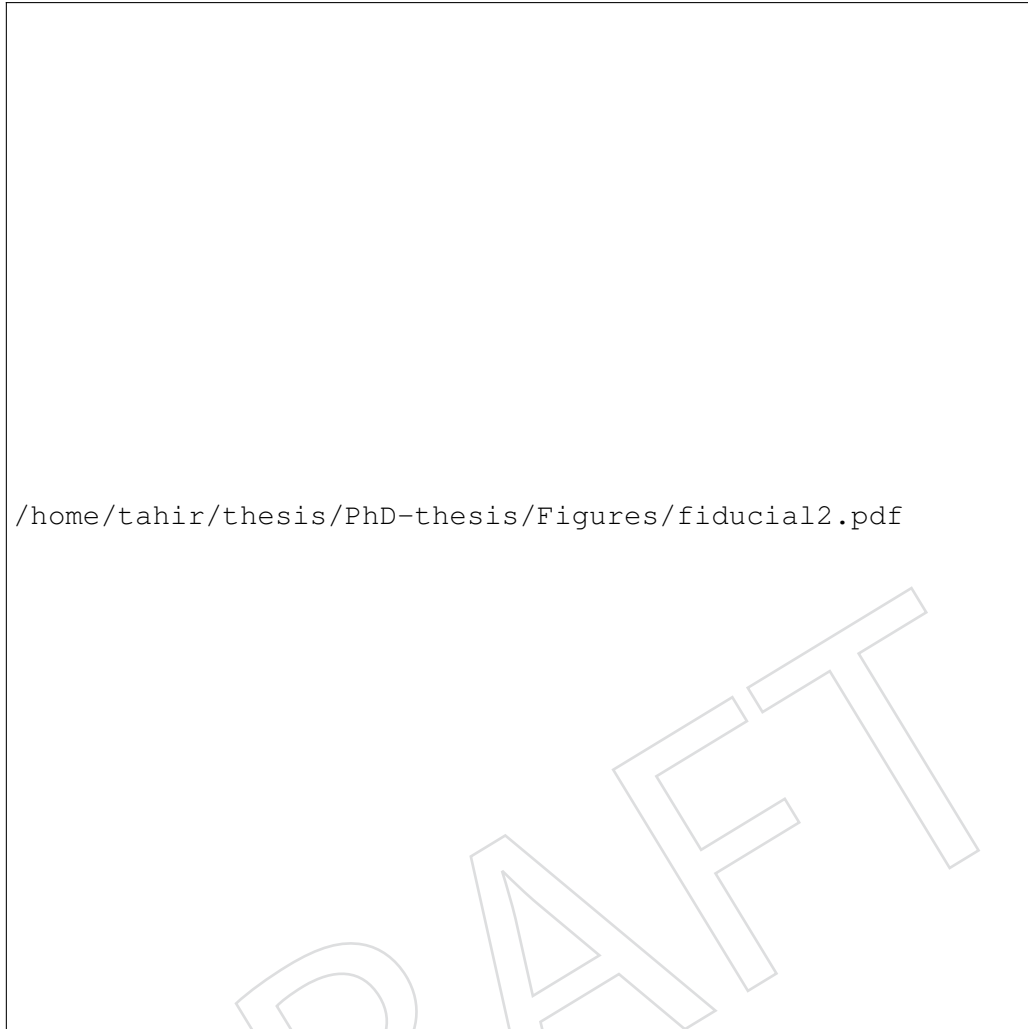


Figure 8: Fiducial efficiency(ϵ) and nonfiducial(f_{nonfid}) signal definition.

Table 13: Summary of different Standard Model signal models (2016).

Signal process	\mathcal{A}_{fid}	ϵ	f_{nonfid}	$(1 + f_{nonfid})\epsilon$
Individual Higgs boson production modes				
gg \rightarrow H (POWHEG) 125 GeV	0.397 ± 0.001	0.604 ± 0.001	0.051 ± 0.001	0.635 ± 0.001
VBF 125 GeV	0.446 ± 0.001	0.618 ± 0.002	0.039 ± 0.001	0.642 ± 0.002
WH 125 GeV	0.328 ± 0.001	0.593 ± 0.002	0.077 ± 0.001	0.638 ± 0.002
ZH 125 GeV	0.340 ± 0.002	0.608 ± 0.003	0.077 ± 0.002	0.655 ± 0.004
ttH 125 GeV	0.312 ± 0.002	0.585 ± 0.003	0.169 ± 0.004	0.684 ± 0.004

³⁷² integrated out in the fit procedure. The results are obtained using an asymptotic approach [39]
³⁷³ with a test statistic based on the profile likelihood ratio [40]. Following the models for signal
³⁷⁴ and background contributions described above, the number of expected events in each final

Table 14: Summary of different Standard Model signal models (2017).

Signal process	\mathcal{A}_{fid}	ϵ	f_{nonfid}	$(1 + f_{\text{nonfid}})\epsilon$
Individual Higgs boson production modes				
gg \rightarrow H (POWHEG) 125 GeV	0.403 ± 0.001	0.593 ± 0.001	0.056 ± 0.001	0.626 ± 0.001
VBF 125 GeV	0.445 ± 0.001	0.609 ± 0.001	0.044 ± 0.001	0.636 ± 0.001
WH 125 GeV	0.329 ± 0.001	0.583 ± 0.002	0.081 ± 0.001	0.631 ± 0.002
ZH 125 GeV	0.341 ± 0.002	0.594 ± 0.003	0.084 ± 0.002	0.644 ± 0.004
ttH 125 GeV	0.318 ± 0.003	0.589 ± 0.006	0.187 ± 0.007	0.699 ± 0.008

Table 15: Summary of different Standard Model signal models (2018).

Signal process	\mathcal{A}_{fid}	ϵ	f_{nonfid}	$(1 + f_{\text{nonfid}})\epsilon$
Individual Higgs boson production modes				
gg \rightarrow H (POWHEG) 125 GeV	0.403 ± 0.001	0.599 ± 0.001	0.055 ± 0.001	0.632 ± 0.001
VBF 125 GeV	0.443 ± 0.001	0.617 ± 0.002	0.043 ± 0.001	0.644 ± 0.002
WH 125 GeV	0.330 ± 0.001	0.625 ± 0.002	0.075 ± 0.001	0.672 ± 0.002
ZH 125 GeV	0.339 ± 0.002	0.629 ± 0.003	0.083 ± 0.002	0.681 ± 0.004
ttH 125 GeV	0.314 ± 0.002	0.589 ± 0.003	0.184 ± 0.004	0.698 ± 0.004

Table 16: Summary of different Standard Model signal models.(Full Run 2)

Signal process	\mathcal{A}_{fid}	ϵ	f_{nonfid}	$(1 + f_{\text{nonfid}})\epsilon$
Individual Higgs boson production modes				
gg \rightarrow H (POWHEG) 125 GeV	0.402 ± 0.001	0.598 ± 0.002	0.054 ± 0.001	0.631 ± 0.002
VBF 125 GeV	0.445 ± 0.002	0.615 ± 0.002	0.043 ± 0.001	0.641 ± 0.003
WH 125 GeV	0.329 ± 0.002	0.604 ± 0.003	0.078 ± 0.002	0.651 ± 0.004
ZH 125 GeV	0.340 ± 0.003	0.613 ± 0.005	0.082 ± 0.004	0.663 ± 0.006
ttH 125 GeV	0.315 ± 0.004	0.588 ± 0.007	0.181 ± 0.009	0.694 ± 0.010

375 state f and in each bin i of a considered observable is expressed as a function of $m_{4\ell}$ given by:

$$\begin{aligned}
 N_{\text{obs}}^{f,i}(m_{4\ell}) &= N_{\text{fid}}^{f,i}(m_{4\ell}) + N_{\text{nonfid}}^{f,i}(m_{4\ell}) + N_{\text{nonres}}^{f,i}(m_{4\ell}) + N_{\text{bkg}}^{f,i}(m_{4\ell}) \\
 &= \epsilon_{i,j}^f \cdot \left(1 + f_{\text{nonfid}}^{f,i}\right) \cdot \sigma_{\text{fid}}^{f,j} \cdot \mathcal{L} \cdot \mathcal{P}_{\text{res}}(m_{4\ell}) \\
 &\quad + N_{\text{nonres}}^{f,i} \cdot \mathcal{P}_{\text{nonres}}(m_{4\ell}) + N_{\text{bkg}}^{f,i} \cdot \mathcal{P}_{\text{bkg}}(m_{4\ell}),
 \end{aligned} \tag{5}$$

376 The parameter $\sigma_{\text{fid}}^{f,j}$ is the signal cross subsection in bin j of the fiducial phase space, and it is the
 377 parameter extracted from the measurement.

378 The shape of the resonant signal contribution, $\mathcal{P}_{\text{res}}(m_{4\ell})$, is described by a double-sided Crys-
 379 tal Ball function, as described in previous sections, whose normalisation is proportional to
 380 the fiducial cross subsection. The shape of the non-resonant signal contribution, $\mathcal{P}_{\text{nonres}}(m_{4\ell})$,
 381 which arises from WH, ZH, and ttH production where one of the leptons from the Higgs bo-
 382 son decay is lost or not selected, is empirically modelled by a Landau distribution whose shape
 383 parameters are constrained in the fit to be within a range determined from simulation. This
 384 contribution is treated as a background and hereafter we will refer to this contribution as the
 385 “non-resonant signal” contribution.

386 The $\epsilon_{i,j}^f$ represents the detector response matrix that maps the number of expected events in
 387 a given observable bin j at the fiducial level to the number of expected events in the bin i at

388 the reconstruction level. The f_{nonfid}^i fraction describes the ratio of the non-fiducial and fiducial
 389 signal contribution in bin i at the reconstruction level. The efficiency is measured using signal
 390 simulation samples and corrected for residual differences between data and simulation. In the
 391 case of the integrated fiducial cross subsection measurement the efficiencies reduce to a single
 392 values.

393 An additional resonant contribution arises from events which are reconstructed but which do
 394 not originate from the fiducial phase space. These events are due to detector effects which
 395 cause differences between the quantities used for the fiducial phase space definition and the
 396 analogous quantities at the reconstruction level. This contribution is treated as background
 397 and is referred to as the “non-fiducial signal” contribution. The shape of these events is verified
 398 using simulation to be identical to the shape of the fiducial signal and its normalisation is fixed
 399 to be a fraction of the fiducial signal component. The value of this fraction, which we denote
 400 by f_{nonfid} , which has been determined from simulation for each of the studied signal models.

401 The variation between different models of the factor in the final column of Table 16, $(1 +$
 402 $f_{\text{nonfid}})\epsilon$, is directly related to the model dependence of the measurement. The model depen-
 403 dence is defined as the variation of the factor $(1 + f_{\text{nonfid}})\epsilon$ when the relative fraction of each
 404 the production modes are varied within their experimental constraints.

405 6.7 Extraction of differential $H \rightarrow 4\ell$ cross section

406 6.7.1 Considered observables

407 The differential fiducial cross sections are presented as a function of several kinematic observ-
 408 ables which are sensitive to the Higgs-boson production mechanisms. Examples are rapidity
 409 and transverse momentum of the four-lepton system, associated jet multiplicity and transverse
 410 momentum of the leading jet $p_T(H)$ or $p_T(4\ell)$, $|y(H)|$ or $|y(4\ell)|$, $N(\text{jets})$, and $p_T(\text{jet})$. These
 411 measurements are important to test the Standard Model predictions in the Higgs sector and
 412 can be used to constrain phase spaces of many theories beyond the Standard Model. In addition,
 413 several other observables related to decay of Higgs boson are also studied. These include
 414 m_{Z_1} , m_{Z_2} , ϕ , $\cos\theta^*$ and several other observables which are sensitive to spin and CP or Higgs
 415 bosons.

416 6.7.2 Choice of bin boundaries

417 For each kinematic or differential observable, selection procedure of the binning boundaries
 418 has been optimized in order to have a similar expected measured cross-section for every bin.
 419 Relative uncertainties for p_T of Higgs observables are given in Table. 17.

420 6.7.3 Applying the Statistical Procedure

421 The fiducial differential cross section is extracted in the bins of kinematic observables at the
 422 fiducial level following the procedure outlined in previous. For signal yields, mass spectrum
 423 of signal is built in each cell of the response matrix using a Double Crystal Ball (DCB) function,
 424 similar to what was done in Ref. [?]. In practice, the same parameters of the CB function are
 425 used in each cell and the systematic uncertainties assigned on the energy scale and resolution
 426 generally cover discrepancy of signal mass spectrum among each cell.

427 Examples of the fitted signal line shapes for differential bins of $p_T(H)$ from $gg \rightarrow H$ (POWHEG
 428 + JHUGEN 125 GeV 2018 sample) in the individual final states are shown in Figure 31, and
 429 examples of the efficiency matrices for $p_T(H)$ for the $2e2\mu$ final state are shown in Fig 10. Many
 430 more examples can be seen in Appendix A.

Table 17: Differential cross section results for the $p_T(H)$ observable.

Bin range (GeV)	$d\sigma_{fid}$ (fb)	Δ_{tot} (% fb)	Δ_{rel} (%)	δ_{stat} (% fb)	δ_{syst} (% fb)
CMS preliminary choice					
0 - 10	0.34	+0.11 −0.096	+33 −28	+0.1 −0.091	+0.048 −0.031
10 - 20	0.53	+0.13 −0.11	+25 −21	+0.12 −0.11	+0.056 −0.037
20 - 30	0.42	+0.11 −0.097	+27 −23	+0.1 −0.093	+0.044 −0.027
30 - 45	0.43	+0.11 −0.094	+25 −22	+0.1 −0.089	+0.044 −0.029
45 - 80	0.52	+0.11 −0.1	+22 −19	+0.1 −0.092	+0.05 −0.038
80 - 120	0.25	+0.073 −0.062	+29 −25	+0.069 −0.06	+0.024 −0.018
120 - 200	0.18	+0.057 −0.048	+31 −26	+0.055 −0.046	+0.016 −0.011
200 - 13000	0.082	+0.036 −0.028	+44 −34	+0.035 −0.028	+0.008 −0.004
Total bins = 8	$\sigma_{fid} = \sum d\sigma_{fid} = 2.8$ (fb)				

431 Figure 11 shows the four lepton mass distributions for an Asimov dataset generated using SM
 432 cross section values and efficiencies from the $gg \rightarrow H$ production mode from POWHEG+JHUGEN,
 433 and resulting fitted values of PDFs of signal and background for different bins of $p_T(H)$ (all fi-
 434 final states combined).

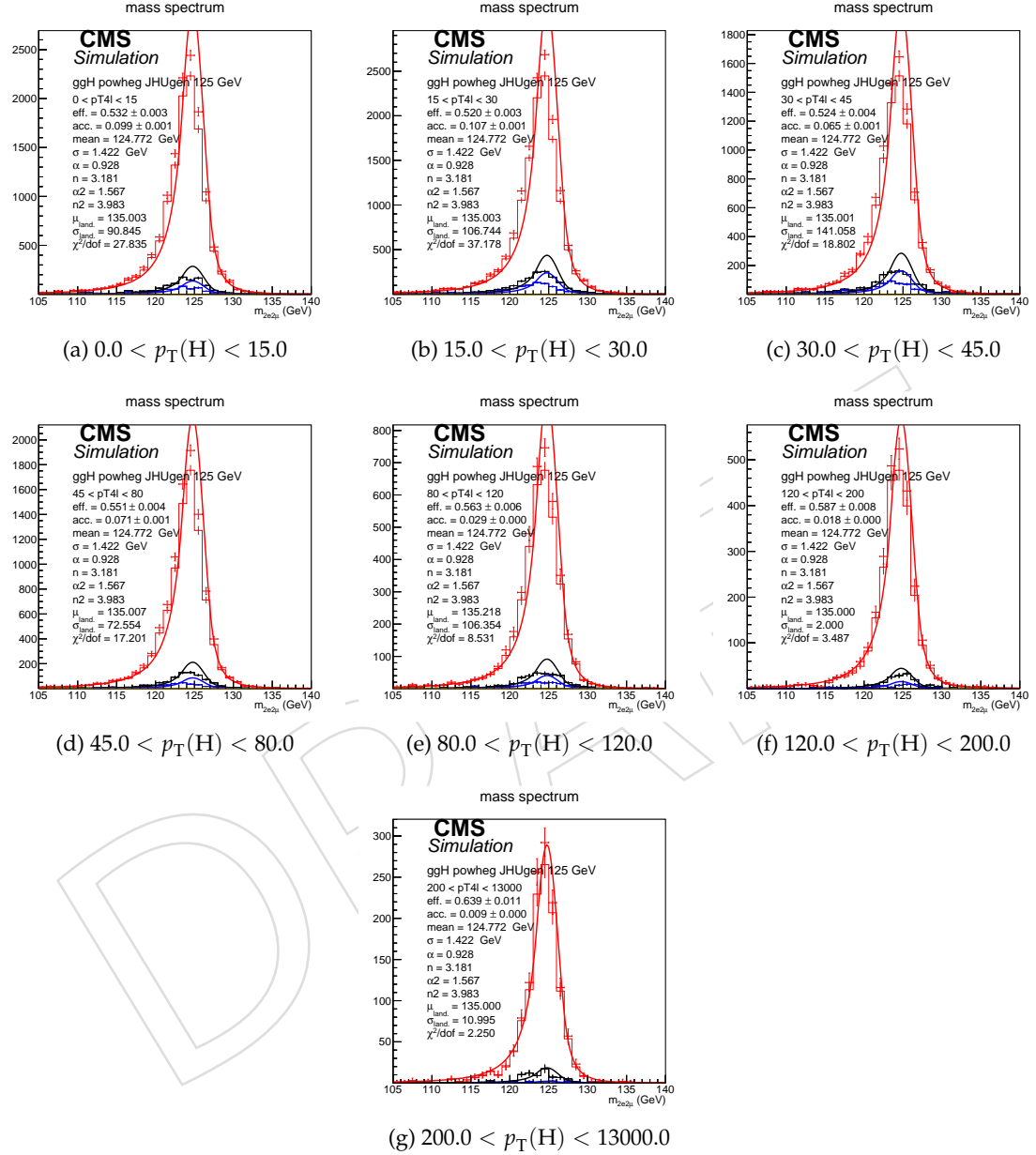


Figure 9: Example signal shapes at reconstruction level for a resonance of $m(4\ell)$ in $2e2\mu$ final state for the $gg \rightarrow H$ production mode from POWHEG+JHUGEN in different bins of $p_{\text{T}}(\text{H})$. The black curve represents events which do not pass the fiducial volume selection. The curve has no effect on the result.

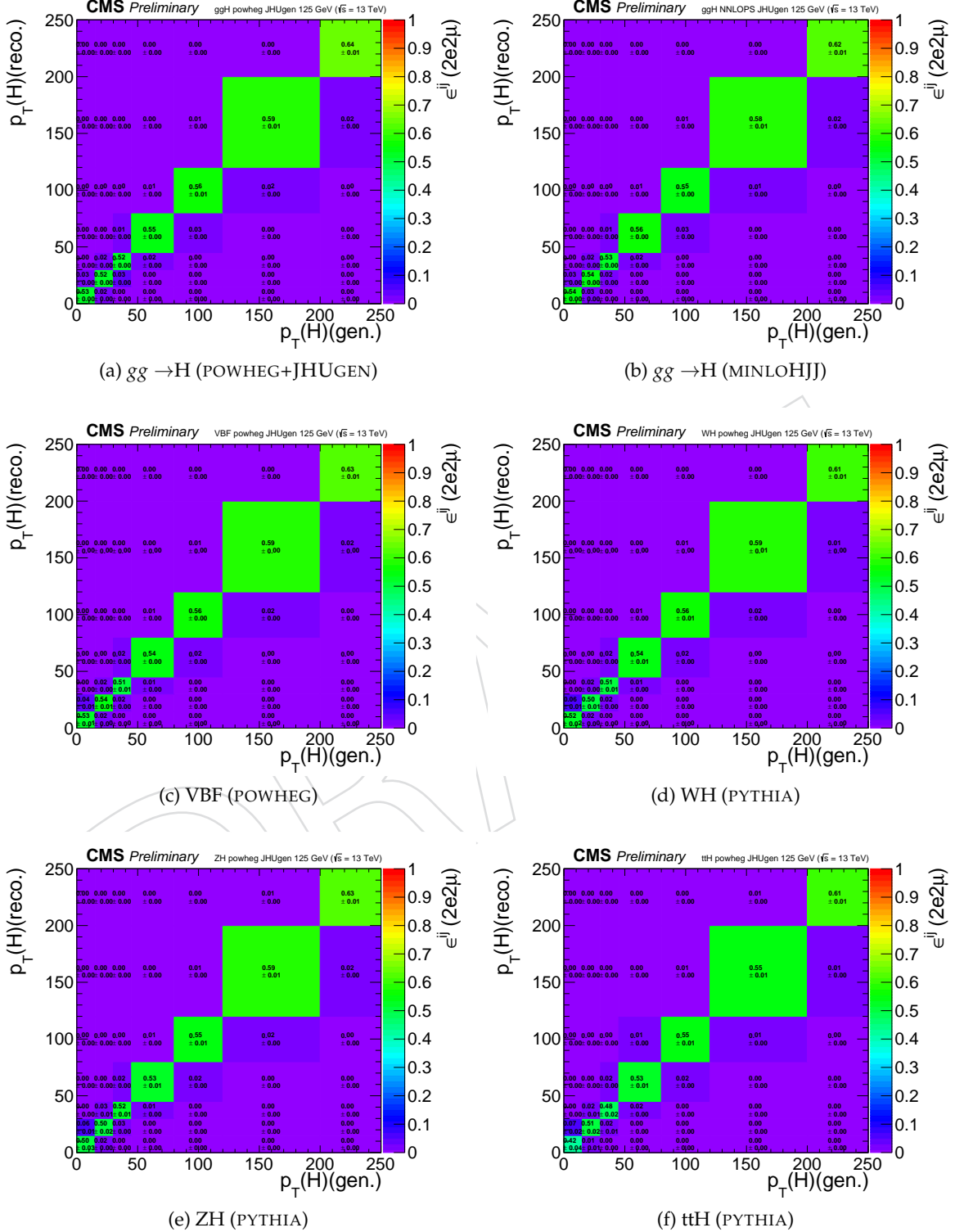


Figure 10: Efficiency response matrices for $p_T(H)$ for different SM production modes in the $2e2\mu$ final state using 2018 samples.

⁴³⁵ **6.8 Interpretations**

⁴³⁶ To be updated

⁴³⁷ **6.8.1 κ -framework**

⁴³⁸ To be updated

⁴³⁹ **6.8.2 Effective Field Theory**

⁴⁴⁰ To be updated.

⁴⁴¹ **6.8.3 κ -framework**

DRAFT

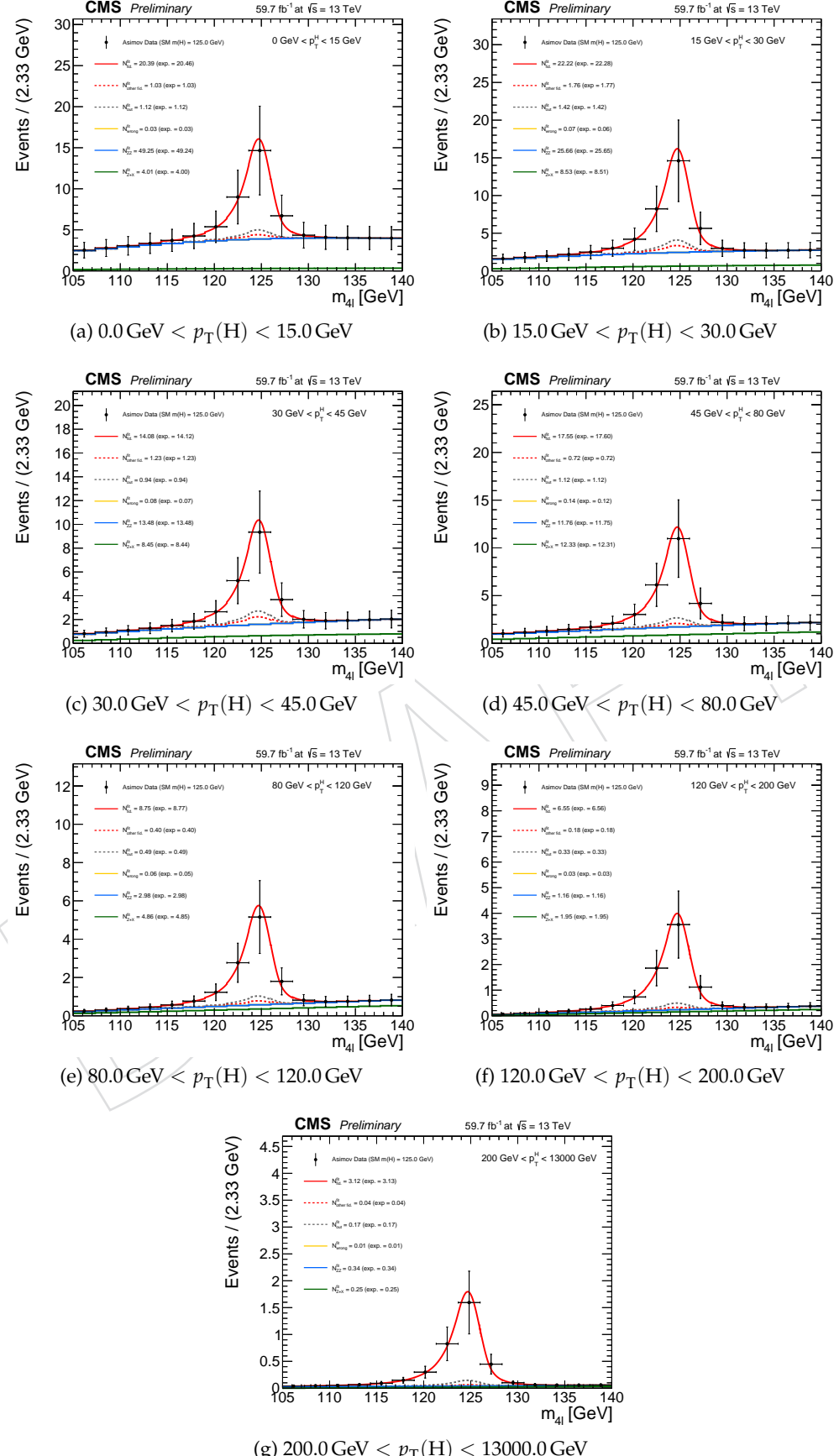


Figure 11: Four lepton mass distributions for an Asimov dataset generated using SM cross section values and SM efficiencies where the $gg \rightarrow H$ prediction is from POWHEG+JHUGEN and resulting fitted values of PDFs of signal and background for different bins of $p_T(\text{H})$ (all final states combined).

442 7 Systematic uncertainties

443 The main experimental uncertainties which affect both signal and background are the uncer-
 444 tainty on the integrated luminosity (from to 2.3% to 2.6%, depending on the data taking period)
 445 and the uncertainty on the lepton identification and reconstruction efficiency (ranging from 1
 446 to 2.5% and from 11 to 15.5% on the overall yields, in the 4μ and $4e$ channels, respectively).
 447 Experimental uncertainties for the reducible background estimation, described in Section ??,
 448 vary between 6% to 32% from the variation of the fake rates. The mismatch in the composition
 449 of backgrounds between the samples where the fake rate is derived and where it is applied
 450 accounts for about 30%.

451 The uncertainty of the lepton energy scale is assessed by propagating down to the four-leptons
 452 invariant mass the uncertainty associated the lepton momentum corrections on each individual
 453 lepton. The uncertainty is treated as uncorrelated (all up or all down). The new four-leptons
 454 invariant mass obtained this way is then fitted with only the mean value floating. The differ-
 455 ence between the new mean value and the default one gives an estimation of the impact of the
 456 lepton energy scale. The values are reported in the Table 18, together with the estimation of the
 457 impact of lepton momentum resolution, following a similar procedure.

Table 18: Difference (in %) between the nominal mean and width of the four-leptons Higgs mass distribution and those where the lepton momentum scale and resolution uncertainties have been propagated.

	4e	4μ	$2e2\mu$
Scale Difference (%)	0.087	0.049	0.069
Resolution Difference (%)	17	12	17

458 The results obtained this way suggest that the uncertainties from 2016 (20% on the resolution,
 459 0.3% for the $4e$ channel for scale) are still valid.

460 Theoretical uncertainties which affect both the signal and background estimation include un-
 461 certainties from the renormalization and factorization scale and choice of PDF set. The uncer-
 462 tainty from the renormalization and factorization scale is determined by varying these scales
 463 between 0.5 and 2 times their nominal value while keeping their ratio between 0.5 and 2. In the
 464 case of ggF production mode, the QCD scale uncertainty is broken down to 9 different sources.
 465 The renormalization and factorization scale affect the overall cross section, the migration of
 466 the stage1.1 bins in different Higgs pT and number of jets, top loop effects are treated as inde-
 467 pendent uncertainties, and correlated among different stage 1.1 bins. The numbers are shown
 468 in Fig ???. The uncertainty from the PDF set is determined by taking the root mean square of
 469 the variation when using different replicas of the default NNPDF set. PDF uncertainty arises
 470 from uncertainty is also taken into account. On the background, an additional uncertainty of
 471 10% on the K factor used for the $gg \rightarrow ZZ$ prediction is applied as described in Section ???. A
 472 systematic uncertainty of 2% on the branching ratio of $H \rightarrow ZZ \rightarrow 4\ell$ only affects the signal
 473 yield. In the case of event categorization, experimental and theoretical uncertainties which ac-
 474 count for possible migration of signal and background events between categories are included.
 475 The main sources of uncertainty on the event categorization include the QCD scale, PDF set,
 476 and the modeling of hadronization and the underlying event. These uncertainties amount to
 477 between 4–20% for the signal and 3–20% for the background depending on the category. The
 478 lower range corresponds to the VBF and VH processes and the upper range corresponds to the
 479 $gg \rightarrow H$ process yield in the VBF-2jet-tagged category. Additional uncertainties come from the
 480 imprecise knowledge of the jet energy scale (from 2% for the $gg \rightarrow H$ yield in the untagged
 481 category to 22% for $gg \rightarrow H$ yield in the VBF-2jet-tagged category) and b-tagging efficiency

⁴⁸² and mistag rate (up to 10% in the $t\bar{t}H$ -tagged category). In the cross section measurement, the
⁴⁸³ signal cross section uncertainties arise from theoretical sources are removed.

Table 19: Summary of the experimental systematic uncertainties in the $H \rightarrow 4\ell$ measurements of 2016, 2017 and 2018 data.

Summary of relative systematic uncertainties			
Common experimental uncertainties			
	2016	2017	2018
Luminosity	2.6 %	2.3 %	2.5 %
Lepton identification/reconstruction efficiencies	1.2 – 15.5 %	1.1 – 12 %	0.7 – 11 %
Background related uncertainties			
Reducible background ($Z+X$)	31 – 42 %	31 – 38 %	31 – 37 %
Signal related uncertainties			
Lepton energy scale	0.04 – 0.3 %	0 %	0 %
Lepton energy resolution	20 %	20 %	20 %

Table 20: Summary of the theory systematic uncertainties in the $H \rightarrow 4\ell$ measurements for the inclusive analysis

Summary of inclusive theory uncertainties	
QCD scale (gg)	± 3.9 %
PDF set (gg)	± 3.2 %
Bkg K factor (gg)	± 10 %
QCD scale (VBF)	+0.4/-0.3 %
PDF set (VBF)	± 2.1 %
QCD scale (WH)	+0.5/-0.7 %
PDF set (WH)	± 1.9 %
QCD scale (ZH)	+3.8/-3.1 %
PDF set (ZH)	± 1.6 %
QCD scale ($t\bar{t}H$)	+5.8/-9.2 %
PDF set ($t\bar{t}H$)	± 3.6 %
BR($H \rightarrow ZZ \rightarrow 4\ell$)	2 %
QCD scale ($q\bar{q} \rightarrow ZZ$)	+3.2/-4.2 % %
PDF set ($q\bar{q} \rightarrow ZZ$)	+3.1/-3.4 %
Electroweak corrections ($q\bar{q} \rightarrow ZZ$)	± 0.1 %

⁴⁸⁴ 7.1 Systematic uncertainties treatment when combining the data sets

⁴⁸⁵ In this Section we describe how different systematic uncertainties are treated when combining
⁴⁸⁶ the data sets. The theoretical uncertainties are correlated. All the experimental systematics are
⁴⁸⁷ treated independently.

⁴⁸⁸ In this subsection we summarize the status of the analysis after selection, showing the inputs to
⁴⁸⁹ the final results, namely the event yields and errors in the full signal region and in a restricted
⁴⁹⁰ $m_{4\ell}$ range, and the distributions of the main kinematic variables in data and MC.

⁴⁹¹ 7.1.1 Signal Region Yields

⁴⁹² The number of candidates observed in data and the expected yields for the backgrounds and
⁴⁹³ Higgs boson signal after the full event selection are reported in Table 22 for the full range of
⁴⁹⁴ $m_{4\ell}$. Table ?? shows the expected and observed yields for each of the 22 event categories, for a
⁴⁹⁵ $118 < m_{4\ell} < 130$ GeV mass window around the Higgs boson peak.

Table 21: The number of expected background and signal events and number observed candidates after full analysis selection, for each final state, for the full mass range $m_{4\ell} > 70$ GeV, for an integrated luminosity of 137 fb^{-1} . Signal and ZZ backgrounds are estimated from Monte Carlo simulation, Z+X is estimated from data.

Channel	4μ	$4e$	$2e2\mu$	$4l$
qqZZ	1414.85	748.64	1835.05	3998.54
ggZZ	268.48	163.45	399.78	831.70
ZX	112.84	48.62	151.71	313.18
EW bkg	15.13	12.73	27.83	55.69
Sum of backgrounds	1811.30	973.45	2414.36	5199.11
Signal ($m_H = 125$ GeV)	95.27	46.01	118.53	259.82
Total expected	1906.57	1019.46	2532.90	5458.93
Data	1970	1032	2646	5648

⁴⁹⁶ 7.1.2 Signal Region Distributions

⁴⁹⁷ The reconstructed four-lepton invariant mass distribution is shown in Figure 14 for the full
⁴⁹⁸ dataset, and compared to expectations from the SM backgrounds, first for the full mass range,
⁴⁹⁹ and then zooming on the low-mass range and high-mass range. In Figure 15, the same dis-
⁵⁰⁰ tributions are shown split by final state ($4e$, 4μ , and $2e2\mu$), for the two same mass ranges. In
⁵⁰¹ Figure ??, they are split by event category, for the low-mass range. The SM background dis-
⁵⁰²tributions are obtained combining the rate normalization from data-driven methods and knowl-
⁵⁰³edge on shapes taken from the MC samples.

⁵⁰⁴

⁵⁰⁵ The reconstructed dilepton invariant masses selected as Z_1 and Z_2 are shown in Figures ??
⁵⁰⁶ together with their correlation, both full range of $m_{4\ell}$ and focusing on a $118 < m_{4\ell} < 130$ GeV
⁵⁰⁷ mass window around the Higgs boson peak.

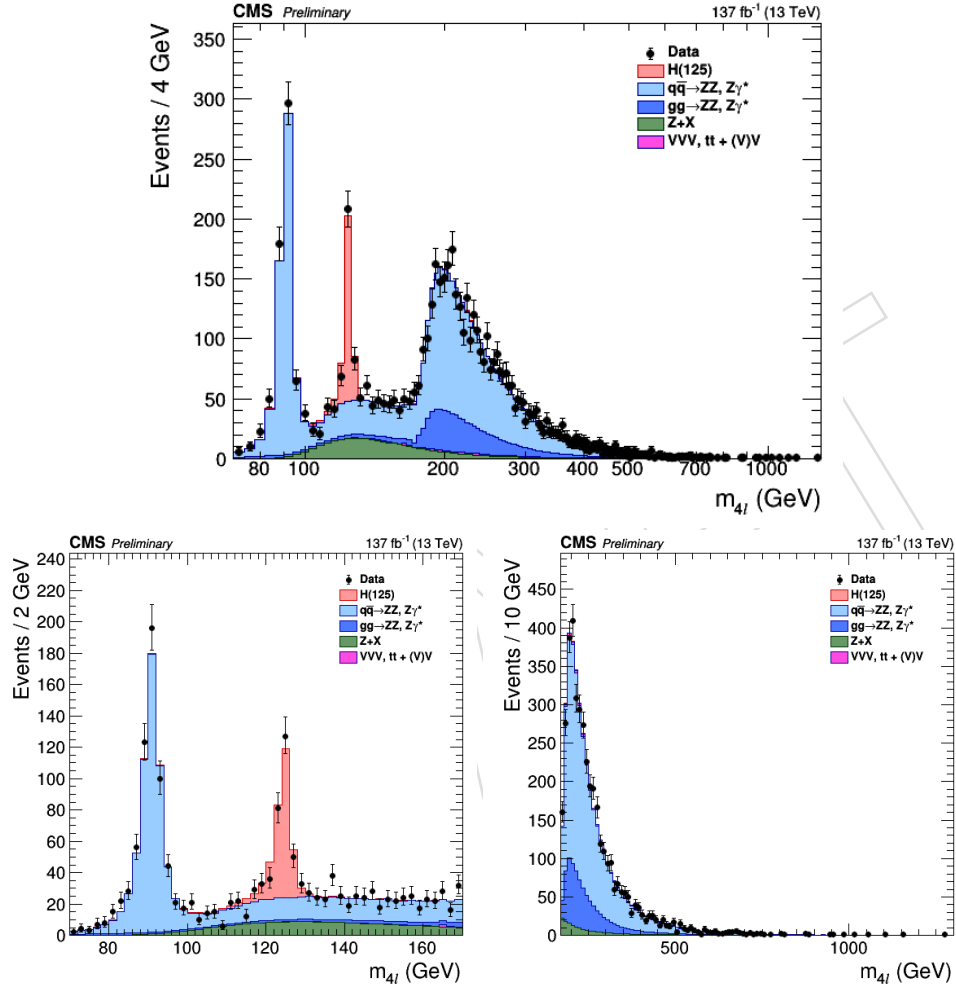


Figure 12: Distribution of the four-lepton reconstructed invariant mass $m_{4\ell}$ in the full mass range (top) and the low-mass range (bottom left) and high-mass range (bottom right). Points with error bars represent the data and stacked histograms represent expected distributions. The 125 GeV Higgs boson signal and the ZZ backgrounds are normalized to the SM expectation, the Z+X background to the estimation from data.

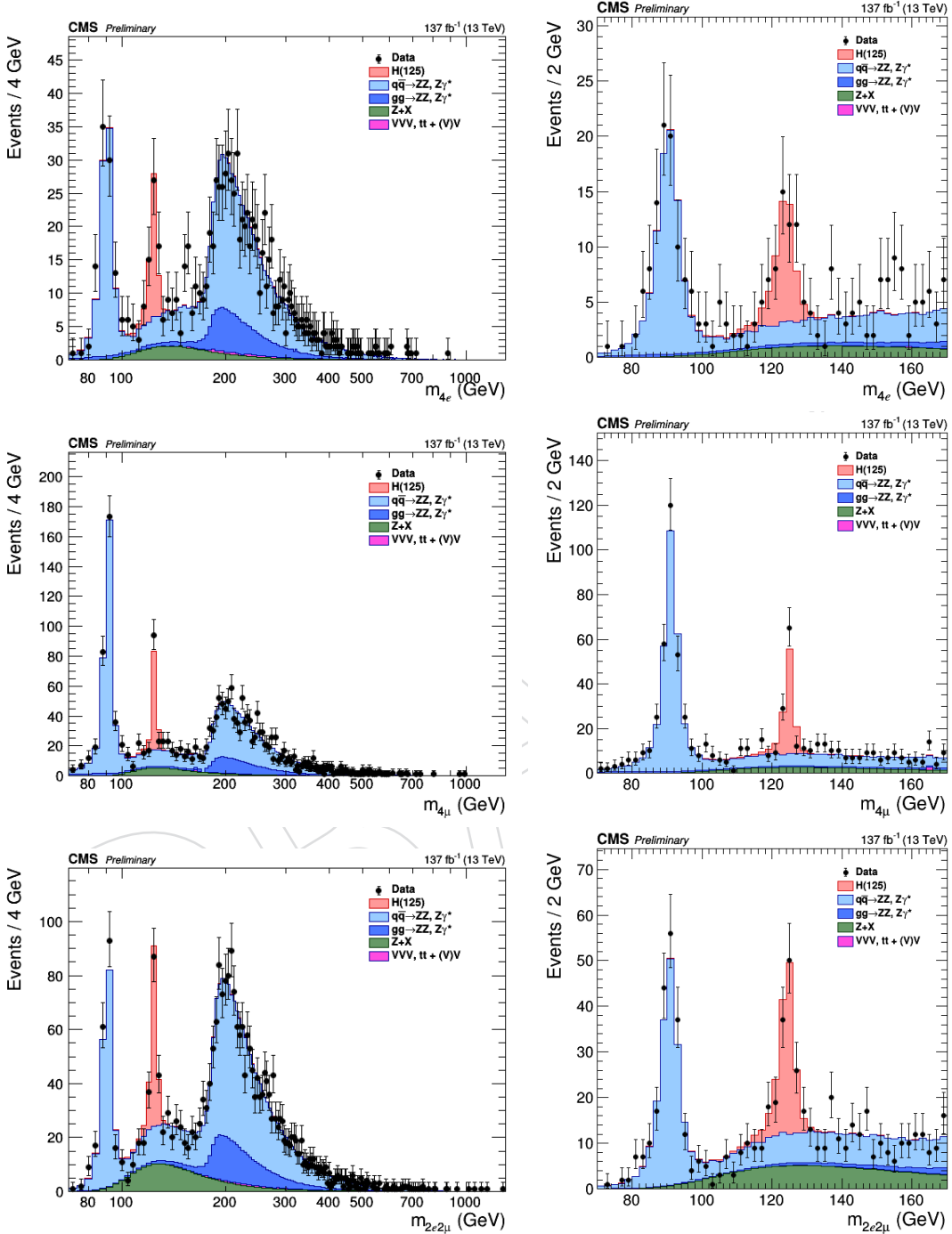
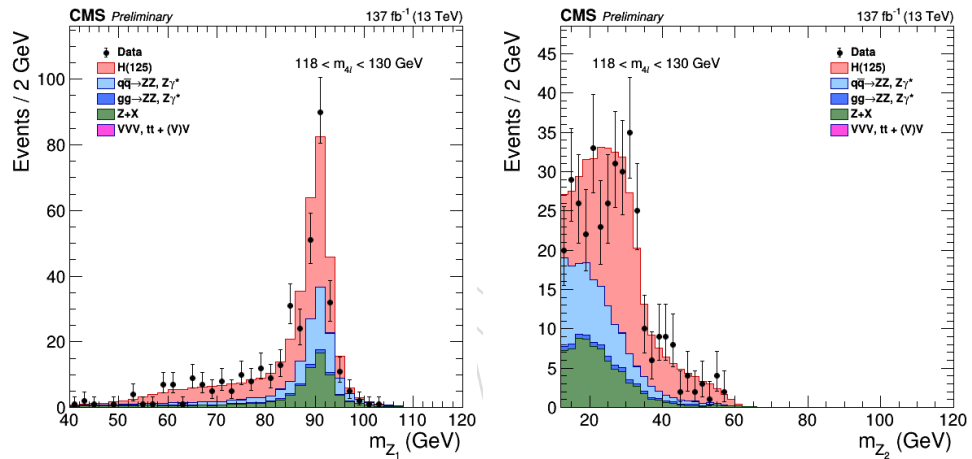


Figure 13: Distribution of the four-lepton reconstructed mass in several sub-channels: $4e$ (top), 4μ (middle), $2e2\mu$ for the low-mass range (bottom) for the full mass range (left) and the low-mass range (right).



Distribution of the Z_1 (left) and Z_2 (right) reconstructed invariant masses for the full mass range (left) and the low mass ($118 < m_{4\ell} < 130$ GeV) range (right). The stacked histograms and the gray scale represent expected distributions, and points represent the data. The 125 GeV Higgs boson signal and the ZZ backgrounds are normalized to the SM expectation, the Z+X background to the estimation from data.

508 8 Results

509 In this section, we describe the methods used for the estimation of the significance of the ex-
 510 cess of events above the SM backgrounds observed in the low-mass region, and of the signal
 511 strength, i.e. its cross section normalized to the one expected for a SM Higgs.

512 To exploit all the properties of the resonance under study or search, a multi-dimensional fit is
 513 implemented. For each of the categories defined in Section ??, the variable used in the maxi-
 514 mum likelihood fit is the four-lepton mass without kinematic refitting $m_{4\ell}$.

515 8.1 Yields and distributions

516 In this subsection we summarize the status of the analysis after selection, showing the inputs to
 517 the final results, namely the event yields and errors in the full signal region and in a restricted
 518 $m_{4\ell}$ range, and the distributions of the main kinematic variables in data and MC.

519 8.1.1 Signal Region Yields

520 The number of candidates observed in data and the expected yields for the backgrounds and
 521 Higgs boson signal after the full event selection are reported in Table 22 for the full range of
 522 $m_{4\ell}$. Table ?? shows the expected and observed yields for each of the 22 event categories, for a
 523 $118 < m_{4\ell} < 130$ GeV mass window around the Higgs boson peak.

Table 22: The number of expected background and signal events and number observed candi-
 dates after full analysis selection, for each final state, for the full mass range $m_{4\ell} > 70$ GeV, for
 an integrated luminosity of 137 fb^{-1} . Signal and ZZ backgrounds are estimated from Monte
 Carlo simulation, Z+X is estimated from data.

Channel	4μ	$4e$	$2e2\mu$	$4l$
qqZZ	1414.85	748.64	1835.05	3998.54
ggZZ	268.48	163.45	399.78	831.70
ZX	112.84	48.62	151.71	313.18
EW bkg	15.13	12.73	27.83	55.69
Sum of backgrounds	1811.30	973.45	2414.36	5199.11
Signal ($m_H = 125$ GeV)	95.27	46.01	118.53	259.82
Total expected	1906.57	1019.46	2532.90	5458.93
Data	1970	1032	2646	5648

524 8.1.2 Signal Region Distributions

525 The reconstructed four-lepton invariant mass distribution is shown in Figure 14 for the full
 526 dataset, and compared to expectations from the SM backgrounds, first for the full mass range,
 527 and then zooming on the low-mass range and high-mass range. In Figure 15, the same dis-
 528 tributions are shown split by final state ($4e$, 4μ , and $2e2\mu$), for the two same mass ranges. In
 529 Figure ??, they are split by event category, for the low-mass range. The SM background distri-
 530 butions are obtained combining the rate normalization from data-driven methods and knowl-
 531 edge on shapes taken from the MC samples.

532

533 The reconstructed dilepton invariant masses selected as Z_1 and Z_2 are shown in Figures ??
 534 together with their correlation, both full range of $m_{4\ell}$ and focusing on a $118 < m_{4\ell} < 130$ GeV
 535 mass window around the Higgs boson peak.

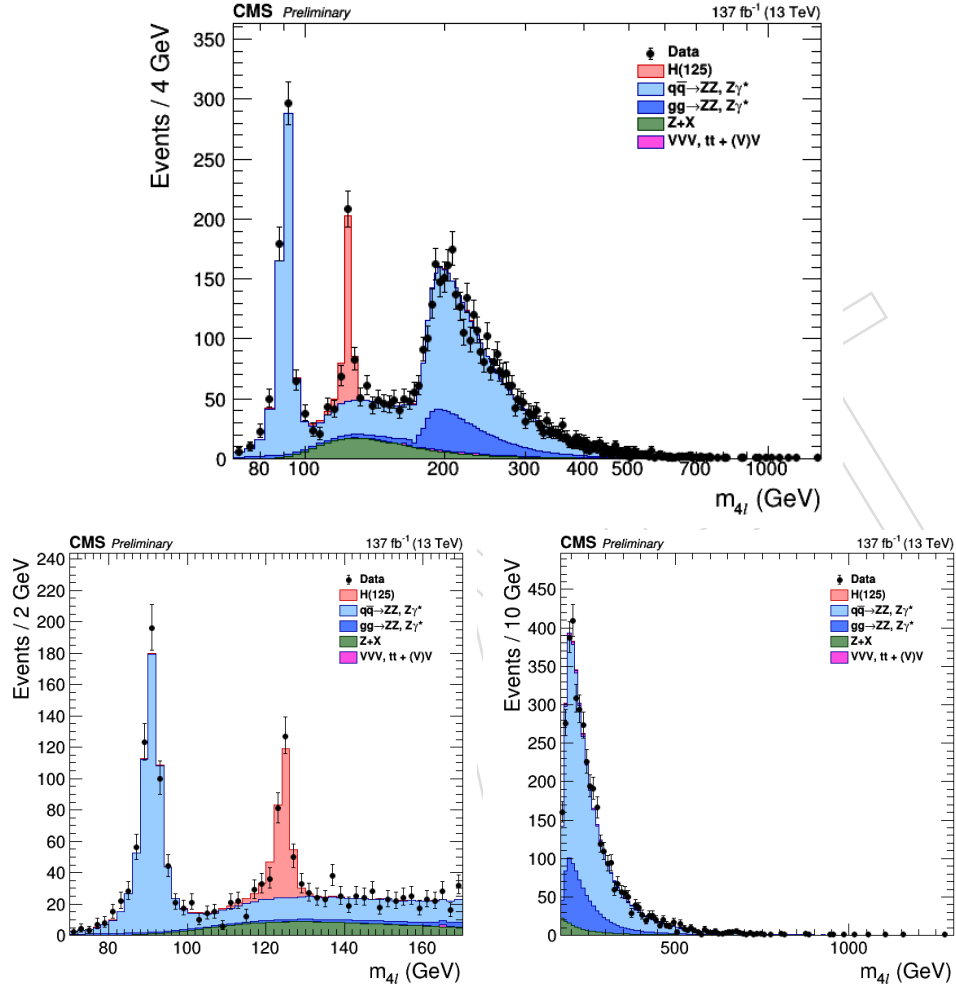


Figure 14: Distribution of the four-lepton reconstructed invariant mass $m_{4\ell}$ in the full mass range (top) and the low-mass range (bottom left) and high-mass range (bottom right). Points with error bars represent the data and stacked histograms represent expected distributions. The 125 GeV Higgs boson signal and the ZZ backgrounds are normalized to the SM expectation, the Z+X background to the estimation from data.

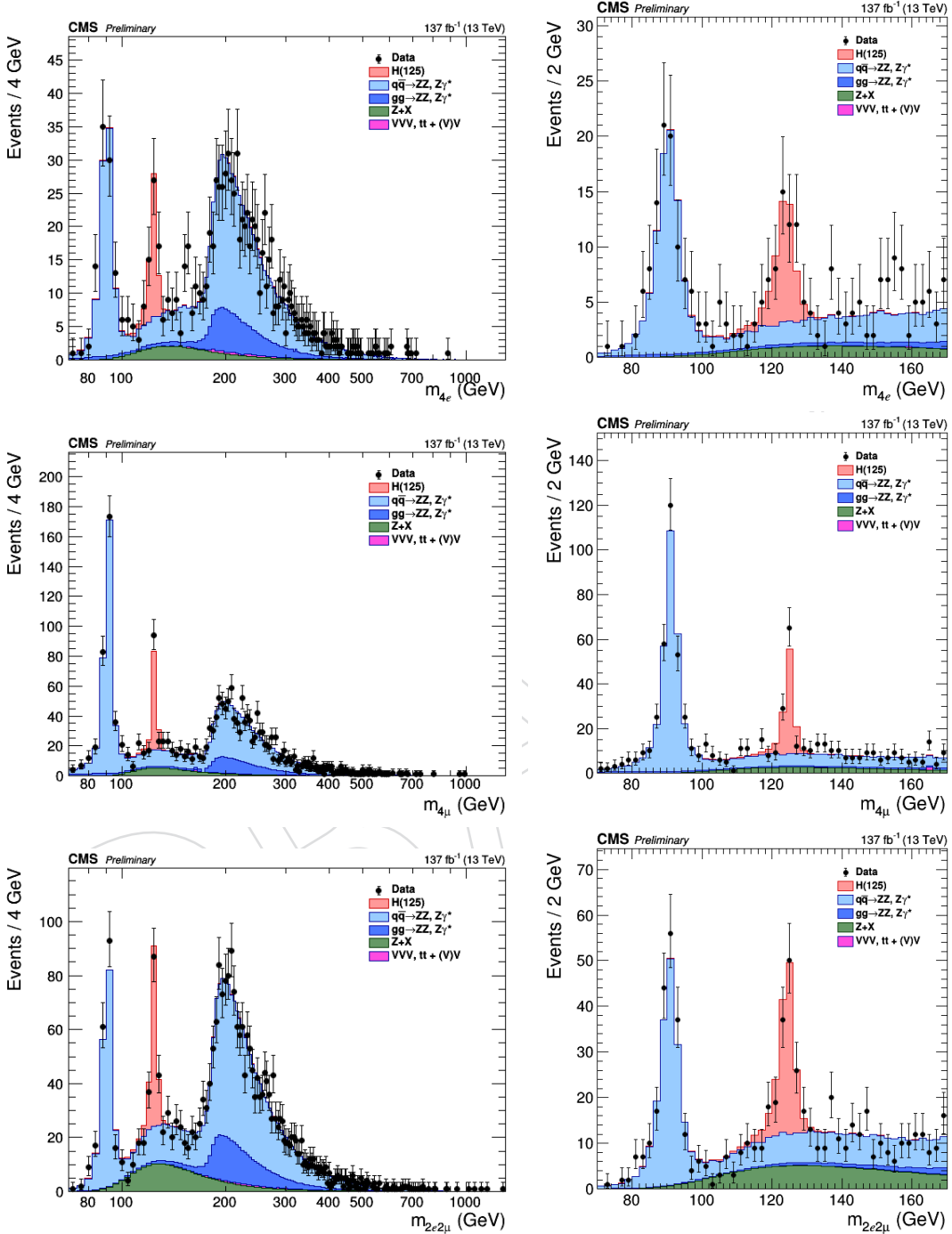
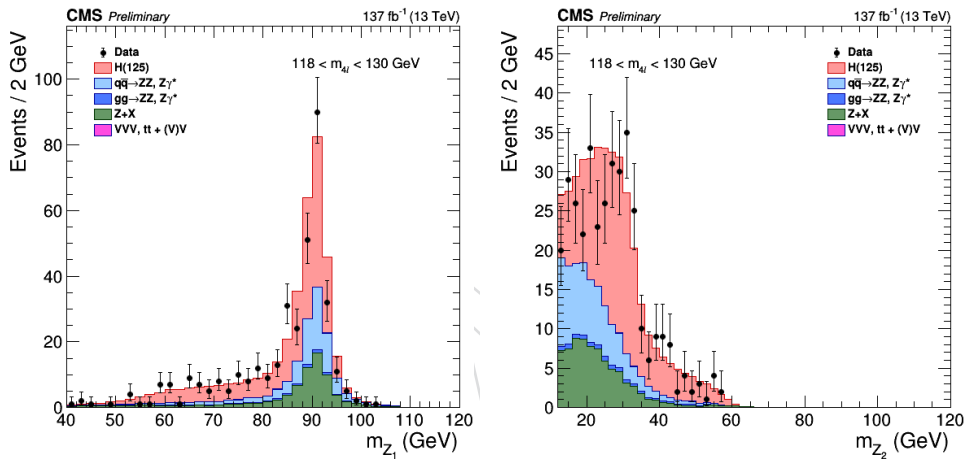


Figure 15: Distribution of the four-lepton reconstructed mass in several sub-channels: $4e$ (top), 4μ (middle), $2e2\mu$ for the low-mass range (bottom) for the full mass range (left) and the low-mass range (right).



Distribution of the Z_1 (left) and Z_2 (right) reconstructed invariant masses for the full mass range (left) and the low mass ($118 < m_{4\ell} < 130$ GeV) range (right). The stacked histograms and the gray scale represent expected distributions, and points represent the data. The 125 GeV Higgs boson signal and the ZZ backgrounds are normalized to the SM expectation, the Z+X background to the estimation from data.

536 8.2 Differential Cross Sections measurement results

537 **FIXME:** Results to be updated with final processing

538 8.2.1 Results for Higgs production observables

539 The expected differential cross section results can be seen in Fig. 16.

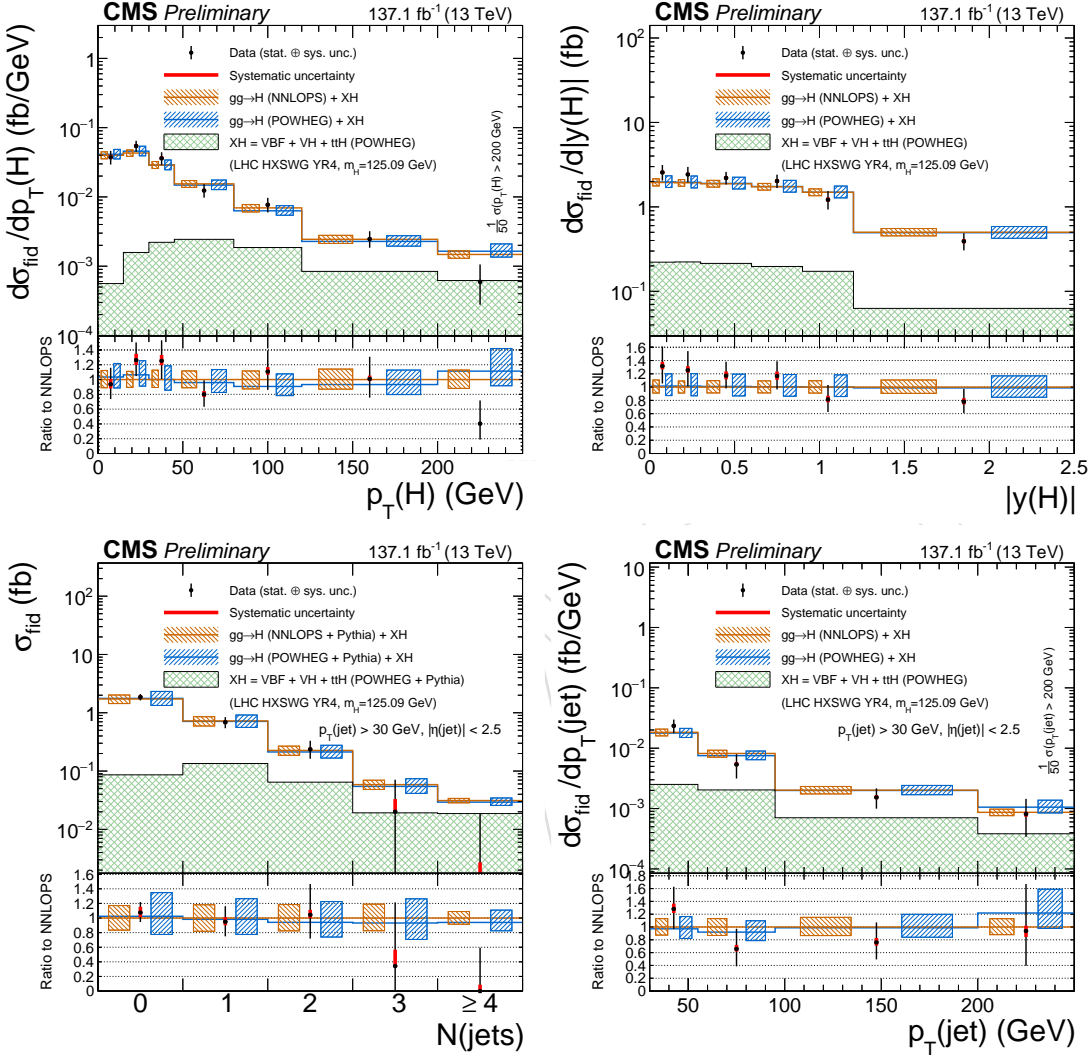


Figure 16: The results of the differential cross section measurement for $p_T(H)$ (middle left), $|y(H)|$ (middle right) and $N(jets)$ (bottom left), p_T of the leading jet (bottom right). The acceptance and theoretical uncertainties in the differential bins are calculated using POWHEG. The sub-dominant component of the signal (VBF + VH + tH) is denoted as XH.

540 8.2.2 Results for Higgs decay observables

541 Additional decay observables include Φ , Φ_1 , $m(Z_1)$, $m(Z_2)$, $|\cos \theta^*|$, $|\cos \theta_1|$ and $|\cos \theta_2|$ which
542 are studied in $H \rightarrow 4\ell$ using full Run 2 toy data and compared with the theoretical predictions.

543 In each plot shown below, systematic uncertainty is indicated by red bars and black bars show
544 total statistical and the systematic uncertainties, combined in quadrature. The blue and brown
545 colors show the theoretical predictions. The acceptances and the theoretical uncertainties in
546 differential bins are computed using POWHEG. Sub-dominant production contributions XH

⁵⁴⁷ = VBF + VH + ttH are shown in green separately. The systematic uncertainties correspond to
⁵⁴⁸ the generators accuracy are also taken in to account for differential predictions. The fraction of
⁵⁴⁹ 4 μ , 4e and 2e2 μ in each differential bin is allowed to float in fit.

DRAFT

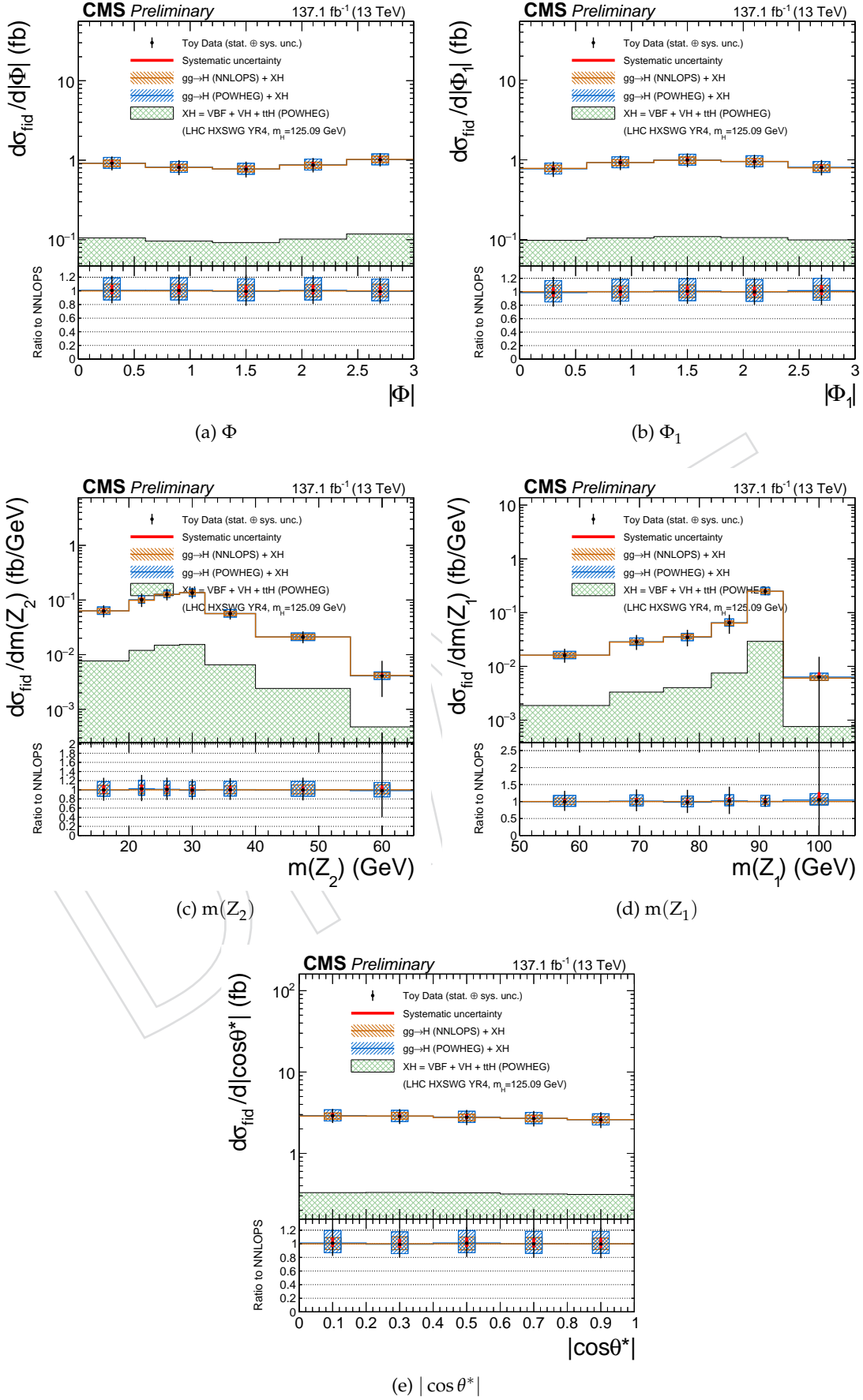


Figure 17: Differential fiducial cross section results using full Run 2 toy data for Φ , Φ_1 , $m(Z_1)$, $m(Z_2)$ and $|\cos\theta^*|$ in $H \rightarrow 4\ell$ and comparison with the theoretical predictions.

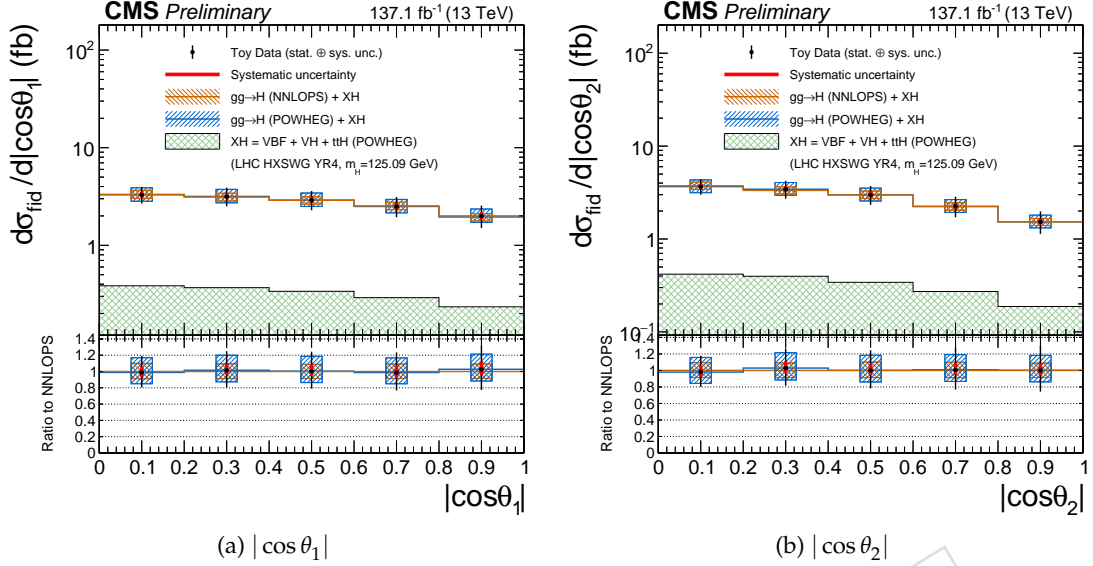


Figure 18: Differential fiducial cross section results using full Run 2 toy data for $|\cos \theta_1|$, $|\cos \theta_2|$ in $H \rightarrow 4\ell$ and comparison with the theoretical predictions. Systematic uncertainty is indicated by red bars and black bars show total statistical and the systematic uncertainties, combined in quadrature. The blue and brown colors show the theoretical predictions. The acceptances and the theoretical uncertainties in differential bins are computed using POWHEG. Sub-dominant production contributions $XH = VBF + VH + t\bar{t}H$ are shown in green separately. The systematic uncertainties correspond to the generators accuracy are also taken in to account for differential predictions. The fraction of 4μ , $4e$ and $2e2\mu$ in each differential bin is allowed to float in fit.

550 8.3 Double differential cross section measurements

551 Differential measurements are extended upto higher dimension upto 2. Several 2D combina-
552 tion are aimed to be measured e.g. $m(Z_1)$ vs $m(Z_2)$ and so forth. To be updated further.

553 8.4 Interpretations

554 To be updated.

555 8.4.1 Constraints on Yukawa Couplings: Fits of coupling modifiers (κ_b vs. κ_c)

556 To be updated.

557 8.4.2 Constraint on Higgs boson trilinear self-coupling (κ_λ)

558 To be updated.

DRAFT

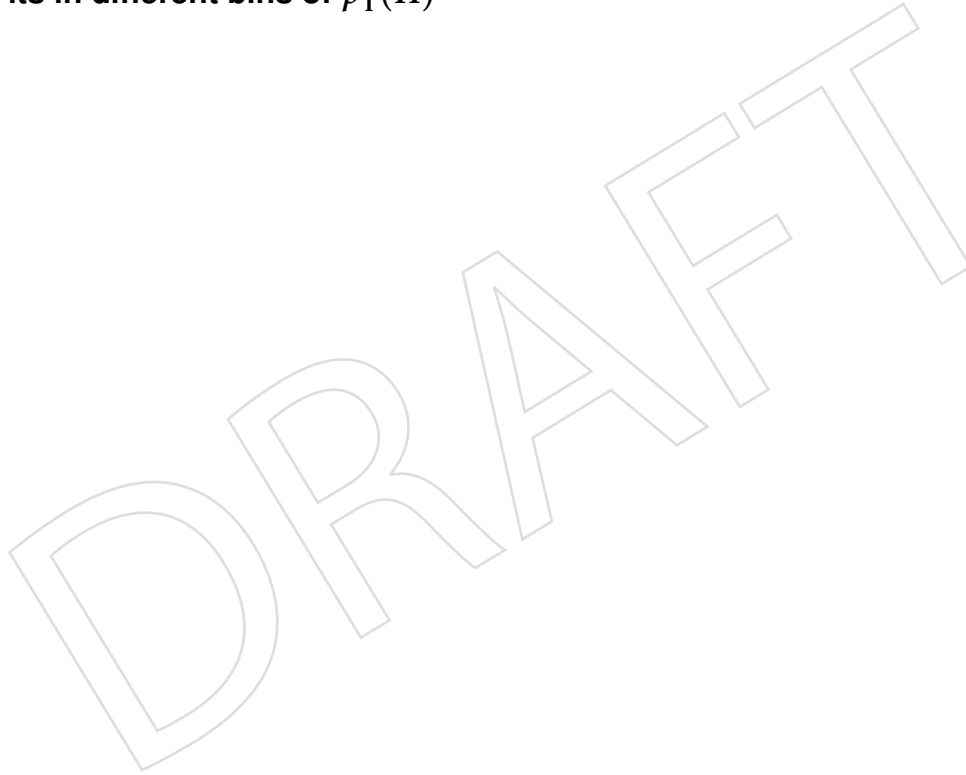
559 **9 Interpretation**

DRAFT

560 A Signal Shapes and Efficiencies

561 For all plots showing fits to the signal distributions, the red histograms show the distribution of
562 events which pass both the fiducial selection at generator level and pass the full reconstruction
563 level selection, including the selection on $p_T(H)$. The red curve shows a fit to this distribution
564 using a double-sided crystal ball function, and the resulting σ of the fit is also shown on the
565 plot. The blue histograms show events which pass the full reconstruction level selection, and
566 pass the fiducial selection at generator level within a different $p_T(H)$ bin. The blue curves show
567 a fit to this distribution using the same function as the red curve with a different normalization.
568 The black histograms show the distribution of events which pass the full reconstruction level
569 selection but do not pass the fiducial selection at generator level, and the black curve shows a fit
570 to this distribution using the same function as the red curve but with a different normalization.
571 The yellow histogram shows events which pass the full reconstruction level selection but where
572 one of the four selected leptons does not originate from the Higgs boson. The yellow curve
573 shows a fit to this distribution using a Landau function.

574 **A.1 Fits in different bins of $p_T(H)$**



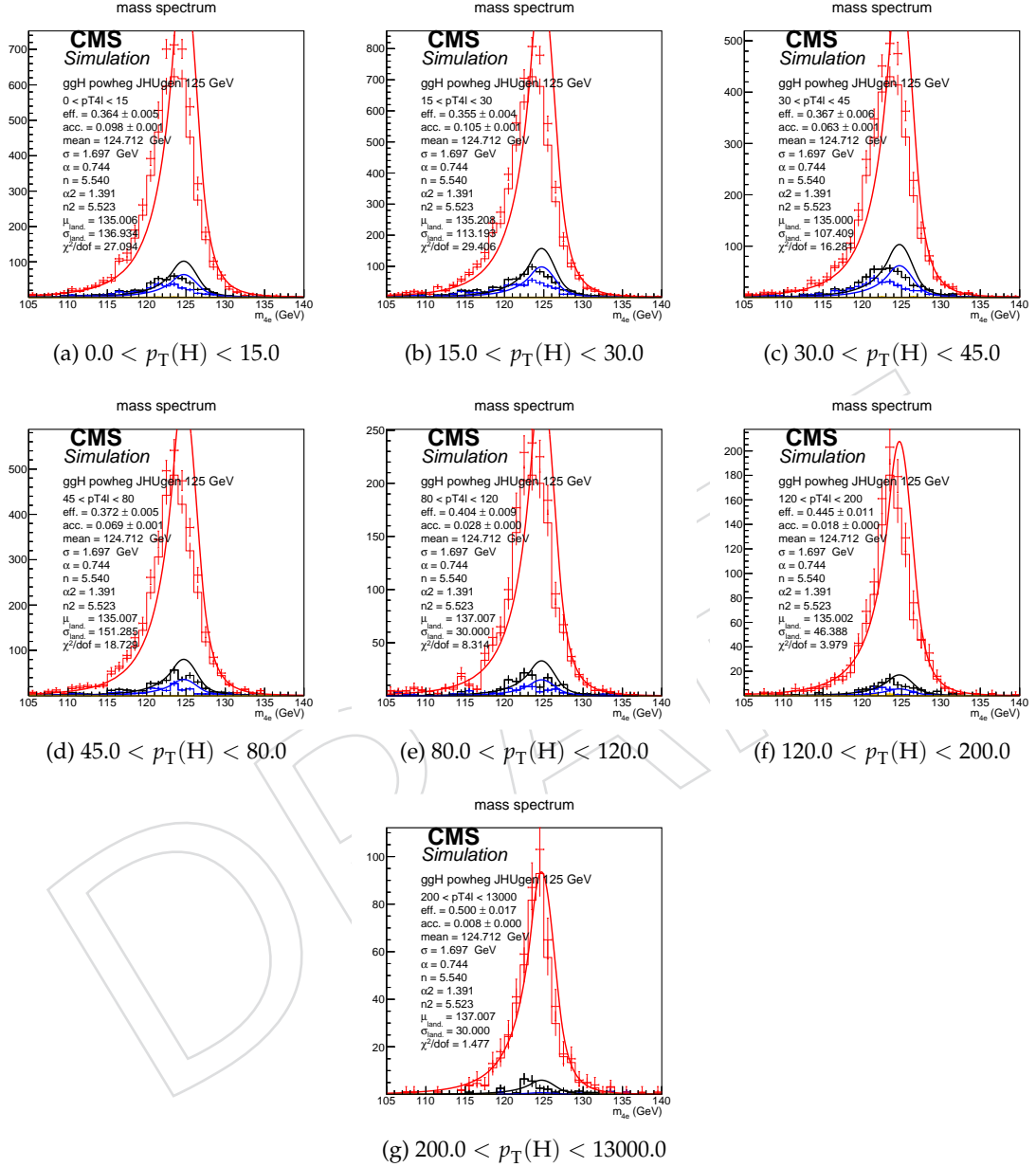


Figure 19: Example signal shapes at reconstruction level for a resonance of $m(4\ell)$ in $4e$ final state for the $gg \rightarrow H$ production mode from POWHEG+JHUGEN in different bins of $p_T(H)$. The black curve represents events which do not pass the fiducial volume selection. The curve has no effect on the result.

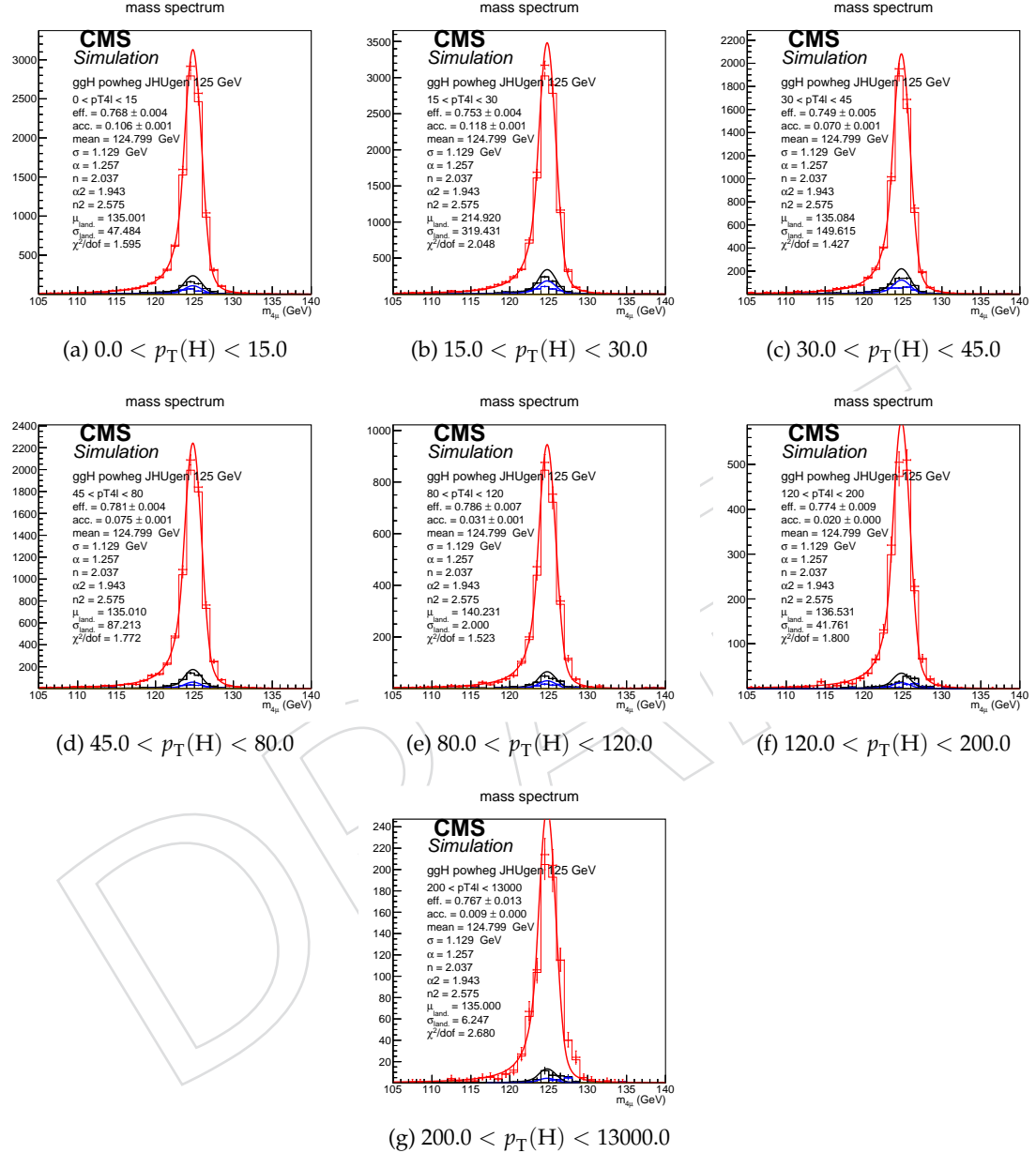


Figure 20: Example signal shapes at reconstruction level for a resonance of $m(4\ell)$ in 4μ final state for the $gg \rightarrow H$ production mode from POWHEG+JHUGEN in different bins of $p_T(H)$. The black curve represents events which do not pass the fiducial volume selection. The curve has no effect on the result.

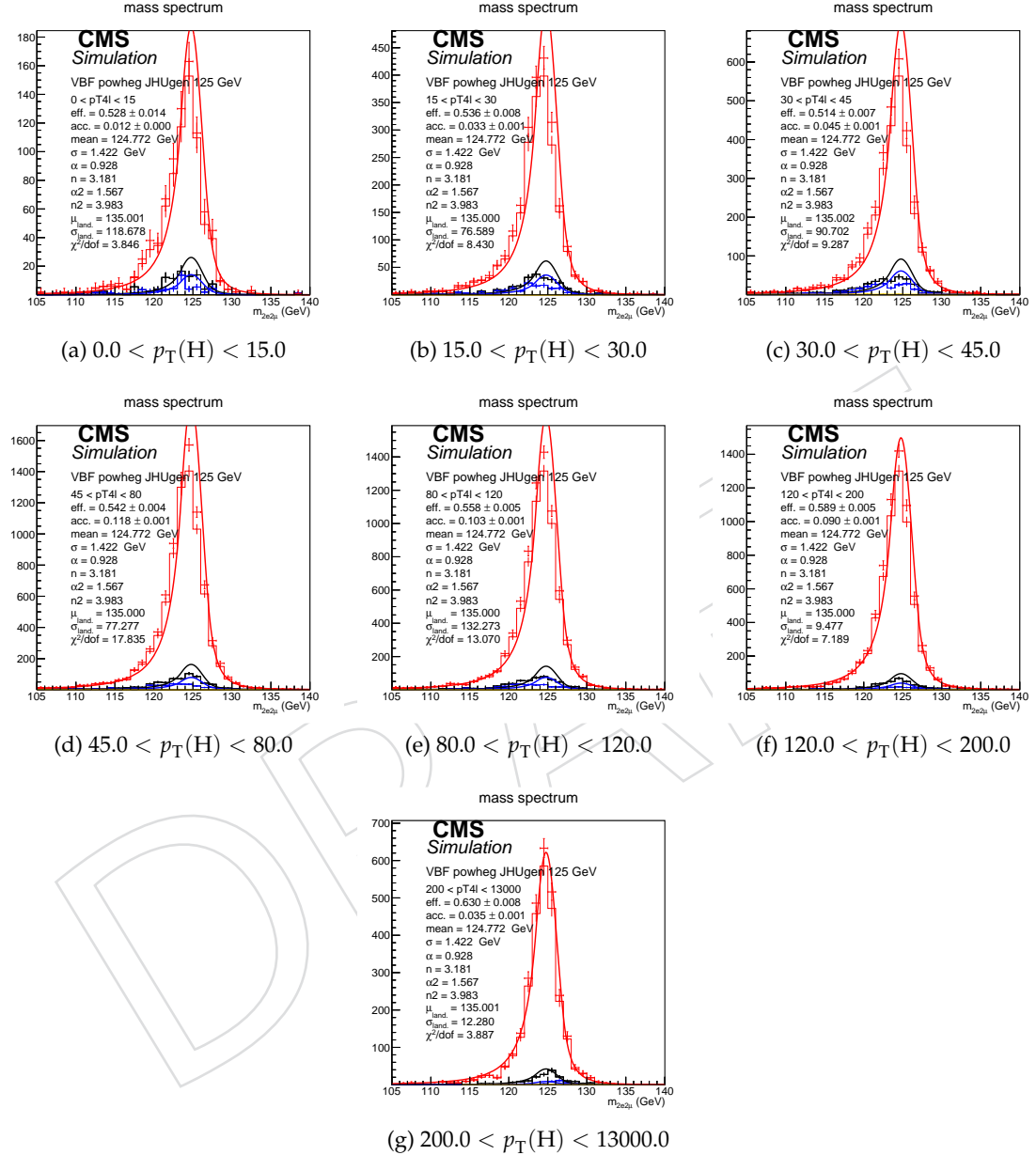


Figure 21: Example signal shapes at reconstruction level for a resonance of $m(4\ell)$ in $2e2\mu$ final state for the VBF production mode from POWHEG+JHUGEN in different bins of $p_T(H)$. The black curve represents events which do not pass the fiducial volume selection. The curve has no effect on the result.

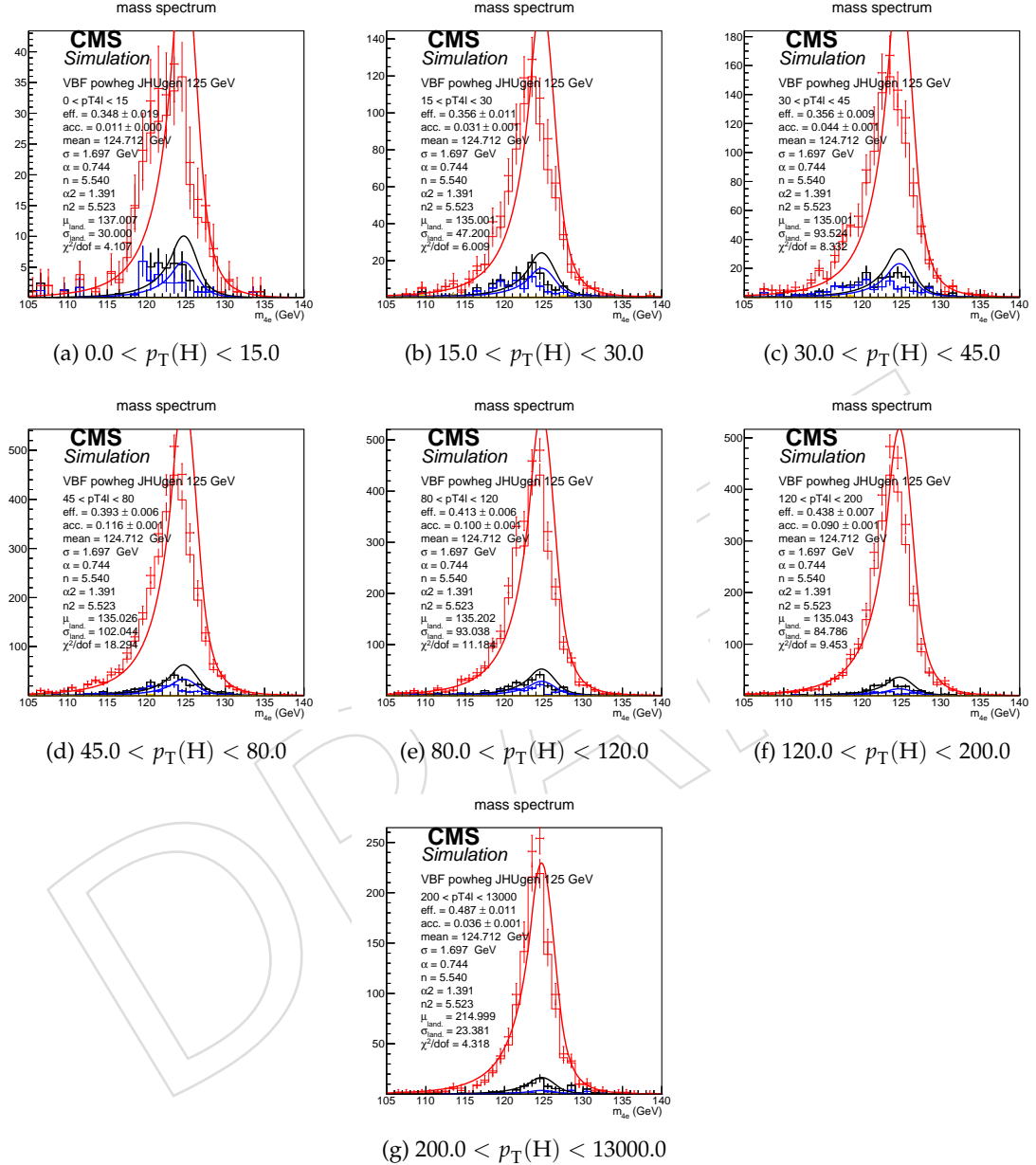


Figure 22: Example signal shapes at reconstruction level for a resonance of $m(4\ell)$ in $4e$ final state for the VBF production mode from POWHEG+JHUGEN in different bins of $p_T(H)$. The black curve represents events which do not pass the fiducial volume selection. The curve has no effect on the result.

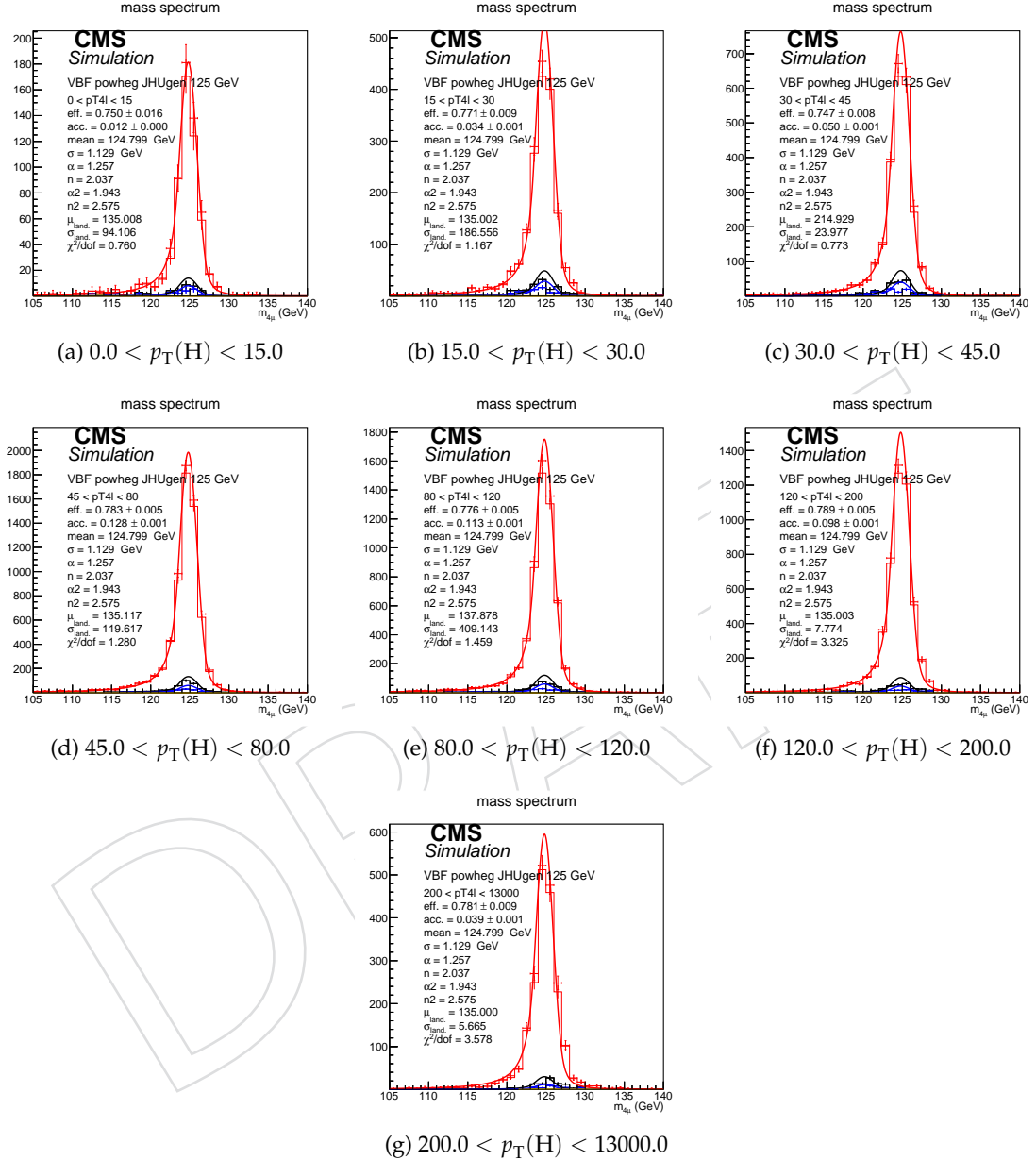


Figure 23: Example signal shapes at reconstruction level for a resonance of $m(4\ell)$ in 4μ final state for the VBF production mode from POWHEG+JHUGEN in different bins of $p_T(H)$. The black curve represents events which do not pass the fiducial volume selection. The curve has no effect on the result.

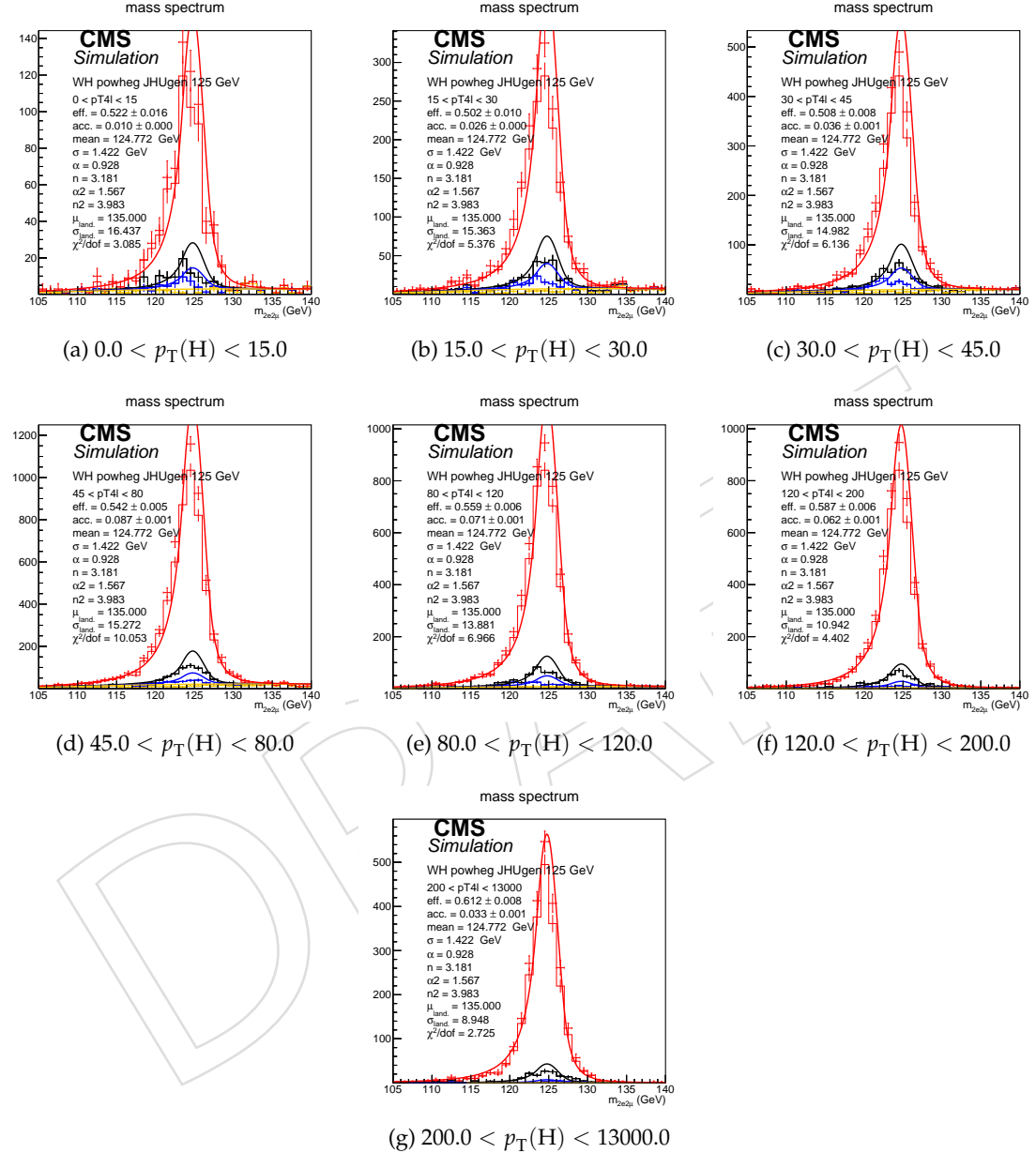


Figure 24: Example signal shapes at reconstruction level for a resonance of $m(4\ell)$ in $2e2\mu$ final state for the WH production mode from POWHEG+JHUGEN in different bins of $p_T(H)$. The black curve represents events which do not pass the fiducial volume selection. The curve has no effect on the result.

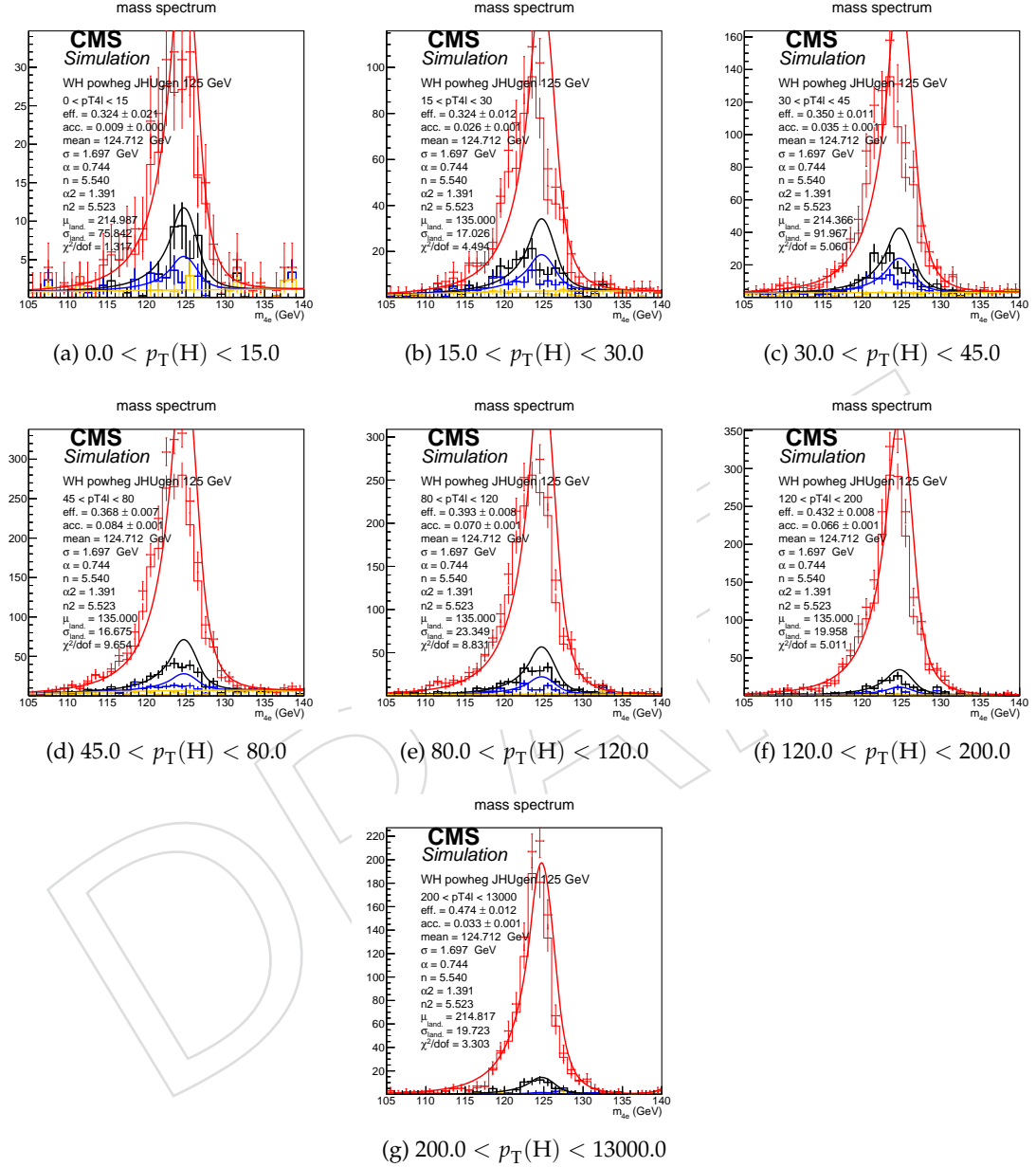


Figure 25: Example signal shapes at reconstruction level for a resonance of $m(4\ell)$ in $4e$ final state for the WH production mode from POWHEG+JHUGEN in different bins of $p_T(H)$. The black curve represents events which do not pass the fiducial volume selection. The curve has no effect on the result.

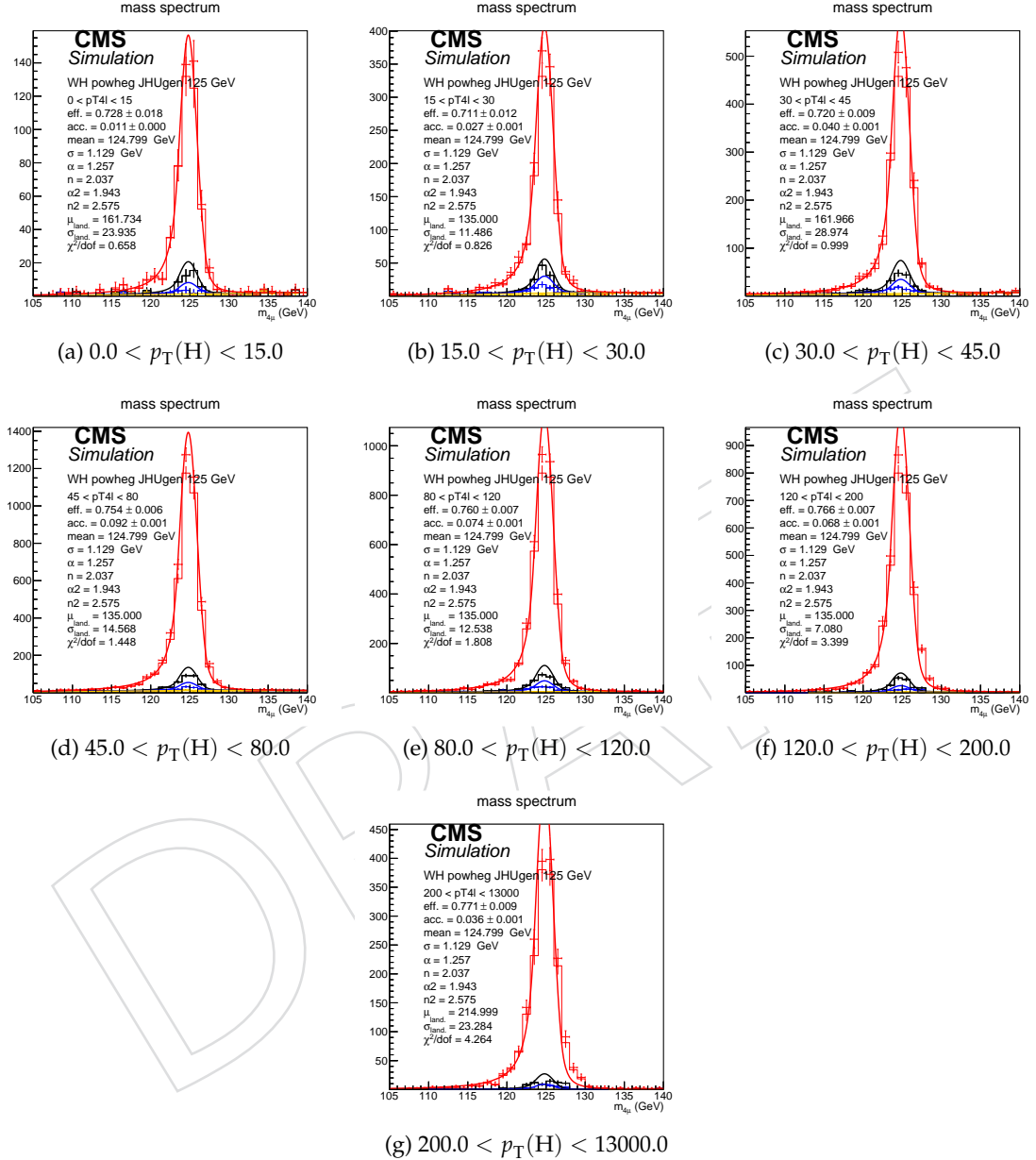


Figure 26: Example signal shapes at reconstruction level for a resonance of $m(4\ell)$ in 4μ final state for the $gg \rightarrow H$ production mode from POWHEG+JHUGEN in different bins of $p_T(H)$. The black curve represents events which do not pass the fiducial volume selection. The curve has no effect on the result.

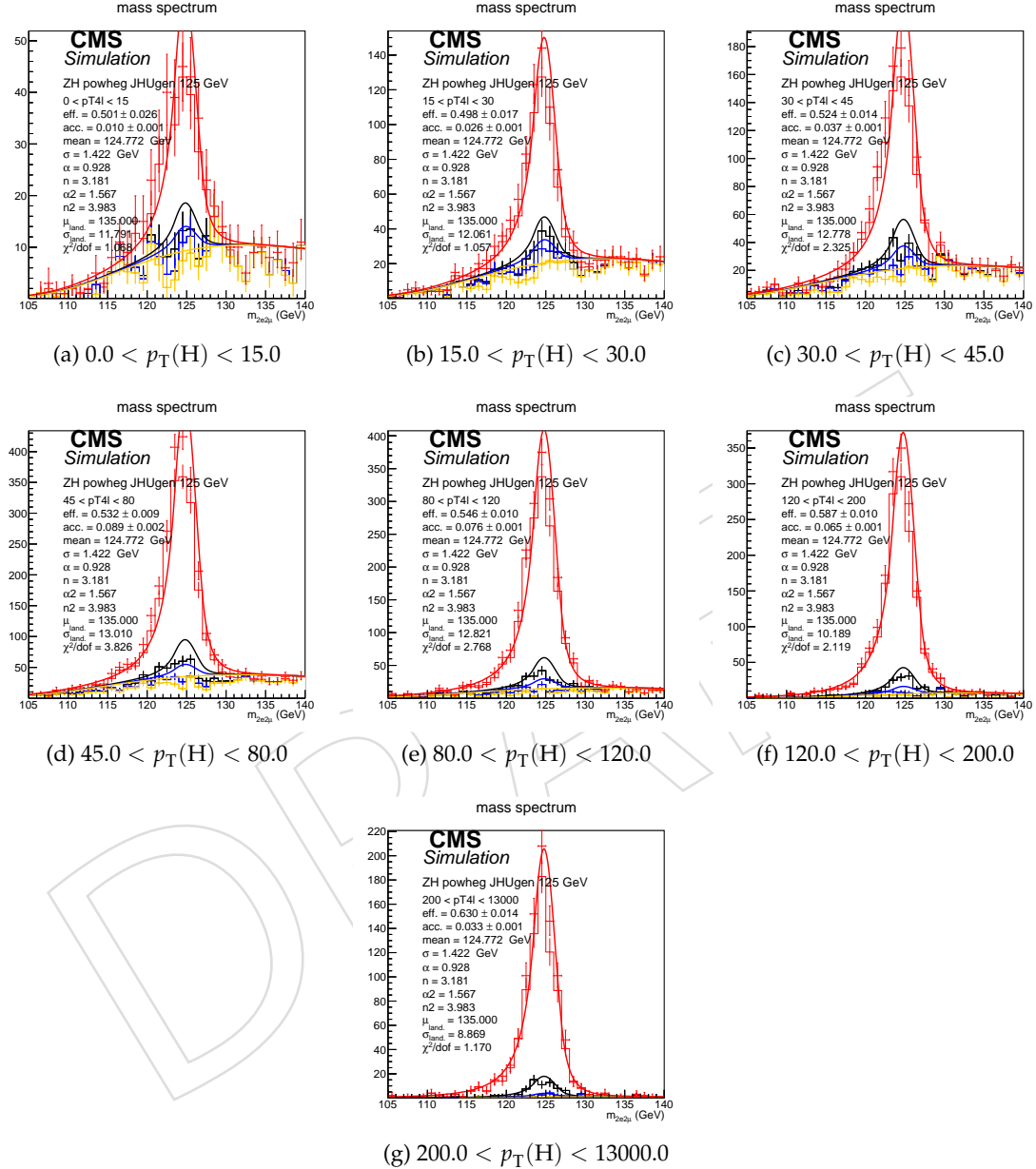


Figure 27: Example signal shapes at reconstruction level for a resonance of $m(4\ell)$ in $2e2\mu$ final state for the ZH production mode from POWHEG+JHUGEN in different bins of $p_T(H)$. The black curve represents events which do not pass the fiducial volume selection. The curve has no effect on the result.

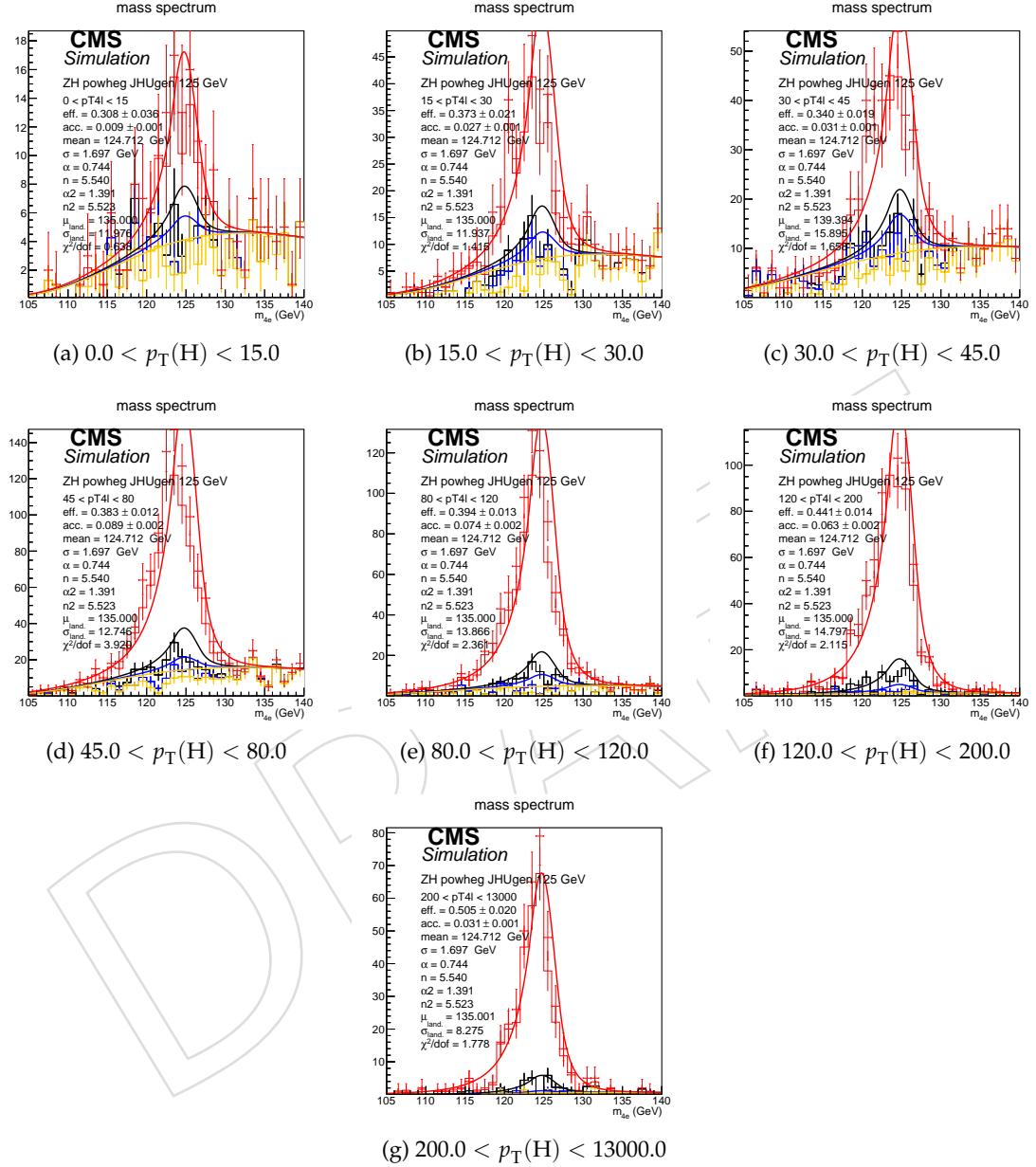


Figure 28: Example signal shapes at reconstruction level for a resonance of $m(4\ell)$ in $4e$ final state for the ZH production mode from POWHEG+JHUGEN in different bins of $p_{\text{T}}(\text{H})$. The black curve represents events which do not pass the fiducial volume selection. The curve has no effect on the result.

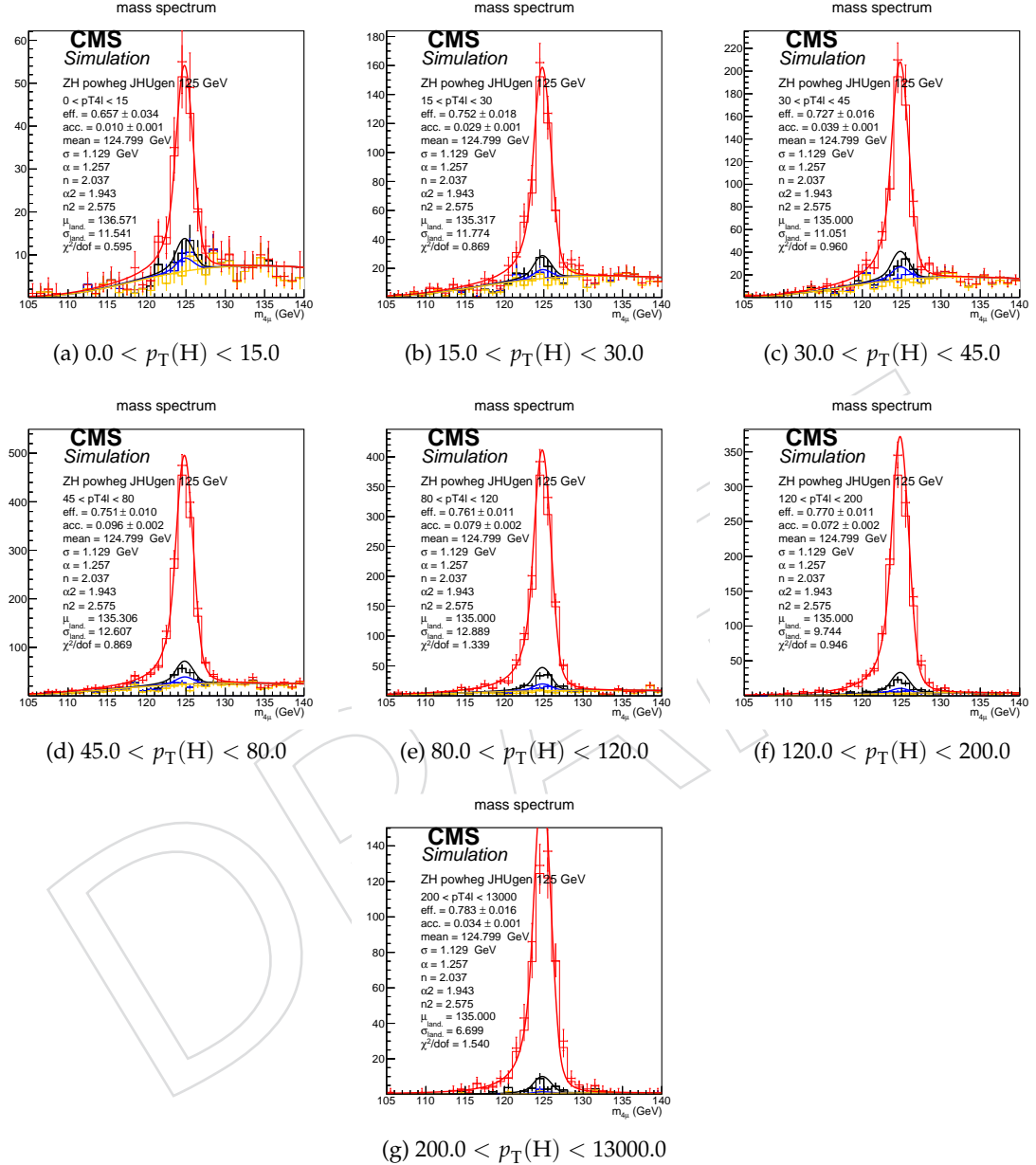


Figure 29: Example signal shapes at reconstruction level for a resonance of $m(4\ell)$ in 4μ final state for the ZH production mode from POWHEG+JHUGEN in different bins of $p_T(H)$. The black curve represents events which do not pass the fiducial volume selection. The curve has no effect on the result.

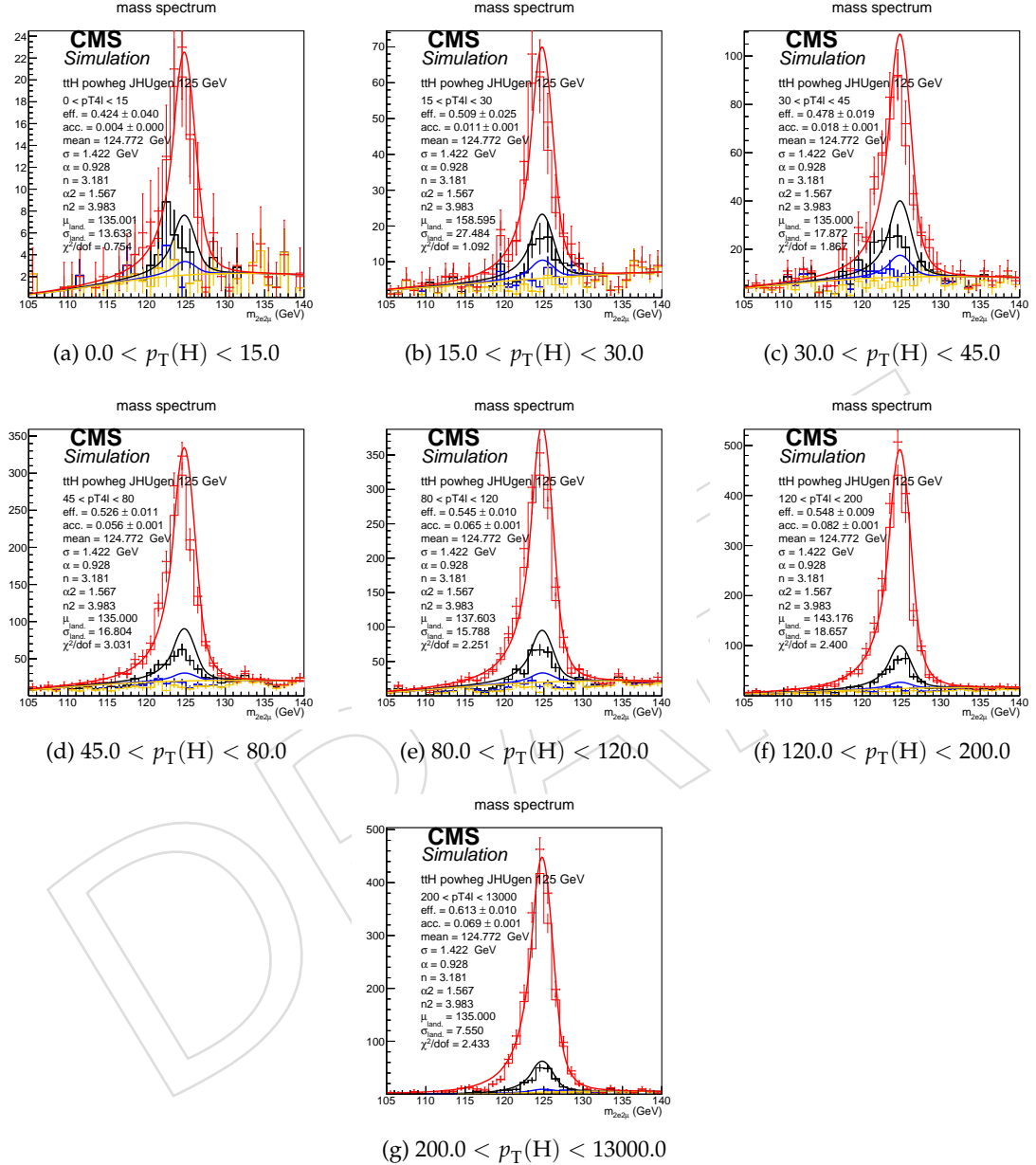


Figure 30: Example signal shapes at reconstruction level for a resonance of $m(4\ell)$ in $2e2\mu$ final state for the $t\bar{t}H$ production mode from POWHEG+JHUGEN in different bins of $p_T(H)$. The black curve represents events which do not pass the fiducial volume selection. The curve has no effect on the result.

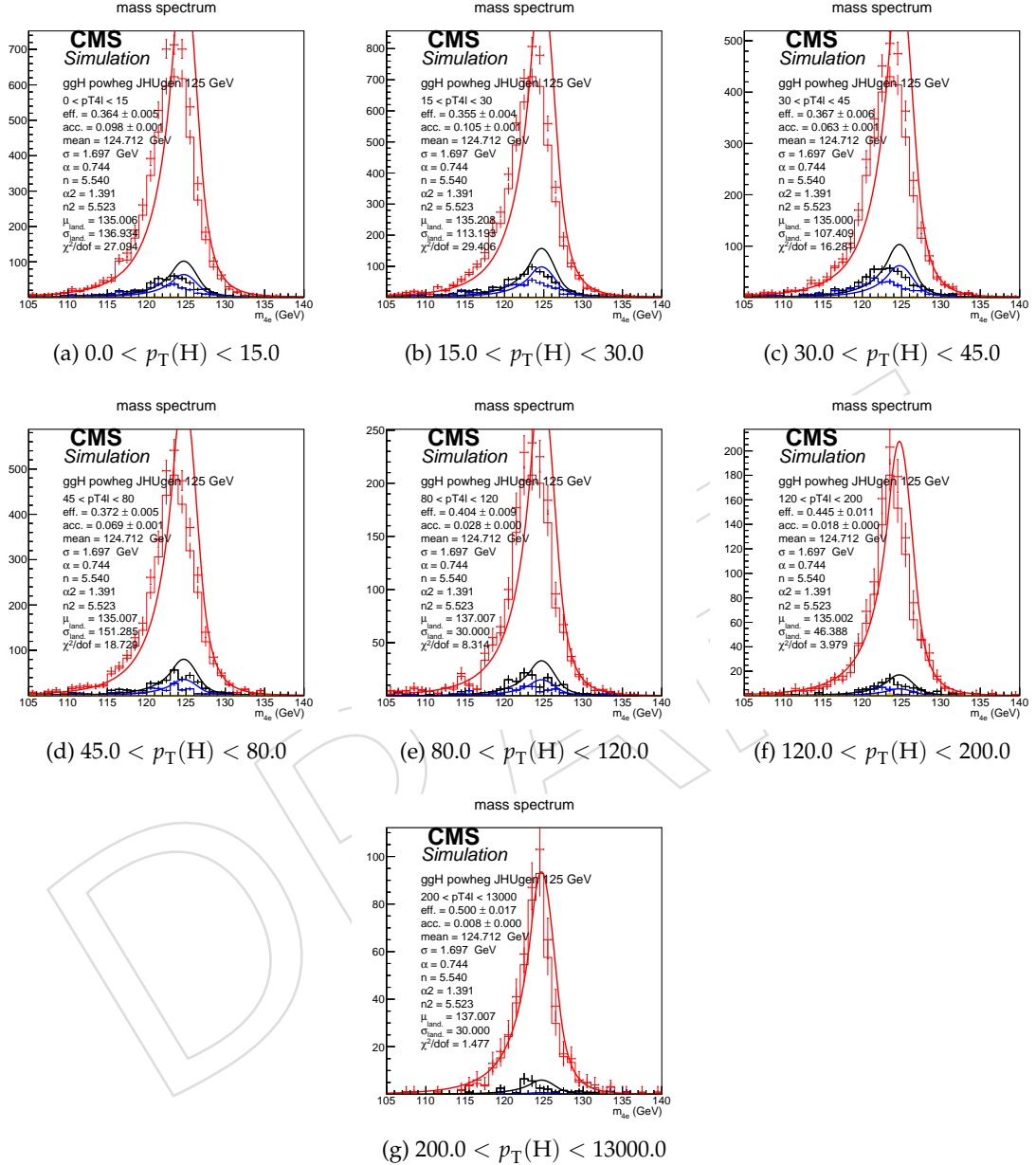


Figure 31: Example signal shapes at reconstruction level for a resonance of $m(4\ell)$ in $4e$ final state for the $t\bar{t}H$ production mode from POWHEG+JHUGEN in different bins of $p_T(H)$. The black curve represents events which do not pass the fiducial volume selection. The curve has no effect on the result.

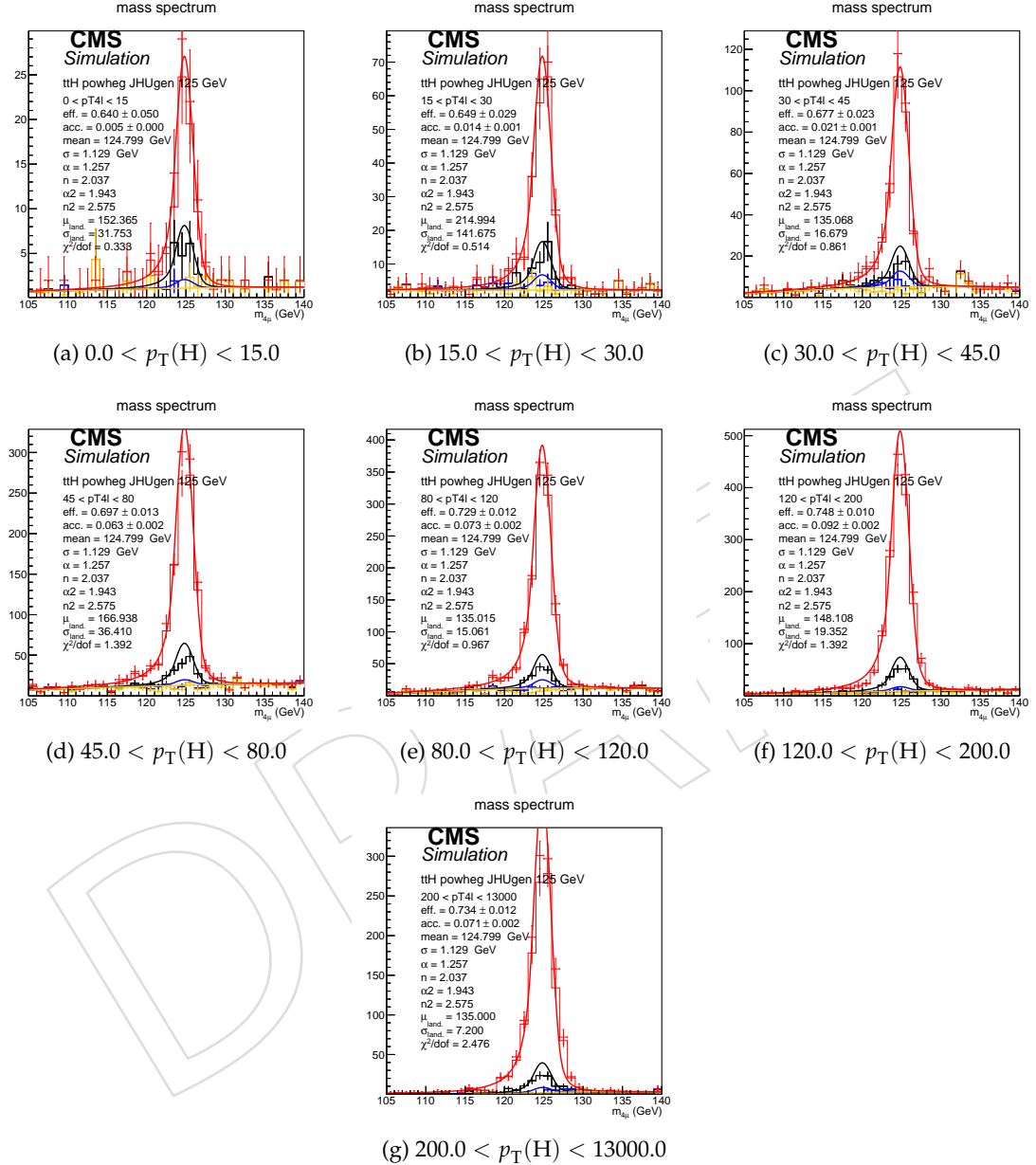


Figure 32: Example signal shapes at reconstruction level for a resonance of $m(4\ell)$ in 4μ final state for the $t\bar{t}H$ production mode from POWHEG+JHUGEN in different bins of $p_T(H)$. The black curve represents events which do not pass the fiducial volume selection. The curve has no effect on the result.

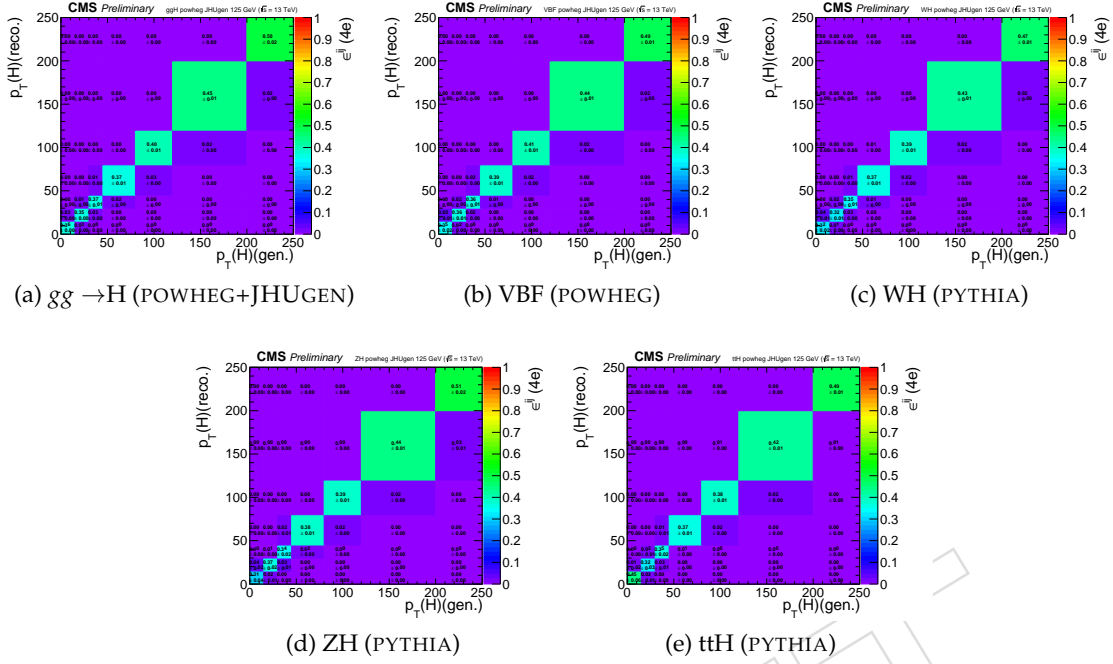


Figure 33: Efficiency matrices for $p_T(H)$ for different SM production modes in the $4e$ final state.

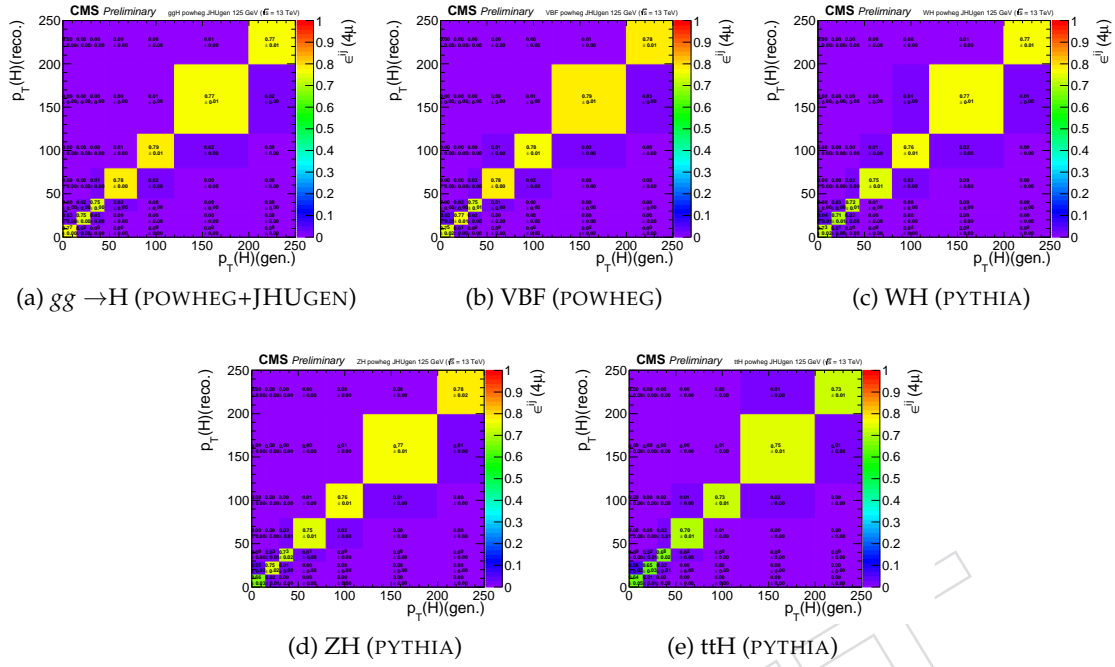


Figure 34: Efficiency matrices for $p_T(H)$ for different SM production modes in the 4μ final state.

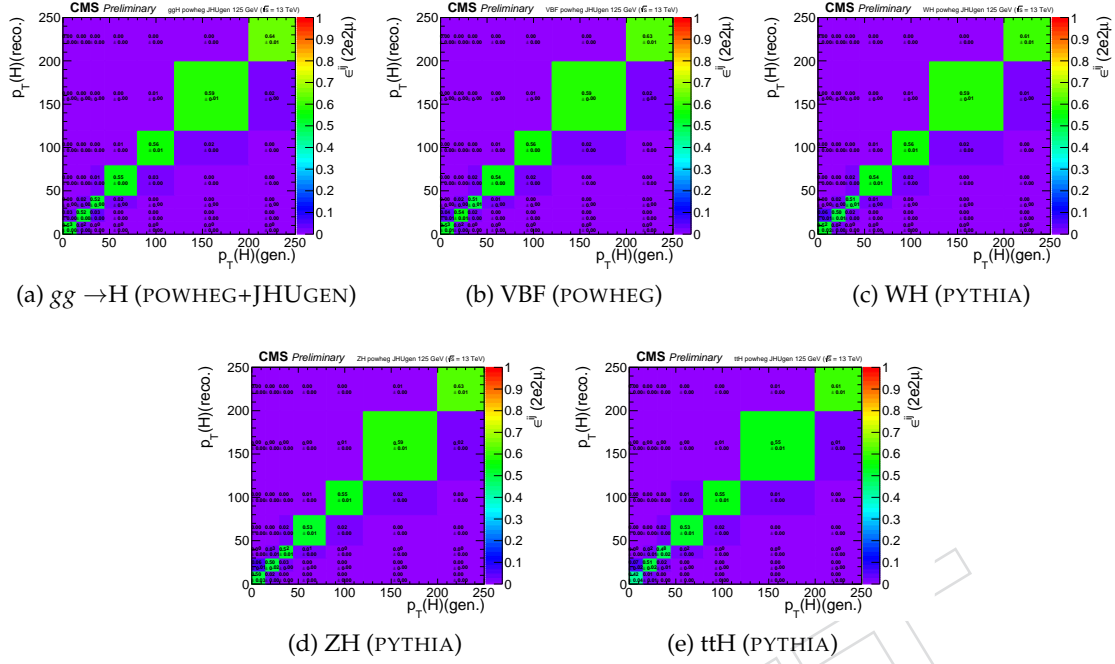
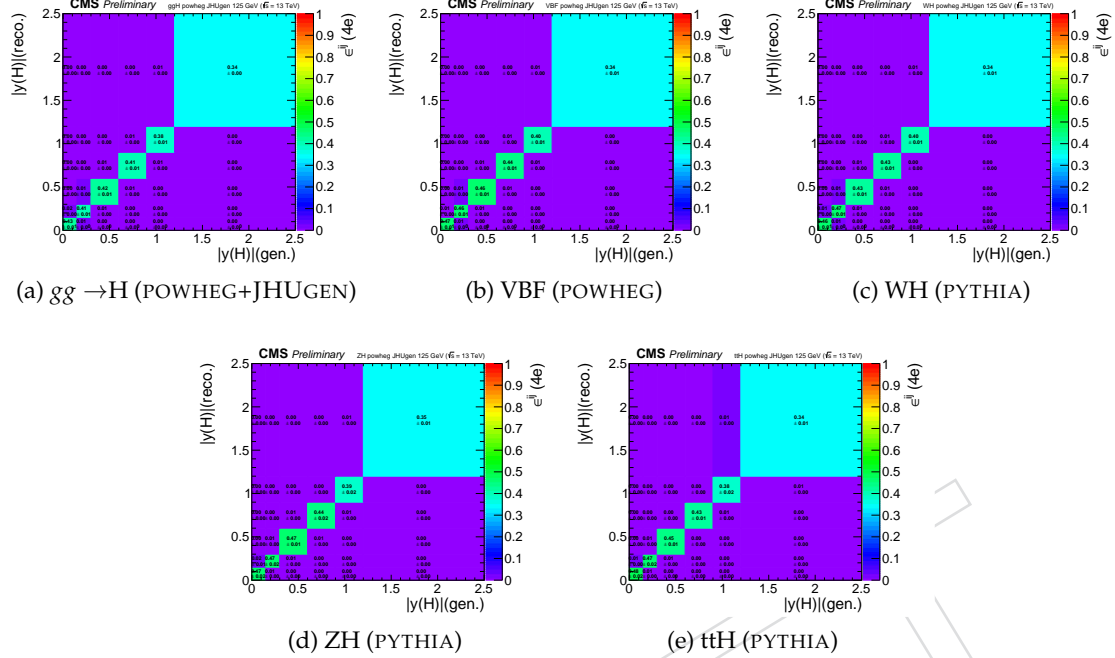


Figure 35: Efficiency matrices for $p_T(H)$ for different SM production modes in the $2e2\mu$ final state.

575 A.2 Signal inputs in different bins of $|y(H)|$ Figure 36: Efficiency matrices for $|y(H)|$ for different SM production modes in the $4e$ final state.

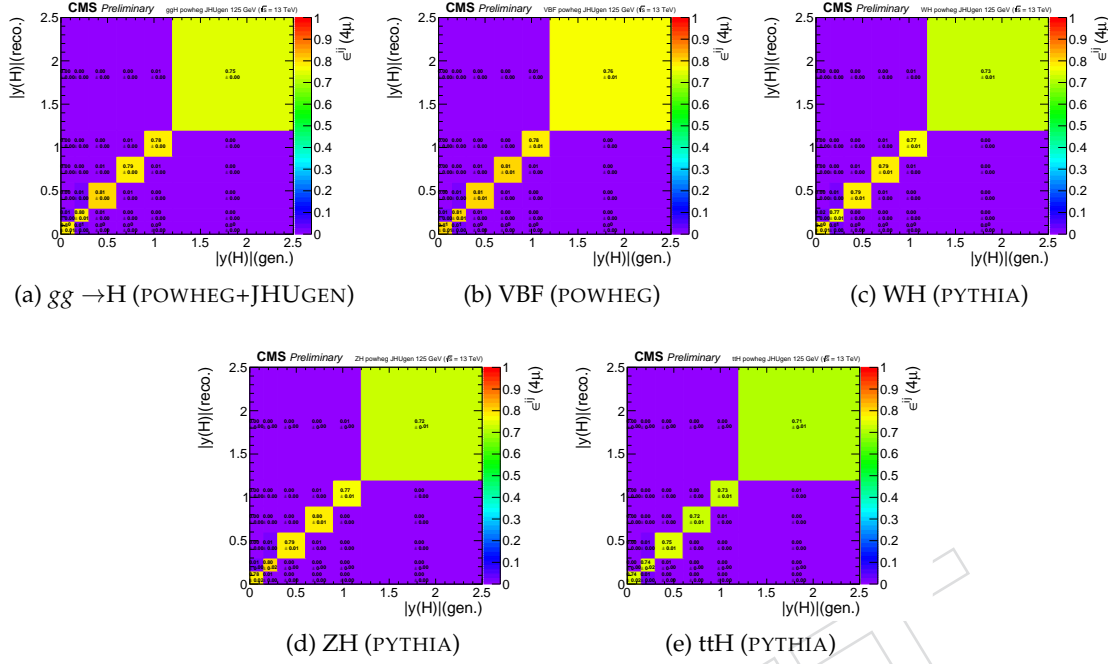


Figure 37: Efficiency matrices for $|y(H)|$ for different SM production modes in the 4μ final state.

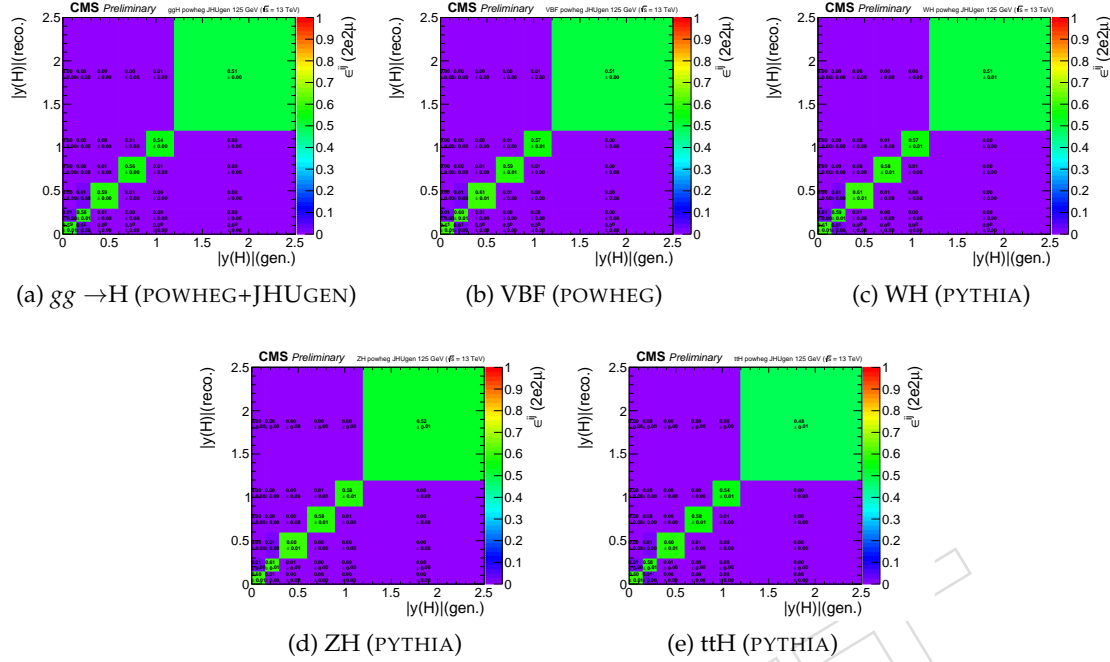


Figure 38: Efficiency matrices for $|y(H)|$ for different SM production modes in the $2e2\mu$ final state.

576 **A.3 Fits in different bins of N(jets)**

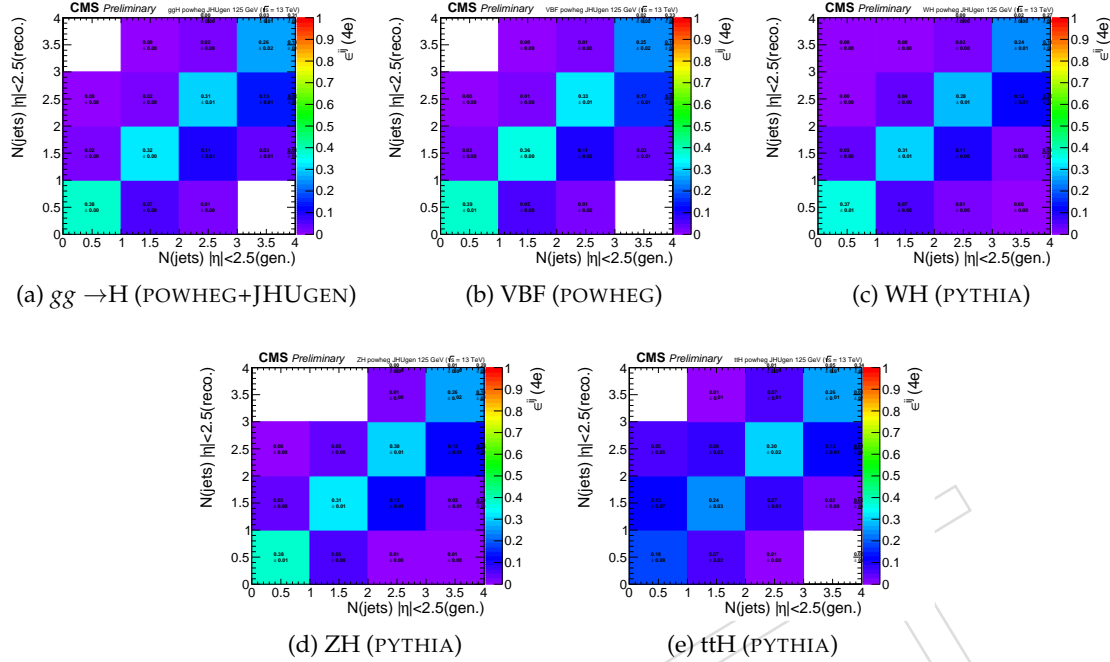


Figure 39: Efficiency matrices for $N(jets)$ for different SM production modes in the $4e$ final state.

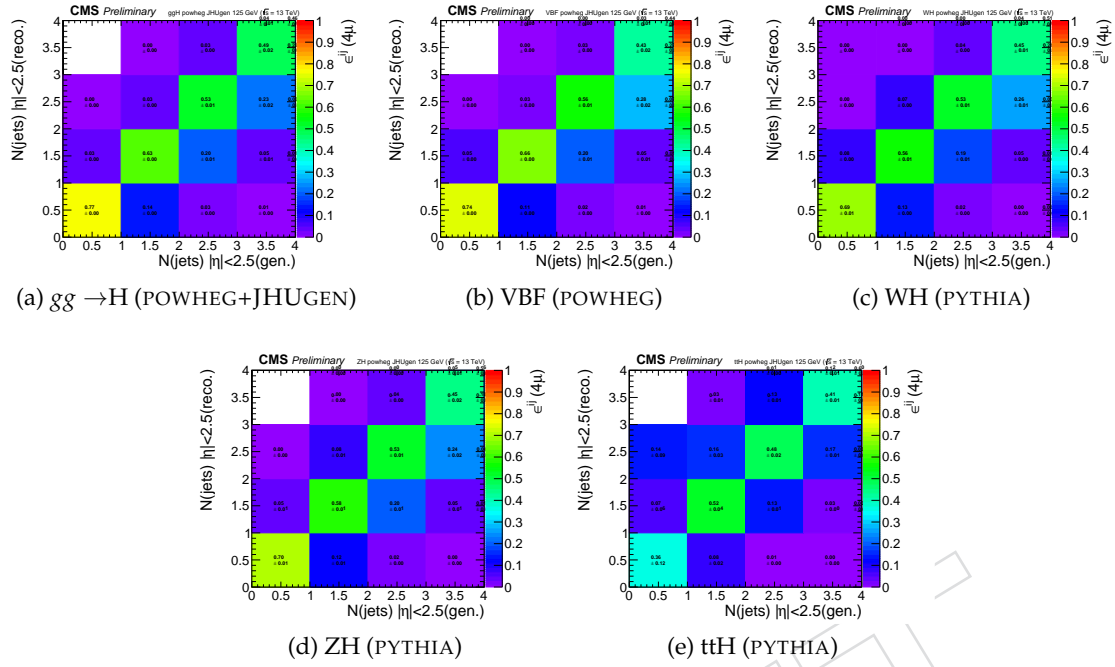


Figure 40: Efficiency matrices for $N(\text{jets})$ for different SM production modes in the 4μ final state.

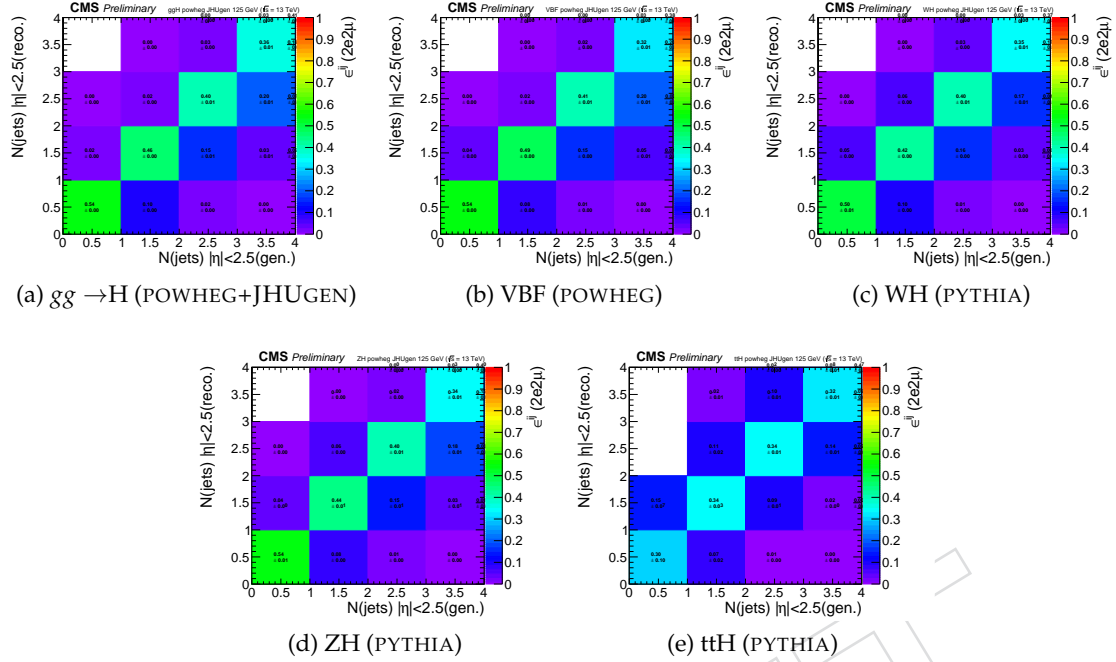


Figure 41: Efficiency matrices for $N(\text{jets})$ for different SM production modes in the $2e2\mu$ final state.

577 References

- 578 [1] CMS Collaboration, "Observation of a new boson at a mass of 125 GeV with the CMS
579 experiment at the LHC", *Phys. Lett. B* **716** (2012) 30,
580 doi:10.1016/j.physletb.2012.08.021, arXiv:1207.7235.
- 581 [2] ATLAS Collaboration, "Observation of a new particle in the search for the Standard
582 Model Higgs boson with the ATLAS detector at the LHC", *Phys. Lett. B* **716** (2012) 1,
583 doi:10.1016/j.physletb.2012.08.020, arXiv:1207.7214.
- 584 [3] F. Englert and R. Brout, "Broken Symmetry and the Mass of Gauge Vector Mesons",
585 *Phys. Rev. Lett.* **13** (1964) 321, doi:10.1103/PhysRevLett.13.321.
- 586 [4] P. W. Higgs, "Broken symmetries, massless particles and gauge fields", *Phys. Lett.* **12**
587 (1964) 132, doi:10.1016/0031-9163(64)91136-9.
- 588 [5] P. W. Higgs, "Broken Symmetries and the Masses of Gauge Bosons", *Phys. Rev. Lett.* **13**
589 (1964) 508, doi:10.1103/PhysRevLett.13.508.
- 590 [6] G. Guralnik, C. Hagen, and T. Kibble, "Global Conservation Laws and Massless
591 Particles", *Phys. Rev. Lett.* **13** (1964) 585, doi:10.1103/PhysRevLett.13.585.
- 592 [7] P. W. Higgs, "Spontaneous Symmetry Breakdown without Massless Bosons", *Phys. Rev.* **145**
593 (1966) 1156, doi:10.1103/PhysRev.145.1156.
- 594 [8] T. Kibble, "Symmetry breaking in nonAbelian gauge theories", *Phys. Rev.* **155** (1967)
595 1554, doi:10.1103/PhysRev.155.1554.
- 596 [9] CMS Collaboration, "Precise determination of the mass of the Higgs boson and tests of
597 compatibility of its couplings with the standard model predictions using proton
598 collisions at 7 and 8 TeV", *Eur. Phys. J. C* **75** (2015) 212,
599 doi:10.1140/epjc/s10052-015-3351-7, arXiv:1412.8662.
- 600 [10] ATLAS Collaboration, "Measurements of the Higgs boson production and decay rates
601 and coupling strengths using pp collision data at $\sqrt{s} = 7$ and 8 TeV in the ATLAS
602 experiment", *Eur. Phys. J. C* **76** (2016) doi:10.1140/epjc/s10052-015-3769-y,
603 arXiv:1507.04548.
- 604 [11] ATLAS, CMS Collaboration, "Combined Measurement of the Higgs Boson Mass in pp
605 Collisions at $\sqrt{s} = 7$ and 8 TeV with the ATLAS and CMS Experiments", *Phys. Rev. Lett.*
606 **114** (2015) 191803, doi:10.1103/PhysRevLett.114.191803, arXiv:1503.07589.
- 607 [12] "Measurements of the Higgs boson production and decay rates and constraints on its
608 couplings from a combined ATLAS and CMS analysis of the LHC pp collision data at \sqrt{s}
609 = 7 and 8 TeV", Technical Report CMS-PAS-HIG-15-002. ATLAS-CONF-2015-044, CERN,
610 Geneva, 2015.
- 611 [13] CMS Collaboration, "Measurement of the properties of a Higgs boson in the four-lepton
612 final state", *Phys. Rev. D* **89** (2014) 092007, doi:10.1103/PhysRevD.89.092007,
613 arXiv:1312.5353.
- 614 [14] CMS Collaboration, "Study of the Mass and Spin-Parity of the Higgs Boson Candidate
615 via Its Decays to Z Boson Pairs", *Phys. Rev. Lett.* **110** (2013) 081803,
616 doi:10.1103/PhysRevLett.110.081803, arXiv:1212.6639.

- [617] [15] CMS Collaboration, “Constraints on the spin-parity and anomalous HVV couplings of
618 the Higgs boson in proton collisions at 7 and 8 TeV”, *Phys. Rev. D* **92** (2015) 012004,
619 doi:[10.1103/PhysRevD.92.012004](https://doi.org/10.1103/PhysRevD.92.012004), arXiv:[1411.3441](https://arxiv.org/abs/1411.3441).
- [620] [16] CMS Collaboration, “Constraints on the Higgs boson width from off-shell production
621 and decay to Z-boson pairs”, *Phys. Lett. B* **736** (2014) 64,
622 doi:[10.1016/j.physletb.2014.06.077](https://doi.org/10.1016/j.physletb.2014.06.077), arXiv:[1405.3455](https://arxiv.org/abs/1405.3455).
- [623] [17] CMS Collaboration, “Limits on the Higgs boson lifetime and width from its decay to four
624 charged leptons”, *Phys. Rev. D* **92** (2015) 072010,
625 doi:[10.1103/PhysRevD.92.072010](https://doi.org/10.1103/PhysRevD.92.072010), arXiv:[1507.06656](https://arxiv.org/abs/1507.06656).
- [626] [18] CMS Collaboration, “Measurement of differential and integrated fiducial cross sections
627 for higgs boson production in the four-lepton decay channel in pp collisions at $\sqrt{s} = 7$
628 and 8 tev”, arXiv:[1512.08377](https://arxiv.org/abs/1512.08377).
- [629] [19] CMS Collaboration Collaboration, “Measurements of properties of the Higgs boson in
630 the four-lepton final state in proton-proton collisions at $\sqrt{s} = 13$ TeV”, Technical Report
631 CMS-PAS-HIG-19-001, CERN, Geneva, 2019.
- [632] [20] I. Brivio, Y. Jiang, and M. Trott, “The SMEFTsim package, theory and tools”, *JHEP* **12**
633 (2017) 070, doi:[10.1007/JHEP12\(2017\)070](https://doi.org/10.1007/JHEP12(2017)070), arXiv:[1709.06492](https://arxiv.org/abs/1709.06492).
- [634] [21] J. Aebischer et al., “WCxf: an exchange format for Wilson coefficients beyond the
635 Standard Model”, *Comput. Phys. Commun.* **232** (2018) 71–83,
636 doi:[10.1016/j.cpc.2018.05.022](https://doi.org/10.1016/j.cpc.2018.05.022), arXiv:[1712.05298](https://arxiv.org/abs/1712.05298).
- [637] [22] S. Alioli, P. Nason, C. Oleari, and E. Re, “NLO vector-boson production matched with
638 shower in POWHEG”, *JHEP* **07** (2008) 060,
639 doi:[10.1088/1126-6708/2008/07/060](https://doi.org/10.1088/1126-6708/2008/07/060), arXiv:[0805.4802](https://arxiv.org/abs/0805.4802).
- [640] [23] P. Nason, “A new method for combining NLO QCD with shower Monte Carlo
641 algorithms”, *JHEP* **11** (2004) 040, doi:[10.1088/1126-6708/2004/11/040](https://doi.org/10.1088/1126-6708/2004/11/040),
642 arXiv:[hep-ph/0409146](https://arxiv.org/abs/hep-ph/0409146).
- [643] [24] S. Frixione, P. Nason, and C. Oleari, “Matching NLO QCD computations with parton
644 shower simulations: the POWHEG method”, *JHEP* **11** (2007) 070,
645 doi:[10.1088/1126-6708/2007/11/070](https://doi.org/10.1088/1126-6708/2007/11/070), arXiv:[0709.2092](https://arxiv.org/abs/0709.2092).
- [646] [25] E. Bagnaschi, G. Degrassi, P. Slavich, and A. Vicini, “Higgs production via gluon fusion
647 in the POWHEG approach in the SM and in the MSSM”, *JHEP* **02** (2012) 088,
648 doi:[10.1007/JHEP02\(2012\)088](https://doi.org/10.1007/JHEP02(2012)088), arXiv:[1111.2854](https://arxiv.org/abs/1111.2854).
- [649] [26] P. Nason and C. Oleari, “NLO Higgs boson production via vector-boson fusion matched
650 with shower in POWHEG”, *JHEP* **02** (2010) 037, doi:[10.1007/JHEP02\(2010\)037](https://doi.org/10.1007/JHEP02(2010)037),
651 arXiv:[0911.5299](https://arxiv.org/abs/0911.5299).
- [652] [27] H. B. Hartanto, B. Jager, L. Reina, and D. Wackerlo, “Higgs boson production in
653 association with top quarks in the POWHEG BOX”, *Phys. Rev. D* **91** (2015), no. 9, 094003,
654 doi:[10.1103/PhysRevD.91.094003](https://doi.org/10.1103/PhysRevD.91.094003), arXiv:[1501.04498](https://arxiv.org/abs/1501.04498).
- [655] [28] K. Hamilton, P. Nason, E. Re, and G. Zanderighi, “NNLOPS simulation of Higgs boson
656 production”, *JHEP* **10** (2013) 222, doi:[10.1007/JHEP10\(2013\)222](https://doi.org/10.1007/JHEP10(2013)222),
657 arXiv:[1309.0017](https://arxiv.org/abs/1309.0017).

- 658 [29] G. Luisoni, P. Nason, C. Oleari, and F. Tramontano, “ $HW^\pm/\text{HZ} + 0$ and 1 jet at NLO with
659 the POWHEG BOX interfaced to GoSam and their merging within MiNLO”, *JHEP* **10**
660 (2013) 083, doi:10.1007/JHEP10(2013)083, arXiv:1306.2542.
- 661 [30] Y. Gao et al., “Spin determination of single-produced resonances at hadron colliders”,
662 *Phys. Rev. D* **81** (2010) 075022, doi:10.1103/PhysRevD.81.075022,
663 arXiv:1001.3396. [Erratum: doi:10.1103/PhysRevD.81.079905].
- 664 [31] NNPDF Collaboration, “Parton distributions for the LHC Run II”, *JHEP* **04** (2015) 040,
665 doi:10.1007/JHEP04(2015)040, arXiv:1410.8849.
- 666 [32] P. Nason and G. Zanderighi, “ W^+W^- , WZ and ZZ production in the
667 POWHEG-BOX-V2”, *Eur. Phys. J.* **C74** (2014), no. 1, 2702,
668 doi:10.1140/epjc/s10052-013-2702-5, arXiv:1311.1365.
- 669 [33] J. M. Campbell and R. K. Ellis, “MCFM for the Tevatron and the LHC”, *Nucl. Phys. Proc.
670 Suppl.* **205** (2010) 10, doi:10.1016/j.nuclphysbps.2010.08.011,
671 arXiv:1007.3492.
- 672 [34] J. M. Campbell, R. K. Ellis, and C. Williams, “Bounding the Higgs width at the LHC
673 using full analytic results for $gg \rightarrow e^-e^+\mu^-\mu^+$ ”, *JHEP* **04** (2014) 060,
674 doi:10.1007/JHEP04(2014)060, arXiv:1311.3589.
- 675 [35] J. Alwall et al., “The automated computation of tree-level and next-to-leading order
676 differential cross sections, and their matching to parton shower simulations”, *JHEP* **07**
677 (2014) 079, doi:10.1007/JHEP07(2014)079, arXiv:1405.0301.
- 678 [36] CMS Collaboration, “Measurements of properties of the higgs boson in the four-lepton final
679 state in proton-proton collisions at $\sqrt{s} = 13$ TeV”, CMS-PAS-HIG-19-001 (2019).
- 680 [37] CMS Collaboration, “Measurement of the properties of the higgs boson in the four-lepton
681 final state at $\sqrt{s} = 13$ tev”, CMS Physics Analysis Note CMS-AN-15-277, CERN, 2016.
- 682 [38] CMS Collaboration, “Measurement of differential cross sections for Higgs boson
683 production in the diphoton decay channel in pp collisions at $\sqrt{s}=8$ TeV”, *Eur. Phys. J. C*
684 **76** (2015) 13, doi:10.1140/epjc/s10052-015-3853-3, arXiv:1508.07819.
- 685 [39] ATLAS and CMS Collaborations, LHC Higgs Combination Group, “Procedure for the lhc
686 higgs boson search combination in summer 2011”, ATL-PHYS-PUB/CMS NOTE 2011-11,
687 2011/005, CERN, 2011.
- 688 [40] G. Cowan, K. Cranmer, E. Gross, and O. Vitells, “Asymptotic formulae for
689 likelihood-based tests of new physics”, *Eur. Phys. J. C* **71** (2011) 1554, doi:10.1140/
690 epjc/s10052-011-1554-0, 10.1140/epjc/s10052-013-2501-z,
691 arXiv:1007.1727.